Simulation of Titanium and Titanium Alloy Powder Compact Forging

THE UNIVERSITY OF
WAIKATO
Te Whare Wānanga o Waikato

A report submitted in partial fulfilment of the requirements of a degree in

Master of Engineering

in Materials and Process Engineering

at

the University of Waikato

by :

Zhibo Zhang

The University of Waikato

Hamilton, New Zealand

Mar. 2011

Abstract

Simulation can be divided into two types: physical simulation and interactive numerical simulation. Physical simulation depends on testing smaller or cheaper samples rather than real objects to simplify models; Interactive simulation, which is also been called numerical simulation is depending on mathematical models and computer program to get the detailed results of the model. In this thesis, 48 compression test samples of sintered powder compacts of pure titanium (HDH) and Ti-6Al-4V were tested by using Gleeble 1500 thermal simulation testing machine. The height reduction of all samples was set as 70% and the other experiment conditions were set as three different temperatures and two strain rates. The stress-strain curves of all samples have been collected in the computer which could be considered as basic for the 3D-FEM simulation. Metal plastic forming is a coupled thermo-stress process in which the workpiece is loaded and restricted in some boundary conditions which include force, temperature, velocity, geometry, friction and so on. Thus, the scientific objective of plastic forming simulation is to be able to predict and control these phenomenon and transformation.The upsetting of powder compacts of pure titanium (HDH) and Ti-6Al-4V (GA) was studied in this thesis based on theoretical and physical models and numerical simulation. Based on the constituent model in ABAQUS and the results of thermo-simulation, the upsetting of 3D-FEM model was built which involved heat transfer, deformation and densification. The temperature field, Mises stress field, strain rate field, strain field and relative density field of pure titanium (HDH) and Ti-6Al-4V (GA) powder compacts were attained. Comparing the density distribution of the metallographic phases in optical microscope with the results of simulation, basically, the experimental results are in general agreement with the results of simulation.

Acknowledgements

I would like to thank to my chief supervisor, Professor Deliang Zhang for his significant advice, guidance and encouragement throughout this study. He helped me overcome hurdles that came along the way. Without his radiant efforts and great help, I could not complete my Master's study successfully. It is an honour for me to be able to work with him and I am looking forward for further research works under his brilliant supervision.

I sincerely appreciate all the help my colleagues at the Large Scale Lab have given me throughout my research which including many serious discussions. They are Stella Raynova, Fantao Kong, Mingtu Jia, Yongjun Su, Jia Lou, Dengshan Zhou, Hong Zhou, Huiyang Lu. I would like also appreciate to the technical staff Yuanji Zhang for helping me out with the instruments problems at the laboratory.

My deepest appreciation goes to my family. My parents and parents-in-law have shown their regardless love, encouragement and support throughout my studies. They have supported and accepted well the fact of being far away from them during this study of seeking further knowledge. My wife, Lynn He, had continuously motivated and encouraged me during my studies by giving me academic and emotional support. Last but not least, my son, Jiahao Zhang who is my strong emotional support as well. This Master's study has taught me a lot that they are more important to me in life than anything else in the world.

Contents

List of Figures

List of Tables

Chapter 1: Introduction

As a result of high strength, high toughness, good resistance to corrosion and good formability, titanium and titanium alloys have been widely used in aerospace, automobile, medical and sports industries[1]. Titanium alloys have been used commonly in aerospace to make many parts which include airplane structural parts, fire walls, landing gears, exhaust ducts, and hydraulic systems. To reduce vehicle weight and exhaust emission and increase vehicle life, automotive manufacturers have started to pay close attention to use titanium alloys to make automotive parts. The advantages of automotive parts made of titanium alloys are light weight, long life span, corrosion resistant and endurable at high temperatures. Titanium and titanium alloys have been used in making some medical parts as well. Due to light weight, high strength and biologically compatibility, they are considered as ideal medical materials for manufacturing joint prosthesis[2], artificial teeth[3] and so on. Titanium and titanium alloys are very popular in producing sports gears. Because they have so many advantages as mentioned above, they start to appear in our daily life. The typical daily titanium alloy products included watches, golf clubs, bicycles, spectacle frames, fishing rods, toys and etc.

In order to get the low cost method, titanium and its alloy powder metallurgy (PM) was developed rapidly into manufacture net or near-net shape products, which were used in the fields of automobile, medical, aerospace and sports. However, conventional PM techniques used in industry, which include powder compaction and sintering, are not satisfactory to produce high quality titanium and titanium products, due to lots of porosity, which is not eliminated during sintering process. There are several different ways to consolidate the powder compact, such as powder forging, powder extrusion, powder rolling. Among these methods, high temperature is needed to consolidate the powder compact, considering the deformation and diffusion process, so the deformation behavior of powder compact at high temperature became an emphasis of consolidation.

The hot forming for titanium and titanium alloy powder material is a very complicated elastic and plastic deformation process. This process does not only involve nonlinear behavior of the material, but also involve geometrical nonlinear relationships and nonlinear boundary conditions. Based on all these factors, its deformation mechanism is complicated and it is very hard to be described by using mathematical formula. Finite element method (FEM) simulation is used as an effective calculation method in metal hot forming. By using the least material or not doing any physical experiment to obtain distribution of stress, strain rate, temperature and relative density in metal plastic deformation process, and then to understand quantitatively the hot forming of titanium and titanium alloy powder material and predict formation of deformation defects and the changes of micromechanism.

The objectives of this thesis are as follows:

(1) Determine the high temperature deformation behavior of sintered powder compacts of pure titanium and Ti-6Al-4V (wt%) alloy.
(2) Set up the simulation models of powder compacts of pure titanium and Ti-6Al-4V alloy to be run using a finite element modeling (FEM) software package ABAQUS.
(3) Through FEM simulation using ABAQUS, attain the temperature field, Mises stress field, strain rate field and relative density field of the powder compacts during deformation.
(4) Compare the density distribution of experimental samples with that determined by simulation to determine the reliability and accuracy of the FEM simulation.

Chapter 2: Literature Review

2.1 Titanium and titanium alloys

Titanium is a very active element and can react with many elements in the periodic table of elements. Especially, it is easy to react with oxygen [4].There is hardly any possibility to find any pure titanium metal in nature. The surface of titanium is very similar to that steel which has silvery white metallic luster. It has a high melting point at 1670°C, and a fairly low density at 4.5g/cm^3[5].Titanium alloys are the alloys between titanium element and some other elements such as aluminum and vanadium. Titanium and titanium alloys have high specific strength which is the ratio of strength to density, compared with that of steel and aluminum alloys. They can be used at a large range of temperatures(250°C-600°C) with good mechanical properties [1, 5]. Titanium and titanium alloys have high corrosion resistance in many media and they have good compatibility with biological tissues, such as artificial apparatus as well.

Titanium normally has a closed packed hexagonal structure which called alpha – α titanium, but when it is been heated higher than 882°C, a body centered cubic is formed which called beta – β titanium. Alloying elements can change phase transition temperature between α-titanium and β-titanium and therefore, at room temperature, there are three kinds of titanium alloys; α titanium alloys, α/β titanium alloys and β titanium alloys[6].Thanks to the high strength, toughness, good corrosion resistance and formability, titanium and titanium alloys have been widely used in aerospace, automobile, medical and sports equipment industries[1].

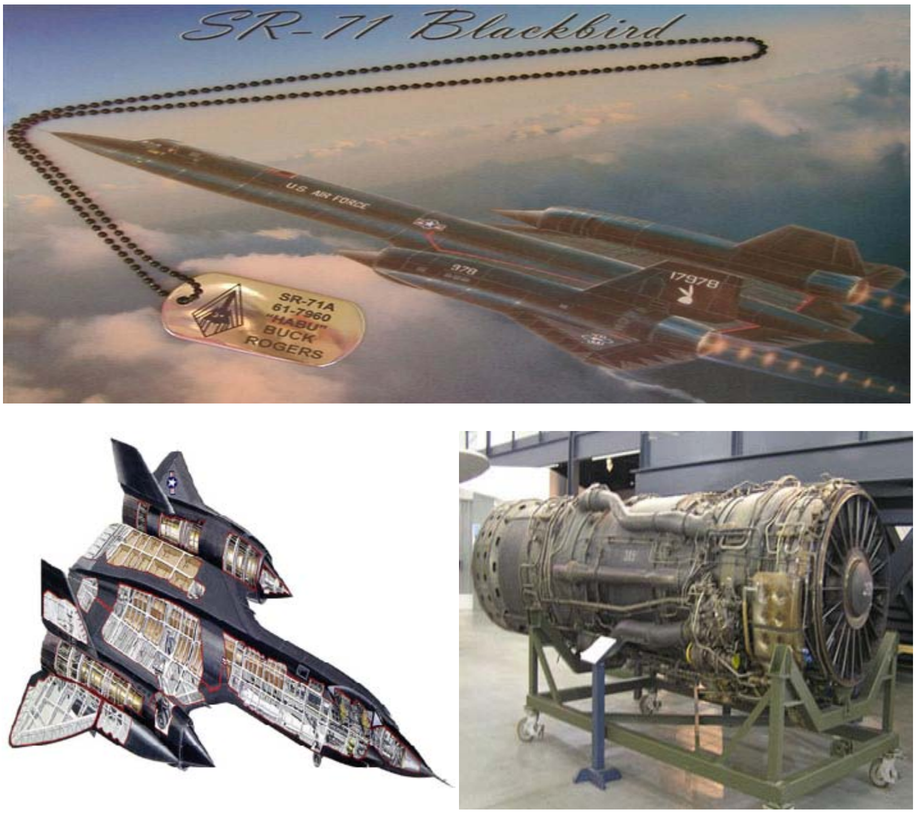

Figure 2.1: SR-71"Blackbird"[7, 8]

Titanium alloys have been commonly used in aerospace industry to make many parts which include airplane structural parts, fire walls, landing gears, exhaust ducts. The very first aircraft that has been made using a large amount titanium alloys in its structural parts is SR-71”Blackbird” as shown in Figure 2.1 which shown that titanium can be widely used in modern military and commercial applications. According to aircrafts research, 59 metric tons (130,000 pounds) of titanium alloys are used in Boeing 777 aircraft; 45 metric tons of titanium alloys are used in Boeing 747 aircraft; 18 metric tons of titanium alloys are used in producing a Boeing 737 aircraft, 32 metric tons of titanium alloys are used in producing an Airbus A340 aircraft, 18 metric tons of titanium alloys are used in producing an Airbus A330 aircraft, and 12 metric tons of titanium alloys are used in producing an Airbus A320. For aerospace engines, titanium alloy has been used to produce compressor blades, hydraulic system components, and nacelles. As in the aircraft applications, almost over 50% titanium alloys that have been used are Ti-6Al-4V alloys[9, 10].

Figure 2.2: Two pictures of titanium alloy automobile parts [11, 12]

Titanium and titanium alloys have been widely used in automobile industry. To reduce weight and exhaust emission and increase life of vehicles, the automobile manufacturers pay close attention to use more titanium alloys. The advantages of automobile parts made using titanium alloys are light weight, long life, corrosion resistant and durable at high temperatures. Due to all these features, titanium and titanium alloys have been used making automobiles parts industry [9], connecting rods [13], pistons[12], suspension springs and valve springs[14] as shown in Figure 2.2. With developing the technology for producing low cost titanium alloy parts, the application of titanium alloys in automobile field would be expended continually.

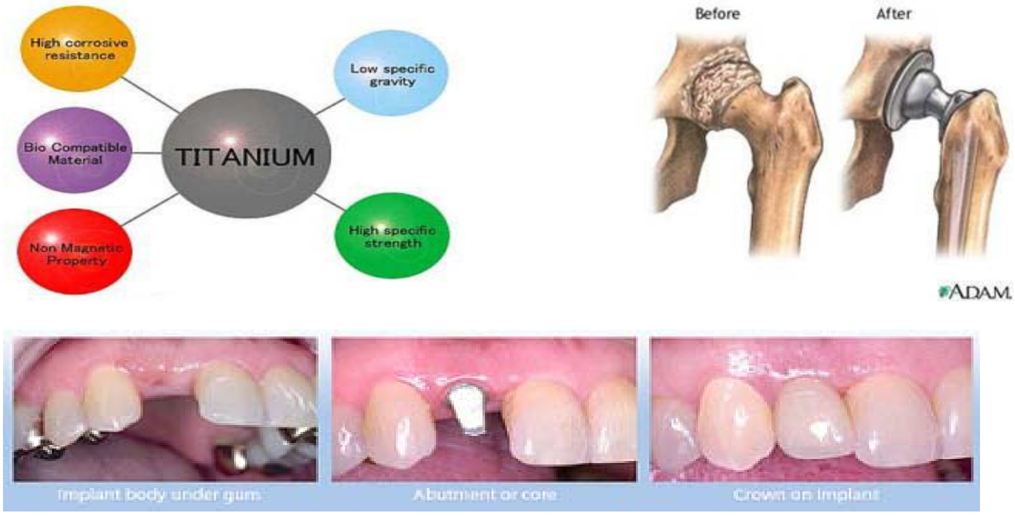

Figure 2.3: Some pictures of titanium and titanium alloy product of medical facilities[15]

Titanium and titanium alloys have been used in medical field as well. Since titanium and titanium alloys are light weight and corrosion resistant, have high strength and are biologically compatible, they are considered as the ideal medical materials for producing joint prosthesis[2], artificial teeth[3]and so on as shown in Figure 2.3.

Figure 2.4: Some pictures of titanium and titanium alloy products of sports and daily life[16-20]

Finally, titanium and titanium alloys are very popular in producing leisure and sports gears. Because they have so many advantages that mentioned above, they start to appear in our daily life as shown in Figure 2.4. The typical daily titanium alloy products included watches, golf clubs, bicycles, spectacle frames, fishing rods, toys and etc. The most representative products are golf club and bicycle. Golf clubs made from titanium alloys have the advantages of light weight, easy to control, and high accuracy; and bicycles made by titanium alloys are light weight, high strength, fatigue resistant, and have good shock-resistance by comparing with the ones that made by traditional steels. Many racing bicycles are made of titanium alloys.

2.2 Powder Metallurgy

Nowadays, powder metallurgy (P/M) technique has been well developed and widely used in commercial production because of its net or near-net shape capability[21]. By using powder metallurgy technique, processed products can get fine and uniform microstructure. In addition, powders of different metal elements can be mixed together and processed to produce final products with unique properties[22]. Powder metallurgy products have been used in a broad range of industrial fields, ranging from automotive and aerospace applications to power tools and household appliances. Powder metallurgy technique has been developed very fast nowadays. The traditional powder metallurgy process is commonly used in manufacturing an extended range of metallic net shape parts[23].

The general procedure of traditional powder metallurgy is blending → compacting → sintering → shaping →post processing as show in Figure 2.5.

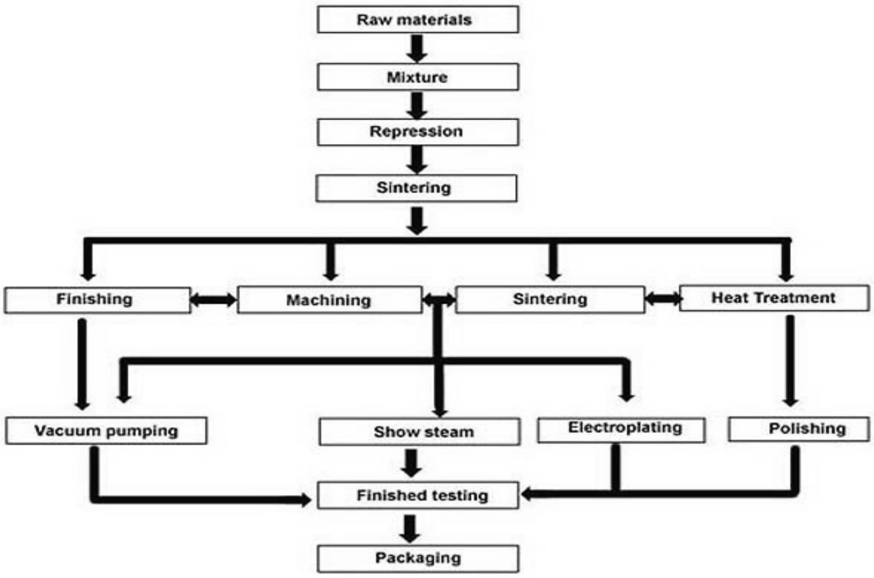

Figure 2.5: General procedures of powder metallurgy [24]

There are several advantages of traditional powder metallurgy[25]

- Net or near-net shape capability, with no or very small amount of cutting and machining;
- High utilization rate of materials, over 95%;
- Small grain sizes and consistent and stable microstructure;

- High strength and hardness;
- Ability to produce complex or abnormal structural parts by mold forming which is difficult to be produced by other methods; and
- High energy efficiency and environment friendly.

However, there are several disadvantages of traditional powder metallurgy, and they are:

- Parts have low ductility;
- Parts have low density;
- Impurity elements are easy to be mixed in the products; and
- High raw powder costs.

By comparing with traditional powder metallurgy technique, the recently developed powder metallurgy techniques have a huge improvement. They not only retain the advantages of the traditional powder metallurgy but also overcome some of their disadvantages. These recently developed techniques include powder forging, powder extrusion, hot isotactic pressing and powder injection moulding.

2.3 Titanium based powder metallurgy

Titanium based powder metallurgy overcome the disadvantages of machining and casting, and at the same time, it keeps their advantages such as net or near-net shape capabilities. Basically, it can save the cost to produce titanium products. The titanium based powder metallurgy products have the potential to be used in domains of automobile, medical, aerospace and sports.

There are four methods for producing titanium and titanium alloy powders:

Reduction method; It involves reduction of TiO_2 or $TiCl_4$ using Ca, Na, Mg at elevated temperatures to get Ti powder [26]. The Ti sponge produced by reduction of $TiCl_4$ by Na can be used to produce Ti powder which has low cost. However, such powder contains NaCl which can cause corrosion of sintering equipment and deterioration of material property. The reaction of $TiCl_4$ and Mg is called Kroll method which is another way of producing sponge Ti at low cost with irregular particles. [27, 28] After sponge Ti is ball-milled, the Ti powder can be gained. Due to the sponge Ti powder has lower toughness, high impurity, high particle porosity and it can be used at low temperature, it cannot be used in high demand field such as aerospace and medicine, which is a limitation.

Electrolytic deposition method; Ti powder gained by electrolytic deposition had higher purity than that by reduction method.

Hydride de-hydride (HDH) method; this method turns sponge Ti into Ti powder. It is difficult to crush sponge Ti to powder at room temperature and ambient atmosphere, but hydride of Ti is much easier to be crushed to powder. Therefore, by increasing the ability of Ti in absorbing hydrogen through increasing temperature, sponge Ti can react with hydrogen to form TiH_2 which is more brittle. TiH_2 sponge can be crushed into TiH_2 powder. The hydrogen in TiH_2 powder can be removed by heat treating it under vacuum, and this produces Ti powder. The Ti powder producing using the HDH method has the advantages of low cost and irregular particle shapes and low O content[29], but it has high Cl content which can cause problems.

Gas atomisation method; Gas atomisation is very widely used to produce titanium powder. In a general way, molten titanium stream is impinged by stream of high pressure inert gas which then solidifies into solid particles in flying. Some molten titanium stream can also be broken into droplets by other force like centrifugal force. Ti powder which is produced by gas atomisation method generally has spherical particles. The process has the features of high production, favorable microstructure of the powder particles, fine grain size, low level of solute segregation, small size of secondary phase particles and easy to be used as pre-alloyed powders[29]. There are several different powder consolidation techniques that are commonly been used. First of all, the technique is loose powder sintering.

Using this method of titanium powder can be turned into porous titanium with a relative density of 25%-70%. The second compact technique is pressing and sintering. The density of titanium powder compact can reach up to 92%-95% by using this method. Thirdly, hot isostatic pressing (HIP) is used as another technique for titanium powder consolidation. Being used as a manufacturing process, it can cut down the porosity of powder compacts. HIP enhances the mechanical properties and workability of materials[30]. The relative density of titanium powder compact can reach up to approximately theoretical density after HIP. It is potentially the most cost-effective and efficient process for the manufacture of high quality metal components from powders[31]. It is used to produce some complex parts such as diffusers, turbines and impellers for aircraft and helicopter engines. The next technique is powder compact forging, powder compact extrusion or powder compact rolling. The density of titanium powder compact can also reach up to approximately theoretical density as well. This method is widely used to produce parts with special shapes and high performance materials. Powder forging is a kind of method that combines conventional traditional powder metallurgy and conventional forging. Powder extrusion is the process which is used to produce structural members of fixed cross-sectional profile. The billet is pushed through a die of the desired cross-section. This method has become one of the most popular methods to produce cemented carbide, alloy tube, alloy rod, alloy bar and alloy other member with shapes. The next technique is powder injection moulding (PIM) which is used in titanium powder consolidation. This technique is capable of producing mass intricately shaped components. In recent years, this technology has been adopted in electronic, computer, chemical and medical industries. [32] PIM is used to produce small complex parts such as watch frames or branches for spectacles[23]. The final technique to be mentioned is selective laser sintering (SLS) which is used to produce and repair metal parts directly from CAD data. Not only is SLS a effective high-speed forming tool, but also a highly active instrument to produce intricacy parts[33].

2.4 Powder Forging and Powder Extrusion

2.4.1 Powder Forging

Powder forging combines traditional powder metallurgy and forging. Powder forging, as a mature manufacturing process, has already been used in industrial scale production. Hays, which is a company in the United States, has built a hot powder forging production line for manufacturing automobile parts with a volume of 680 kg/h[34]. Nowadays, the heaviest part that is produced by powder forging technique has reached up to 22.6 kg[35], and there are more than ten automobile parts being produced by using powder forging in automobile industry. Some examples are shown in Figure 2.6.

Figure 2.6: Some pictures of some automobile powder forged parts[36]

The purpose of powder forging (PF) is that powder compacts can be forged to get high density parts with very low porosity level. There are commonly four processes which include cold forging, forged sintering, sintered forging, powder forging, as shown in Figure 2.7.

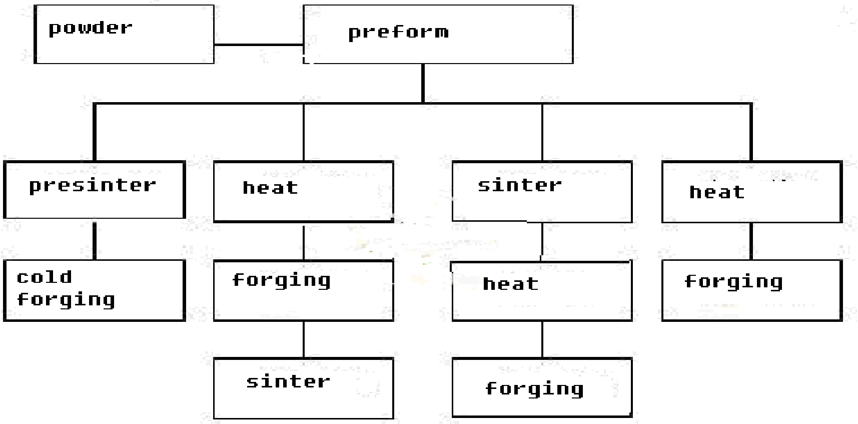

Figure 2.7: A sketch map of powder forging [37]

Preforms for forging are prepared in several steps that mainly include compaction, and sintering[38]. The process of compaction creates the powder compacts that are shaped into three-dimensional bodies which are similar to those traditional P/M parts. However, there are some differences between compaction of P/M parts and PF preforms. Compaction of P/M parts should be controlled specially in order to get the uniform density of the compacts. While the PF powder preform should be controlled in order to create a shape that can be forged to get full density and avoid the formation of cracks, wrinkles and laps. [39] There are two compaction techniques for creating powder compacts, and they are die compaction and cold isostatic pressing (CIP). Die compaction utilizes rigid tooling and uniaxial pressing equipment is widely used because of its high production rate. On the other hand, cold isostatic pressing uses hydrostatic press which densifies powder compacts by using a flexible mold at room temperature [39].

Powder compacts need to be sintered because of its low strength. The purpose of sintering is that powder compacts achieve solid bonds among powder particles and it can help to reduce the size and number of pores. Sintering must be performed at specific temperatures and under controlled atmosphere [39]. Powder forging is a process in which powder are forged to achieve full density and specific shapes of the products. As shown in Figure 2.8, a powder compact preform is put in a die having a cylindrical hollow cavity. An upper punch is used to apply load, and a bottom punch is used to push the part out.

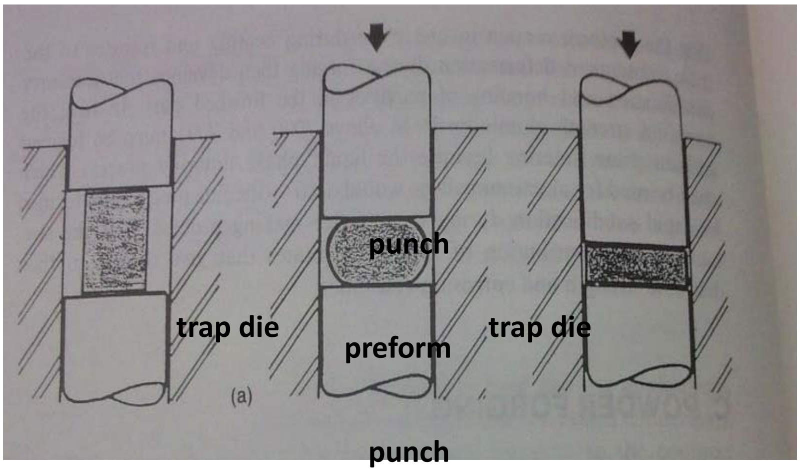

Figure 2.8: The illustration of three kinds of powder forging[39]

The density of the parts produced by powder forging is vital, and it can affect the strength, ductility and fatigue strength of powder forgings. The most dramatic weakness of conventional powder metallurgy is that there are too many pores in the parts. The mechanical properties of material decreases quickly as the porosity level increases, as shown in Figure 2.9.

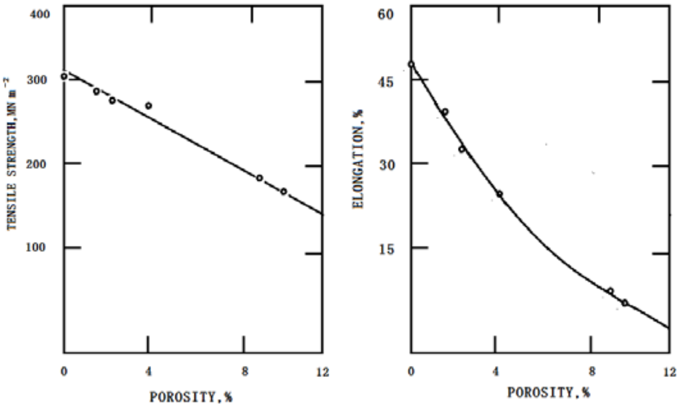

Figure 2.9: Effect of porosity level on strength and tensile ductility of billets produced by sintering from iron powder compact [40]

There are some factors that can affect the workability of powder forging. They include stress field、strain field and strain energy density formulation. Especially the fracture criteria in strain energy density formulation is considered as an important factor by many authors such as Freudenthal [41], Cockcroft and Latham

[42] and Norris et al[43]. Ductile fracture consumed a lot of energy ahead of the crack formed during fracturing, leading to enhanced formability. The bigger the plastic zone the greater the amount of energy absorbed by fracture [39]. However, pores in the material deformed and fractured can reduce the energy absorption during fracture; and thus the quantity of pores of sintered powder materials can reduce their ductility[39]. The upset tests have been used to evaluate the workability of materials [39]. During the upset test, the real stress and real strain of the billet can be determined by measuring the height and diameter of cylindrical billets.

2.4.2 Extrusion

Extrusion is a plastic forming process in which a billet is pushed through an opening in a die to obtain a slender member with specific cross-sectional shape or profile. There are many advantages of extrusion process. First of all, it has the ability to produce very complex cross-sections. Secondly, by using extrusion process, many materials, or even brittle materials can be extruded because the materials only encounter compressive and shear stresses rather than tensile stresses. Thirdly, the finished billet can have excellent surface. In addition, extrusion process has high material utilization rate, and it improves the mechanical properties of materials. It can be done by simple operation and has high productivity. Extrusion can be used to produce long poles and members with thin walls. [44].

Extrusion can be divided into two different types according to the processing temperatures: hot extrusion and cold extrusion. Hot extrusion works at a temperature higher than the recrystallization temperature of the billet in order to make it easier to push the billet through opening of the die. In most cases hot extrusion requires lubrication because of the high friction between the billet and the wall of extrusion chamber. Glass powder can be used as a lubricant and is very popular in hot powder extrusion. Cold extrusion, on the other hand, metal extrusion done at room temperature. In comparing with hot extrusion process, it can get higher material strength, better finished surface and closer dimention tolerances. Materials that normally processed by using cold extrusion process includes lead, tin, aluminum, copper, zirconium, titanium, beryllium, vanadium, niobium, and steel. Cold extrusion requires lubrication as well. Oil and graphite are widely used as lubrication in cold extrusion process[44].

Extrusion can be divided into two different types based on the equipments used: direct extrusion and indirect extrusion. Direct extrusion is commonly used. In the direct extrusion process the billet is placed in a container with thick wall and then pushed to pass through an opening in the extrusion die by a ram. Reusable dummy block is placed between the ram and the billet to prevent their contact. In this extrusion process, frictional forces arise because the billet need to travel the entire length of the container. Thus, direct extrusion needs more force than indirect extrusion. In indirect extrusion process, the extrusion die is pushed against the billet to force the billet material to pass through the opening in the extrusion die. In this process, the force needed can be reduced by 25 to 30%, due to the lack of friction between the billet and the container. Indirect extrusion can achieve large extrusion ratio with the same level of force. The extrusion ratio is defined as the starting cross-sectional area divided by the cross-sectional area of the extrudee. However, indirect extrusion is not as flexible as direct extrusion since the cross-sectional area of the extrudee is restricted by the smallest dimensions of the ram[44], the extrudee has to go through the ram to come out.

2.4.3 Powder Extrusion

Powder extrusion process is a new technology developed based on conventional extrusion. It is one of the most popular methods to produce tubs, rods, bars and members of other abnormal cross sectional shapes out of cemented carbides and alloy powders. The basic principle of powder extrusion process is similar to that of conventional extrusion process. The main difference of powder extrusion from conventional extrusion is that powder extrusion utilizes powder compacts rather billet as starting material. Both hot extrusion and cold extrusion can be used to extrude metal powders compacts, although hot extrusion is more widely used. In the same sense, both direct extrusion and indirect extrusion can be used in powder extrusion process which is according to the equipments that is being used in the process.

Hot extrusion of metal powder is an advanced technology being used to create fully dense. There are three basic methods of hot powder extrusion which as shown in Figure 2.10, and they are basic powder extrusion, powder compact extrusion and canned indirect powder compact extrusion.

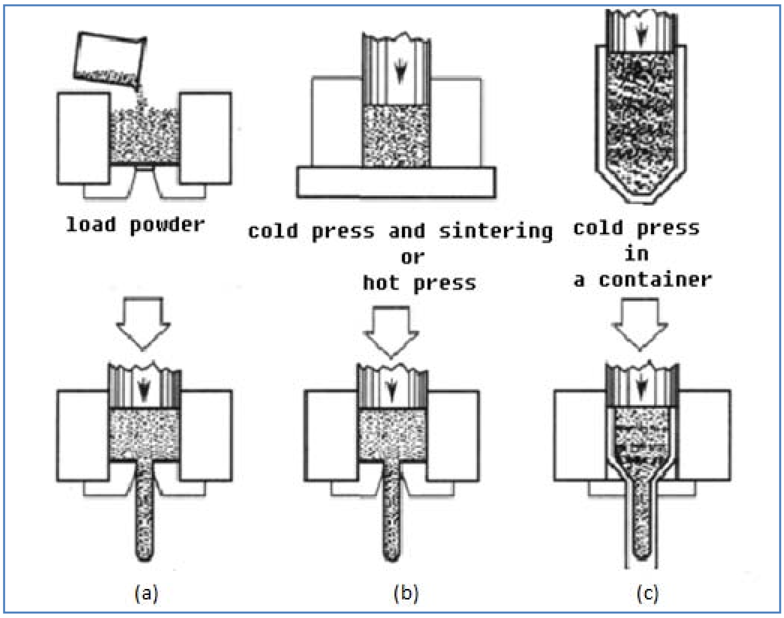

Figure 2.10: A schematic diagram of three basic methods of powder extrusion: (a) basic powder extrusion, (b) powder compact extrusion, (c) canned powder compact extrusion

In basic powder extrusion, metal powder is loaded into the extrusion chamber and then extruded directly through the extrusion die. This process has been used in consolidation of magnesium alloy powders. In the presence of protective atmosphere, the extrusion chamber loaded with powder is heated, and then metal powder is extruded after it is heated to a set temperature. In powder compact extrusion, the metal powder is first cold presses and sintered and then entrusted.

This method has been used to consolidate aluminum and molybdenum powders.

In canned powder extrusion, the metal powder is loaded into a heated container and then they are hot extruded together. The container can help to reduce friction.

Powder extrusion is widely used in several different applications which include producing metal pipe, rods, bars, tubes. Especially, powder extrusion of aluminium alloy, magnesium alloy and titanium alloy powders can be used to produce aircraft parts. In addition, alloy powders can be created advanced materials in the form of using powder extrusion and consolidated. There are some examples of products that have been produced by powder extrusion process from different metal powders as shown in Table 2.1

Table 2.1: Some common metal for powder extrusion, extrusion temperatures and examples of products[44]

Metal powders	Extrusion Temperature	Examples of Products
Aluminium alloy	300^{o}C -600^{o}C	aircraft parts, tubes frames
Copper alloy	600^{o}C -100^{o}C	pipe, wire, rods, bars, tubes
Lead alloy	300^{o}C	pipes, wire, tubes, and cable sheathing
Magnesium alloy	30^{o}C -600^{o}C	aircraft parts and nuclear industry parts
Zinc alloy	200^{o}C -350^{o}C	rods, bar, tubes, hardware components, fitting
Steel alloy	1000^{o}C -1300^{o}C	pipe, rods, bars, tubes
Titanium	600^{o}C -1000^{o}C	aircraft components
Tungsten		Filament

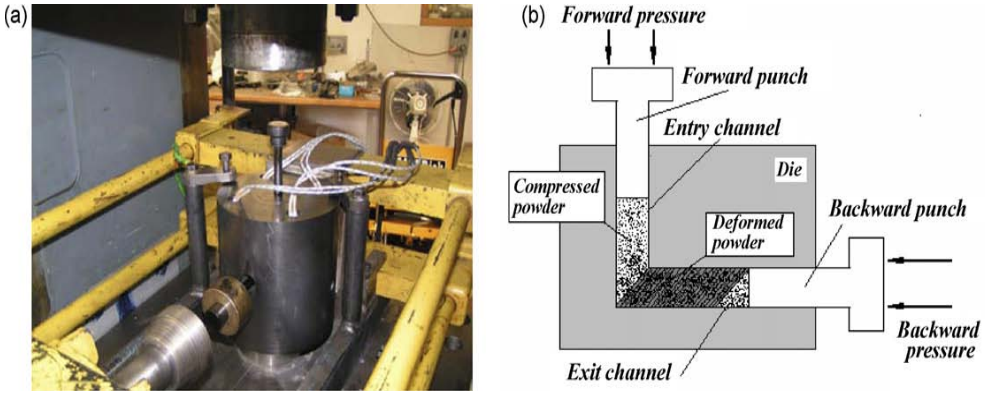

Figure 2.11: Equal channel angular extrusion of powder: (a) Unit for elevated-temperature ECAE with back pressure; (b) Schematic of the powder compaction process[45]

As a new powder consolidation method, Equal channel angular extrusion (ECAE) has been applied. [29]. Figure 2.11(a) shows the ECAE equipment which has a heated die which schematic allows heating of the powder from 20 to 450^{o}C. Figure 2.11(b) is a schematic diagram showing the powder compaction process. The back pressure generated by the backward punch from a horizontal hydraulic cylinder, is set at a level in the range of 20 and 500MPa. When the powder is loaded into the vertical channel of the die, the backward punch was at the innermost position so that all powder is held in the vertical channel. After this, the forward punch was applied above the powder. The die which has been loaded with powder is then heated up to the desired temperature in less than 10 minutes and then the extrusion of powder was done with a speed of 2 mm /s. As the downward load is gradually increased, an increased hydrostatic pressure is generated in the upright channel to pre-compact the powder. After the forward pressure is greater than the pre-set backward pressure, the powder compact starts to flow into the horizontal channel, causing shear deformation of the powder compact. As the shape of cross-section of the powder compact does not change in deformation, ECAE requires lower extrusion force[30]. In addition, during this process, the strength and hardness of the material increase. High density bars of Ti–6Al–4V alloy have been created by using ECAE process[45]. The bars achieved a relative density of 96% when the extrusion temperature was in the range 100◦C and the relative density increased to 98% when the temperature increased to 400◦C applied backward pressure 175MPa. The microstructure and mechanical properties of samples was by consolidation of pre-alloyed Ti-6Al-4V powder use the ECAE at temperatures of 500-800◦C was studied[21]. In this study, firstly, a Ti-6Al-4V cylindrical rod with a diameter of 10 mm was produced by cold isostatic pressing 380 MPa and vacuum sintering at 1230◦C for 4 hours. The rod was then hot isostatically pressed at 100 MPa and 900◦C for 2 hours followed by furnace cooling. After this process, a coarse colony lamella α microstructure with an average colony size of 70μm and lamellae α plate size of 17μm was created. Secondly, the cylindrical rod was then put into 25.4×25.4 mm rectangular stainless steel can and heated to temperatures between 550◦C and 800 ◦C for 1 hour. ECAE process was done with a 90° cross-section angle die preheated to 300◦C and an extrusion rate of 12.7 mm/s. In this study, it was found that shear deformation caused significant reduction of grain sizes which leads to a significant improvement in tensile and compressive strengths at room temperature.

2.5 Finite Element Method for Simulation of Metal Forming

Metal forming is a theromechanical process in which a billet is loaded and restricted with certain boundary conditions which include force, temperature, velocity, geometry, friction and so on. In this process, the material microstructure goes through a dramatic and complex transformation, including dislocation generation and movement, grain boundary movement, recrystallization, grain growth, second phase precipitation, texture formation and etc. These microstructural changes lead to changes of mechanical properties. Thus, the objectives of simulation are to predict and control of these changes.

There are two types of simulation: physical simulation and numerical simulation [46]. Physical simulation is based on testing smaller or cheaper samples rather than real objects as models. Numerical simulation is based on mathematical models and computer program to get the detailed results of the modelling.

Physical simulation and numerical simulation are interdependent. On one hand, the accuracy and universality of physical simulation is relied on the measuring method and the operability of hot metal hot forming. On the other hand, numerical simulation can supply full variable data. However, for some metal plastic forming process, there had not been fully functional mathematical models. Some parameters and relationships must be gained by physical simulation. Physical simulation can be considered as the foundation of numerical simulation and they must be used coherently in order to achieve more accurate results in accordance with the real process[47].

As the computer technology has been developed nowadays, numerical simulation has been realized as a very important method in powder forming. There are several methods that have been used to do numerical simulation of powder forming. They are upper bound method[48], boundary element method [49] and finite element method (FEM)[50].

FEM for simulation of powder forming is based on constant mass. There are several very unstable processes which include shape, boundary conditions, and materials property, which change constantly. FEM can be utilized to solve constitutive equations of metal forming to enable numerical simulation which in turn used to analyze the variation of stress, strain, density, strain rate and temperature as a function of time during hot powder forming. FEM can be considered as the most effective numerical method for analyzing the process of powder forming. By doing simulation using FEM, it is very convenient to see all the interactions between process parameters that are displayed in the computer [51].

For simulation of metal forming, FEM can be classified into four groups: elastic-plastic finite element method (EP-FEM); elastic-viscoplastic finite element method (EVP-FEM); rigid-plastic finite element method (RP-FEM); and rigid-viscoplastic finite element method (RVP-FEM)[52]. EP-FEM and EVP-FEM are mainly used of solid metal forming. By using these two methods, many nonlinear mathematical problems can be solved, such as those related to stress field and strain field. However, their disadvantages are that the increment is not big and a large amount of calculation need to be ran [53]. RP-FEM and RVP-FEM are normally used in flow simulation. By using these two methods, bigger increment can be used and the calculation in every increment is base on the last increment in which material is deformed [54]. For the simulation of powder forming process, RVP-FEM and EVP-FEM are considered as the two best methods. EVP-FEM is more widely been used than RVP-FEM in simulation of hot powder forming. EVP-FEM is used in simulation of hot powder forming processed in the present study.

2.5.1 FEM modeling

In hot metal powder forming, the material has strain rate sensitivity. Powder materials have viscosity like clay. Thus, EVP-FEM is the most suitable method to simulate powder forming. By using EVP-FEM, coupled thermal and stress analyses can be done to simulate powder forging, powder extrusion, powder drawing and powder rolling. There are some advantages of EVP-FEM simulation:
Firstly, most of complex structures, boundary conditions and material model can be operated by the EVP-FEM, while other methods can have some limitations. Secondly, some important information could be shown directly from EVP-FEM. For example, the stress field and strain field, velocity field, and temperature field. This helps mould design and optimization process. Thirdly, the computation precision of FEM depends on shape and size of elements. Hence, with the computer capability developing rapidly, the computation precision of FEM would be improved further. Finally, by using EVP-FEM program software, most complex problems can be solved with less number of parameters.

In order to optimize the powder forming process, it is essential to treat the process as a system, which should include some aspects as following:

A. Material and die properties. They include density, specific heat, conductivity, and yield stress of material. All those features should be used as functions of temperatures and strain rates, and all the functions should be obtained by experiments. For example, by using compression test, the relationships between temperature, stress, strain and strain rate at a given time can be found and used as the basis for simulation.

B. Friction conditions. Friction conditions relate to pressure and friction coefficient which can effect deformation and heat transfer of workpiece.

C. Deformation mechanism. Plastic flow of metal is affected by the shape and dimensions of the cavity in the die, friction action, properties of the material deformed, and heat transfer conditions. All of these are important factors affecting the deformation of metal.

D. Product properties. They include macroscopic properties and microscopic properties. Macroscopic properties are mainly related to geometry, shape and the dimension of material. Microcosmic properties are related to surface quality and microstructure of material. In addition, it is important to study the relationships between material properties and microstructure, and processing conditions such as strain, strain rate and temperature.

To sum up, the system can be described in a relation schema as shown in Figure 2.12.

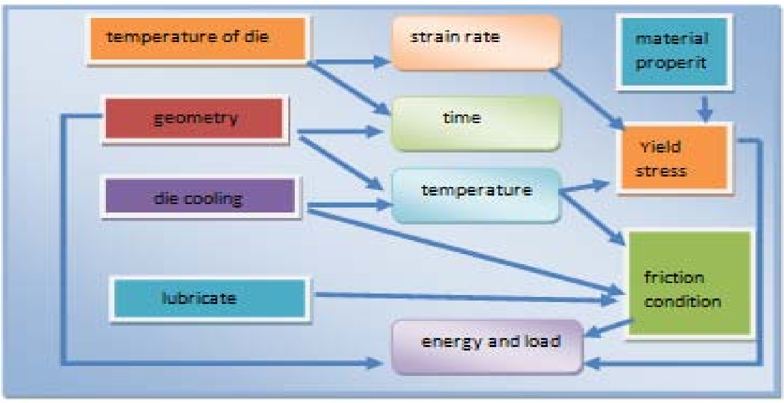

Figure 2.12: A relation schema of some parameters of metal plastic forming

FEM simulation of forming has two steps. Firstly, the model and values of essential input parameters of object used in FEM simulation should be put into the computer. They include geometry and dimension, material parameters, initial conditions and boundary conditions. Secondly, based on these inputs, a series of different equations are solved numerically by computer to determine the output parameters and then shown them in display.

The key factor affecting the computational accuracy is the difference between constitutive equations used in computer and mechanism of the process. In the process of hot metal forming, the mechanical and thermal properties of die and workpiece at different temperatures should be provided. If microstructure transformation change is simulated, the constitutive equation for microstructure changes such as phase transformation should be provided as well.

After the constitutive equations are established, the most important thing is to determine the values of the material parameters in constitutive equations. Generally, there were three methods to test the parameters tensile tests, compression tests and twisting tests. However, asymmetry was a problem that involved stress, strain and temperature. Due to asymmetry, the results of testing would have some systematic errors.

In FEM simulation, the object model is meshed. The quantity of meshes directly affected the computational accuracy. However, a too large number of meshes can reduce the calculation speed. Thus, it is reasonable to re-mesh the important regions of the workpiece. The method of tetrahedron element meshing is widely used in many FEM softwares, and it has advantages of easiness of re-mesh, and good coordination for complex shapes. However, its disadvantage is low computational accuracy. The method of hexahedron element meshing is considered as a better method to get higher computational accuracy. However, the method is sometime difficult to be used in simulation of part with a complex shape.

2.5.2 FEM Post-processing

FEM simulation can help to predict details of metal plastic forming and obtain all physical parameters about deformation of workpiece and die as a function of time and location. Usually, these physical parameters include: geometry, temperature, displacement, velocity, stress, strain, strain rate, load force of inside the workpiece and the die, respectively. In addition, density distribution can be gained for powder forming. Simulation could help of powder compact engineers to know if their designs of process, die and workpiece are reasonable without any experiment. If not reasonable, they can modify conditions continually by using computer until getting satisfied designs. By using FEM simulation, experiment time can be reduced, and the cost of producing new products can be cut.

From the output parameters from FEM simulation, it can be determined whether the workpiece would have some deformation defects. For instance, from geometry output, one can see if the fold back effect has occurred and if the die cavity is completely filled in impression die forging. From temperature distribution, one can see if certain regions of the workpiece are overheated. From fracture criterion, one can see if the fracture of the workpiece has occurred.

FEM simulation is based on ideal conditions. However, the real conditions are complex. The computer normally does not have enough memory and speed for simulating some complex processing. In addition, so far, accurate constitutive equations to simulate real process are not all available because of limited science development. Due to the complexity of the process and the limitation of experiment conditions, the values of material’s mechanical and thermal properties of different temperatures either have some errors or are not available. Despite of these limitations, in many circumstances, the FEM simulation results can be accepted and used to forecast trends of changes as function of input parameters.

Chapter 3: Experimental Procedure

3.1Powder Compacting

In order to prepare compression test samples, powder compacts need to be prepared. In this experiment, titanium powder produced using hydride dehydride (HDH) process and Ti-6Al-4V powder produced using gas atomization (GA) process were compacted into eight groups of powder compacts. The experimental procedure for powder compacting is as follows:

A. HDH titanium Powder compacts

   Firstly, 160grams of HDH titanium powder was put in a die which had Ø40mm diameter and then shake the die to jolt-pack the powder. Secondly, the die was heated to 250^{o}C in air. Thirdly, the powder in the die was pressed with a pressure of 630MPa and hold for 10 minutes to complete this process.

B. GA Ti-6Al-4V powder compacts

   Firstly, 160 grams of GA Ti-6Al-4V powder (GA) was put in a die which had Ø40mm diameter and then shake the die to jolt-pack powder. Secondly, the die was heated to 550^{o}C in argon. Finally, the powder in the die was pressed with a pressure of 780MPa and hold for 20mins to complete this process.

In this experiment, the powder compacts were made by using a 100 ton hydraulic press machine and a rigid die, as shown in Figure 3.1.

(a)

(b)

Figure 3.1: (a) 100 ton hydraulic press (b) The rigid die used for compacting powders

3.2 Induction Sintering

In order to strengthen and densitify powder compacts, all eight powder compacts were sintered by using induction heating under argon. Firstly, powder compacts were heated to 1200°C and 1300°C respectively, and then keep the powder compacts at that temperature for either 0 minute or 5minutes as shown in Table 3.1.

Table 3.1: The sintering plan

Temperature Holding Time	0	5mins
1200°C (Titanium)	Bulk A	Bulk C
1300°C (Titanium)	Bulk B	Bulk D
1200°C (Ti-6Al-4V)	Bulk E	Bulk G
1300°C (Ti-6Al-4V)	Bulk F	Bulk H

Secondly, different marks were written on the sintered powder compacts by sign pen to distinguish the samples made using different sintering conditions. Before starting to heat the powder compacts, the oxygen content of the argon atmosphere in the glove box was controlled to be under 200ppm. The heating rate was maintained at 300ºC/min until the temperature reacted either 1200°C or 1300°C.

3.3 Cutting and Polishing

The dimensions of the compression test samples should be Ø8mm×12mm. However, in order to have allowance for polishing, each induction sintered bulk sample was cut into eight small samples with dimensions of Ø8.2mm×12.8mm by using an electric discharge machining wire cutting machine .The cutting procedure is as follows:

- The computer program with 3D format was setup. The program includes a cutting route of circle with a diameter of 8.2mm.
- The positioning of the molybdenum wire in the plane view of powder compact was checked by visual testing and then the powder compact was fixed onto the fixture using clamps.
- The wire cutting machine and the programs with the circle of 3D program were run so that every bulk sample was cut into 4-12 cylinders with

dimensions of approximately Ø8.2mm × 30 mm.

- The cylinders were bound with a rubber band on a thin steel plate with 8mm × 50mm, and the cutting program was run again to cut into two groups of cylindrical samples with dimensions approximately Ø8.2mm × 12.8mm.
- Finally, the two end surfaces of each cylindrical samples were polished by using a rotary grinding and polishing machine with SiC papers of 600 and 1000 grits, and the side faces of all cylindrical samples were polished by hands with SiC papers of 600 and 1000 grits.

3.4 High Temperature Compression Testing

This high temperature compression testing was done at Harbin Institute of Technology in China. All compression test samples were tested by using Gleeble 1500 thermomechanical simulation testing machine. The height reduction of a sample was set at 70% and the other experiment conditions are shown in Table 3.2. There were three different temperatures and two strain rates.

Table 3.1: Compression testing plan

Temperature\strain rate	0.01/s	1/s
1000°C(Ti)	#Ti-1001A,#Ti-1001B #Ti-1001C,#Ti-1001D	#Ti-1010A,#Ti-1010B #Ti-1010C,#Ti-1010D
1100°C(Ti)	#Ti-1101A,#Ti-1101B #Ti-1101C,#Ti-1101D	#Ti-1110A,#Ti-1110B #Ti-1110C,#Ti-1110D
1200°C(Ti)	#Ti-1201A,#Ti-1201B #Ti-1201C,#Ti-1201D	#Ti-1210A,#Ti-1210B #Ti-1210C, #Ti-1210D
1000°C (Ti64)	#64-1001E,#64-1001F #64-1001G,#64-1001H	#64-1010E,#64-1010F #64-1010G,#64-1010H
1100°C (Ti64)	#64-1101E,#64-1101F #64-1101G,#64-1101H	#64-1110E,#64-1110F #64-1110G,#64-1110H
1200°C (Ti64)	#64-1201E,#64-1201F #64-1201G,#64-1201H	#64-1210E,#64-1210F #64-1210G,#64-1210H

- The experimental details are as follows:
  - Graphite was painted on the two end faces of each sample in order to reduce the friction force between the sample and the working surfaces of the anvil.

- Electric heating was used to heat the sample to the preset temperature (1000°C -1200°C) at a heating rate of 10°C/s and then kept the temperature for one minute.
- The samples were compressed at the velocity which was calculated based on the preset strain rate and sample height.
- The stress-strain curves of all samples were collected in the computer connected to the machine

The high temperature compression experiment set up is shown schematically in Figure 3.2. The temperature of the sample tested was measured using a NiCr-NiAl thermocouple which was welded on the side surface at the middle height of the sample.

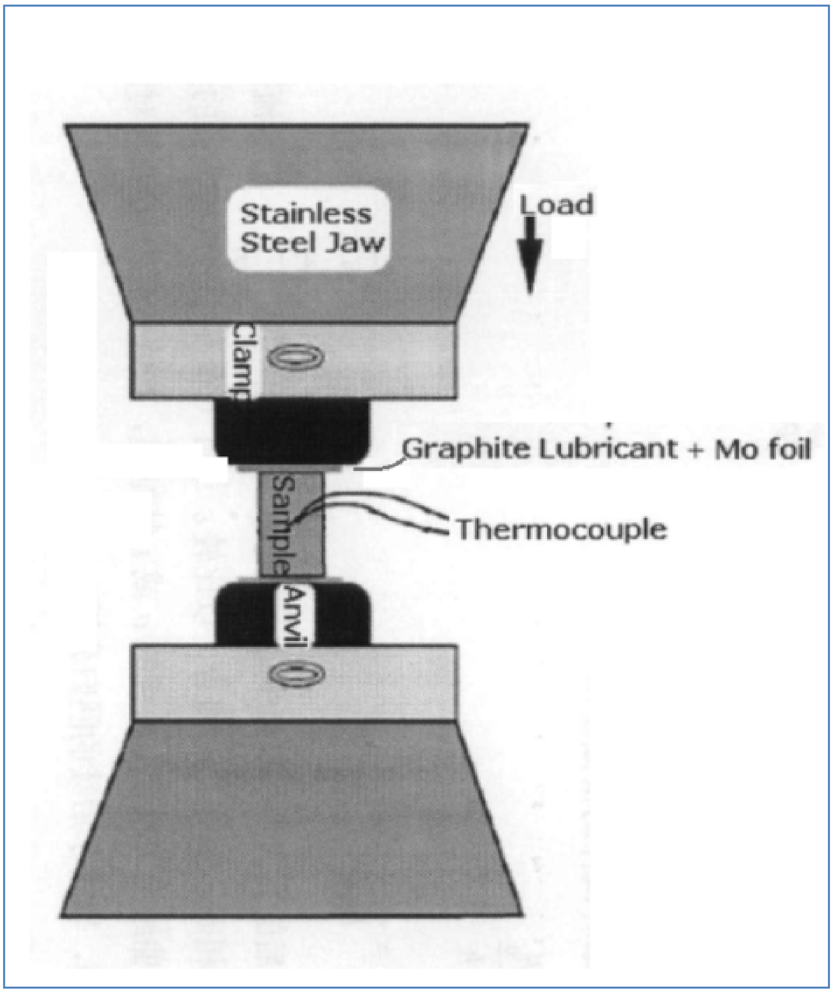

Figure 3.2: Experiment set up of high temperature compression testing using Gleeble 1500

3.5 Density Measurement

Before the powder compacts were sintered, their density (ρ) was determined from their mass (M) and volume (V). The mass of powder compacts was measured by using an electronic balance and the volume of a powder compact was determined by calculation from the diameter and height of the powder compact which were measured using a vernier caliper. This was an approximate measurement method because the surfaces of powder compacts were not very smooth. The equation used to calculate the density of the powder compacts is shown below:

$$\rho = \frac{M}{V} \ldots\ldots\ldots\ldots\ldots\ldots\ldots\ldots\ldots\ldots\ldots\ldots \text{(3.1)}$$

Figure 3.3: The set up used for the density measurement

The density of as-sintered and as-compressed samples was measured based on Archimedes' principle. The set-up used is shown in Figure 3.3 which included a digital weighing balance, a bottle with a bar and a piece of string that was bound to the end of the bar. The sample was bound by using several pieces of string, and then weighted in air water respectively. The density (ρ_a) of the sample was calculated using the following equation:

$$\rho_a = \frac{\mathbf{M1}}{\mathbf{M1-M2}}\rho_w \ldots\ldots\ldots\ldots\ldots\ldots\ldots\ldots\ldots\ldots \text{(3.2)}$$

Where,

M1 is the mass of sample in air, M2 is the mass of sample in water, ρ_w is density of water. The relative density is equal to actual density divided by the theoretical density(ρ_t), as shown in equation 3.3.

$$\text{The relative density} = \frac{\rho_a}{\rho_t} \qquad (3.3)$$

The theoretical density of pure titanium is 4.51 g $/\mathrm{cm}^{-3}$and that of Ti-6Al-4V is 4.46g$/\mathrm{cm}^{-3}$.The porosity level of the sample was calculated using the following equation:

$$\text{The porosity level of sample} = 1 - \frac{\rho_a}{\rho_t} \qquad (3.4)$$

3.6 Optical Microscopy (OM)

In order to observe the microstructure of the thermo-compression testing samples by optical microscope (OM), samples were prepared as follows: By using wire cutting machine, pancake shape thermo-compression testing samples were cut into half to observe its vertical cross-section as shown in Figure 3.4(a). Then, each of the samples was mounted in epoxy resin and then polished to get a mirror surface as shown in Figure 3.4(b). Subsequently, the OM samples were observed using two magnifications of ×50 and ×200.

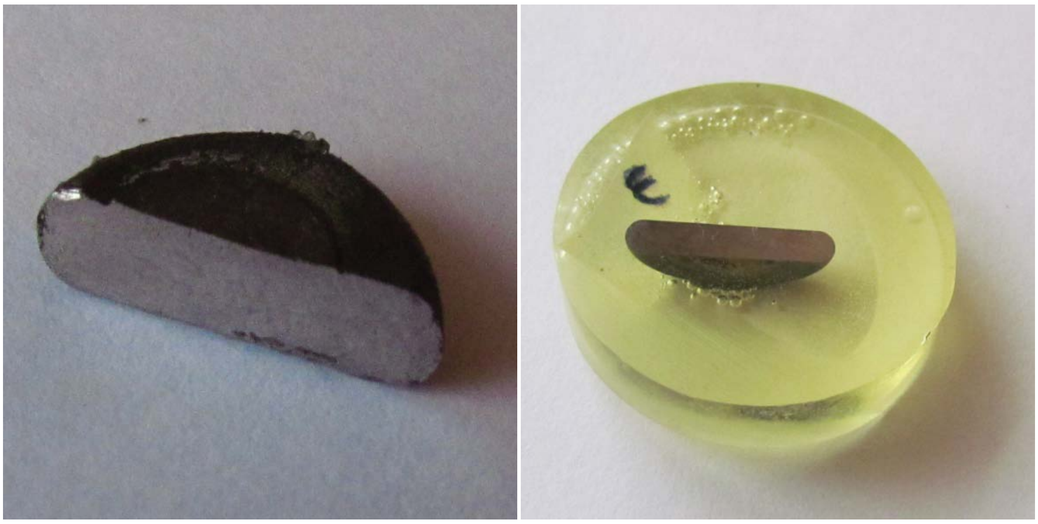
(a) (b)

Figure 3.4: OM sample (a) cut, (b) mounted

Chapter 4: FEM Simulation using ABAQUS

4.1 Introduction

Great improvement in understanding and controlling metal powder forming has been achieved during the past few decades. However, this is a complex process affected by many factors, such as nonlinear properties of material, nonlinear change of stress with strain, complexity of geometry and so on. It is difficult to satisfy the requirements of design by the traditional testing methods. The traditional testing methods not only take a long time to get results, but also consume more material and waste money. Powder metallurgy has been developed to produce complex products. Precision and quality of products have been required to be at high standard. Thus, traditional testing methods do not satisfy the needs of design and research of new material processing. Especially, powder forging and powder extrusion are affected by many factors such as strain rate, temperature distribution, friction, the shapes of die and workpiece, stress and strain, and so on. So far, the constitutive equations of powder forging and powder extrusion have not been agreed on completely. Therefore, powder forming needs more research. FEM simulation of powder forming is needed for to study the process in a greater depth. ABAQUS, as an outstanding FEM simulation software, was used in this work to simulate Ti and Ti-6Al-V powder forging.

4.2 ABAQUS

ABAQUS, as engineering software, has many powerful functions. It can be applied to solve complex linear and nonlinear problems, and includes a cell library which can be used for simulating any random geometry and provided with all kinds of material model databases. Also, most materials can be simulated by ABAQUS, including as metal, rubber, macromolecule material, composite material and armored concrete. Not only can ABAQUS simulate stress and strain, but also other processes, such as heat transfer, mass transfer, coupled thermoelectricity, acoustics and so on. There are a broad range of functions which can be used easily in ABAQUS. In most simulations, the user only need to provide simulation with some engineering data, geometry parameters, material properties, boundary conditions and load behavior[55]. ABAQUS includes two main calculator modules: ABAQUS/Standard and ABAQUS/Explicit as shown in Table 4.1.

Table 4.1: The table of comaring the ABAQUS/Standard with ABAQUS/Explicit[56]

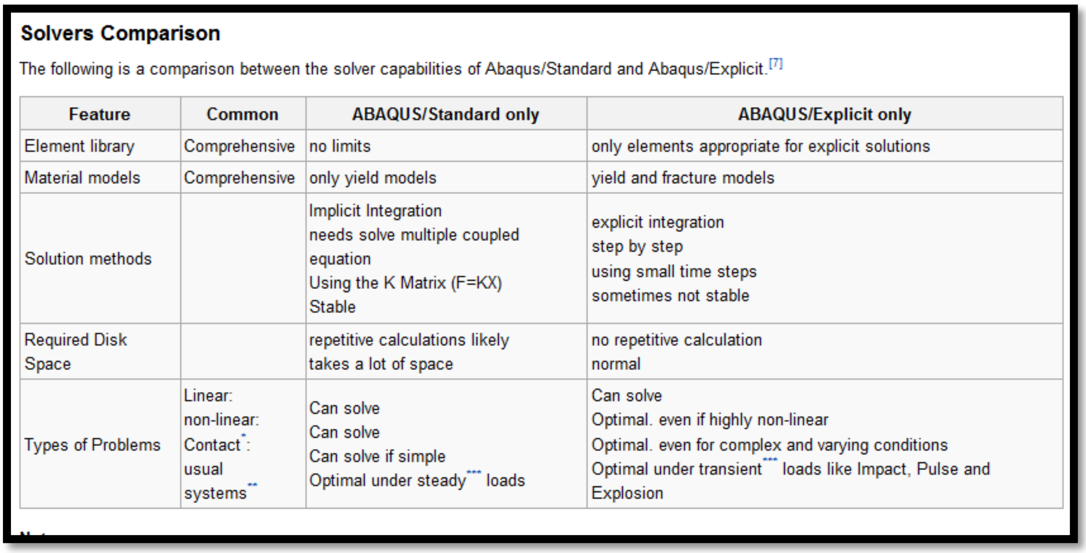

Solvers Comparison

The following is a comparison between the solver capabilities of Abaqus/Standard and Abaqus/Explicit.[7]

Feature	Common	ABAQUS/Standard only	ABAQUS/Explicit only
Element library	Comprehensive	no limits	only elements appropriate for explicit solutions
Material models	Comprehensive	only yield models	yield and fracture models
Solution methods		Implicit Integration needs solve multiple coupled equation Using the K Matrix (F=KX) Stable	explicit integration step by step using small time steps sometimes not stable
Required Disk Space		repetitive calculations likely takes a lot of space	no repetitive calculation normal
Types of Problems	Linear: non-linear: Contact[*]: usual systems[**]	Can solve Can solve Can solve if simple Optimal under steady[***] loads	Can solve Optimal. even if highly non-linear Optimal. even for complex and varying conditions Optimal under transient[***] loads like Impact, Pulse and Explosion

In addition, ABAQUS/CAE, as a computer-aided engineering module, is used for pre-processing, design and modeling machinery, post-processing, and visualizing the result of finite element analysis. On one hand, ABAQUS/CAE can create model easily and define the geometric model with material properties, boundary and load conditions. On the other hand, ABAQUS/CAE can submit and monitor analysis job and then get the output simulation result from input data in its visualization module. To sum up, for ABAQUS finite-element analysis there are mainly three stages mainly as shown in Figure 4.1.

- Pre-processing or modeling: This stage refers to creating an input file which contains an engineer's design for a finite-element analyzer also which is called "solver".

- Processing or finite element analysis: This stage produces an output visual file.
- Post-processing or generating report, image, animation, etc. from the output file: This stage is a visual rendering stage[57].

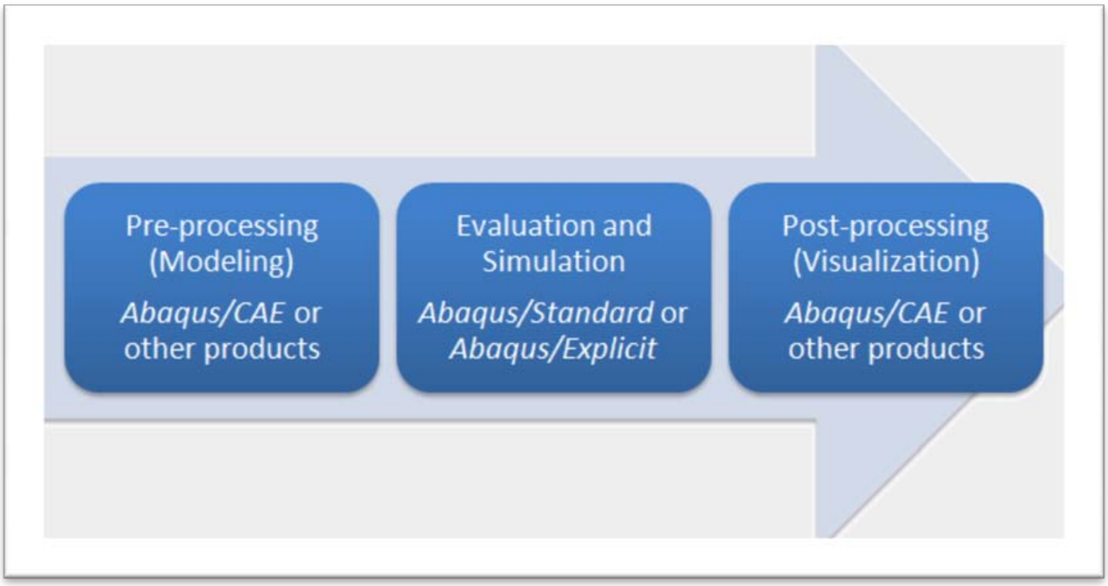

Figure 4.1: The flow chart of ABAQUS

Abacus/CAE is capable of pre-processing, post-processing, and monitoring the processing stage of the solver. The first stage can also be done by other compatible CAD softwares, or even a text editor. ABAQUS/Standard and ABAQUS/Explicit or ABAQUS/CFD are capable of accomplishing the processing stage. Dassault Systemes also produces ABAQUS for CATIA for adding advanced processing and post processing stages to a pre-processor like CATIA[56, 57].

ABAQUS is well-known as one of the most powerful FEM softwares which can be applied to analyze complex solid mechanics products. Specially, it can simulate complex nonlinear problems, and it can simulate both individual parts and the assembly. ABAQUS has been widely used in industry and scientific research, because of its excellent analysis ability and reliability.

4.3 Nonlinear Problems in ABAQUS

Nonlinear means that input data is not proportional to the output data. In fact, almost all mathematical models in physics are nonlinear, and linear analysis is used to simplify models by an approximate calculation which is sufficiently accurate to solve ordinary engineering problems. However, for hot metal forming, it is an extraordinarily complex nonlinear analysis affected by many factors, such as material properties, boundary conditions and geometry factors. Thus, linear analysis is not able to simulate hot metal forming exactly. In order to simulate the whole metal forming process accurately, nonlinear relationship of underlying material behavior, boundary conditions and geometry must be taken into account.

- Nonlinear relationship of material

The majority of metals have linear relationship of stress with strain when the strain is small, but yielding would occur at higher strain. At that time the material would follow a nonlinear relationship of stress with strain.

Furthermore, nonlinear relationship of material is related to many factors, such as temperature, strain rate and so on.

- Nonlinear relationship of boundary

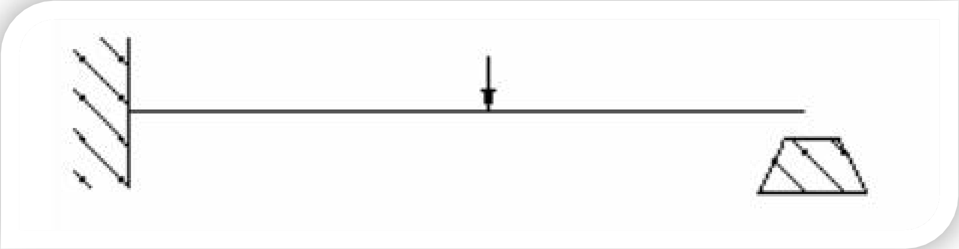

Figure 4.2: A picture of a nonlinear sample

Nonlinear relationship of boundary occurs in concomitance with change of analysis procedure. For example, in a situation shown in Figure 4.2, before the beam contacts the barrier, the vertical deflection of the end of the beam has a linear relationship with the load. However, once the beam contacts the barrier, the boundary conditions changed hugely and the vertical deflection of the end of beam has a nonlinear relationship with the load.

- Nonlinear relationship of geometry

Rigidity changed by geometry deformation can be classified into geometry nonlinear relationship. Nonlinear relationship of geometry can be divided into three aspects:

1. Large strain
2. Large deflection
3. Stress rigidization

There are three phenomena related to nonlinear relationship of geometry.

a) If the element shape, area and thickness are changed, the rigidization of element would be changed.

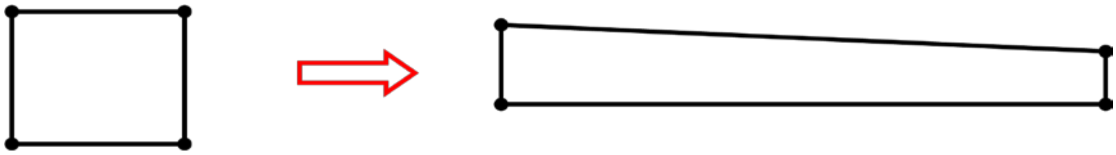

Figure 4.3: Another picture of nonlinear sample

b) If the element orientation is changed, the rigidization of element would be changed.

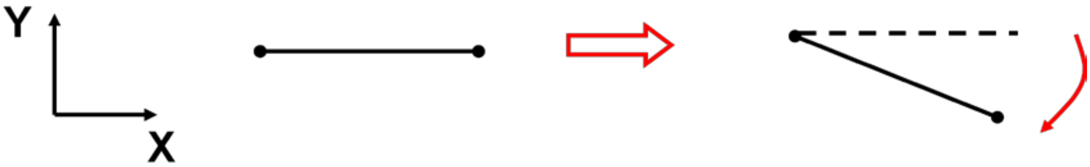

Figure 4.4: The third picture of a nonlinear sample

c) If the element is uder a higher surface internal stress, the surface normal rigidization would be affected obviously.

To sum up, large strain consists of these three phenomena. Large deflection consists of the second and third phenomena. Stress rigidization is only related to the third phenomenon.

4.4 Material Model Constitutive Equations in ABAQUS[58]

In order to simplify and deal with the calculation model, the material properties and processing need be assumed by some special conditions in powder forming analysis. For EVP FEM, there are three given conditions. Bauschinger effect is ignored in plastic deformation, the material is homogeneous; and gravity and inertia of the material is ignored. Accordingly, in ABAQUS, the material model constitutive equations were written as follows:

The strain rate decomposition is

$$\varepsilon = \varepsilon^{el} + \varepsilon^{pl} \ldots\ldots\ldots\ldots\ldots\ldots\ldots\ldots\ldots\ldots\ldots\ldots \text{(4.1)}$$

Where, ε is strain, ε^{el} is elastic strain , ε^{pl} is plastic strain.

$$K = \frac{E}{3(1-2v)}, \quad G = \frac{E}{2(1+v)} \ldots\ldots\ldots\ldots\ldots\ldots \text{(4.2-4.3)}$$

Where, K is bulk modulus. G is shear modulus. E is Young's modulus. v is Poisson's ratio.

The elasticity is written in volumetric and deviatoric components as follows

Volumetric:

$$p = -K\varepsilon_{vol} = -\frac{1}{3}trace(\sigma) \ldots\ldots\ldots\ldots\ldots\ldots \text{(4.4)}$$

Where, p is the equivalent pressure stress. ε_{vol} is volume strain.

Deviatoric:

$$S = 2\text{G}\, e^{el} = \sigma + pI \ldots\ldots\ldots\ldots\ldots\ldots\ldots\ldots\ldots \text{(4.5)}$$

The flow rule is

$$de^{pl} = d\bar{e}^{pl}n \ldots\ldots\ldots\ldots\ldots\ldots\ldots\ldots\ldots \text{(4.6)}$$

Where, $n = \frac{3S}{2q}$, $q = \sqrt{\frac{3}{2}S{:}S}$. e^{-pl} is the equivalent plastic strain rate.

If the material is rate independent, this is the yield condition:

$$q = \sigma^0(\bar{e}^{pl}, \theta) \ldots\ldots\ldots\ldots\ldots\ldots\ldots\ldots\ldots \text{(4.7)}$$

Where σ^0 is the yield stress and is defined by the user as a function of equivalent plastic strain ($\bar{e}^{pl}$) and temperature (θ). If the material is rate dependent, the uniaxial flow rate is defined as:

$$\dot{\bar{e}}^{pl} = h\,(q, \bar{e}^{pl}, \theta) \tag{4.8}$$

Where h is a known function. For example, the rate-dependent material model offers an overstress power law model of the form

$$\dot{\bar{e}}^{pl} = D\,(\frac{\mathrm{q}}{\sigma^0} - 1)^{\mathrm{n}}$$

Where D (θ) and n(θ) are user-defined temperature-dependent material parameters and $\theta^0(\bar{e}^{pl}, \theta)$is static yield stress. Integrating this relationship by the backward Euler method gives

$$\Delta\bar{e}^{pl} = \Delta t\; h\,(\mathrm{q}, \bar{e}^{pl}, \theta) \tag{4.9}$$

Thus, both the rate-independent model and the rate dependent model give the general uniaxial form

$$q = \bar{\sigma}(\bar{e}^{pl}) \tag{4.10}$$

Equations (4.1) to (4.10) define the material behavior. In any increment when plastic flow occurrs these equations must be integrated and solved for the state at the end of the increment. The integration is done by applying the backward Euler method to the flow rule (Equation 4.6), giving

$$\Delta e^{pl} = \Delta e^{-pl}\mathrm{n} \tag{4.11}$$

Combining this with the deviatoric elasticity (Equation 4.5) and the integrated strain rate decomposition (Equation 4.1) gives

$$S = 2G(e^{el}|_{\,t} + \Delta e - \Delta\bar{e}^{\;pl}\;\; n) \tag{4.12}$$

Using the integrated flow rule (Equation 4.11), together with the Mises definition of the flow direction, (in Equation 4.6) this becomes

$$\left(1 + \frac{3G}{q}\Delta\bar{e}^{pl}\right)S = 2G(e^{el}|_t + \Delta e) \tag{4.13}$$

For simplicity of notation we write

$$\hat{e} = e^{el}|_t + \Delta e \tag{4.14}$$

so that this equation is

$$\left(\,1 + \frac{3G}{q}\Delta\bar{e}^{\,pl}\right)S = 2G\hat{e} \tag{4.15}$$

Taking the inner product of this equation with itself gives

$$q + 3G\Delta\Delta\bar{e}^{\,pl} = 3G\tilde{e} = 3G\sqrt{\frac{2}{3}\hat{e}:\hat{e}} \tag{4.16}$$

The Mises equivalent stress, q, must satisfy the uniaxial form defined in Equation 4.10

$$3G(\tilde{e} - \bar{e}^{pl}) - \bar{\sigma} = 0 \ldots\ldots\ldots\ldots (4.17)$$

This is a nonlinear equation for $\bar{e}^{pl}$ in the general case when $\bar{\sigma}$ depends on the equivalent plastic strain (that is, when the material is rate-dependent, or when there is nonzero work hardening). (It is linear in Δe^{pl} for rate-independent perfect plasticity.) We solve it by Newton's method:

$$e^{pl} = \frac{3G(\tilde{e} - \Delta\bar{e}^{pl} - \bar{\sigma})}{3G + H} \ldots\ldots\ldots\ldots (4.18)$$

Where, $H = \frac{d\bar{\sigma}}{d\bar{e}^{pl}}$, $\Delta\bar{e}^{pl} = \Delta\bar{e}^{pl} + e^{pl}$ .The cacultion iterates until convergence is achieved.

Once $\Delta\bar{e}^{pl}$ is known, the solution is fully defined: using Equation 4.7,

$$q = \bar{\sigma} \ldots\ldots\ldots\ldots (4.19)$$

and so, from Equation 4.15, we have

$$S = \frac{2G}{1 + \frac{3G}{Q}\Delta\bar{e}^{pl}}\hat{e} \ldots\ldots\ldots\ldots (4.20)$$

From Equation 4.6, we have

$$n = \frac{3S}{2q} \ldots\ldots\ldots\ldots (4.21)$$

and thus, from Equation 4.9, we have

$$\Delta e^{pl} = \Delta\bar{e}^{pl}\,\mathrm{n} \ldots\ldots\ldots\ldots (4.22)$$

For cases where three direct strain components are provided by the kinematic solution, Equation (4.4).can be changed to

$$p = -K\varepsilon_{vol} \ldots\ldots\ldots\ldots (4.23)$$

so that the solution is then fully defined.

4.5 Thermal-stress Analysis of Powder Forming in ABAQUS

In powder forming, thermal-stress analysis is very complex. The heat flow through conduction occurs with varying thermal field. There are three important considerations that need to be made:

1. There is a temperature gradient in workpiece, die and surrounding. In the

powder hot forming, the heat exchange occurred by conduction and radiation.

2. The heat can be originated from the friction between workpiece and die during the hot forming process.
3. Thirdly, the heat can be generated from metal deformation energy. In turn, the change of temperature can even affect material deformation ability at high temperatures. Accordingly, it is very essential to study the relationships between temperatures, stress and strain.

The thermal stress analysis can be considered as analysis of the transient state, as a result of all kinds of conditions which change with time. In ABAQUS, there are two computation modules, ABAQUS/Standard and ABAQUS/Explicit, which involve the difference-integral methods based on time domain, and the approximate finite element method based on spatial domain. In ABAQUS, the constitutive equations of heat and stress can be solved together.

As shown in Figure 4.5, a metal workpiece is placed in a surrounding, and the density, volume and surface area of the metal are defined with ρ, V and S respectively.

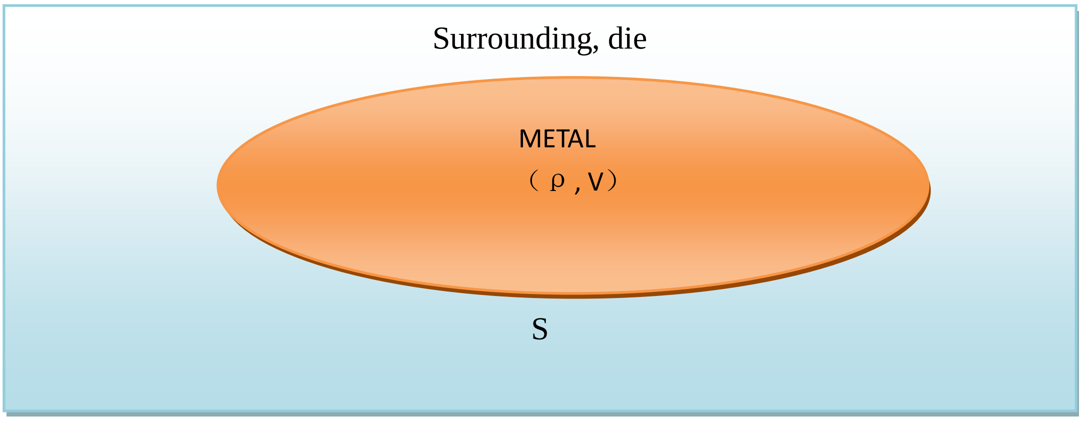

Figure 4.5: A schematic diagram showing heat transfer between metal and surrounding

The energy balance equation is:

$$\int_v \rho \, \dot{U} \quad dv = \int_s q \; ds + \int_v r \quad dv + \int_V r^{pl} \, dv \ldots\ldots\ldots\ldots\ldots.. \text{(4. 24)}$$

Where $\dot{U}$ is the material time rate of the internal energy;

q is the heat flux per unit area of the body, flowing into the body;

r is the heat supplied externally into the body per unit volume.

r^{pl} is heat energy as a result of plastic deformation

$$\dot{U} = \frac{\partial U}{\partial t} \quad \text{.................................... (4. 25)}$$

Where U is internal energy as a unit mass

From equations 4.24 and 4.25, we have

$$\int_v \rho \, \frac{\partial U}{\partial t} \, dv = \int_s q \, ds + \int_v r \, dv + \int_v r^{pl} \, dv \quad \text{.................... (4. 26)}$$

$$\text{and, } \int_v \rho \, \Delta U \, dv = \int_s q \, \Delta t \, ds + \int_v r \, \Delta t \, dv + \int_v r^{pl} \Delta t \, dv \quad \text{........ (4. 27)}$$

In equation 4.27, $\int_v \rho \, \Delta U \, dv$ is the heat energy increment of the metal in Δt , $\int_s q \, \Delta t \, ds$ is the heat energy increment from surrounding into metal surface in Δt, $\int_v r \, \Delta t \, dv$ is the heat energy increment from surrounding into metal body in Δt , and $\int_v r^{pl} \Delta t \, dv$ is the heat energy increment as a result of plastic deformation in Δt.

The heat transfer equations are related to time and space which have no steady values without boundary conditions. Thus, boundary conditions must be defined. There were five major boundary conditions.

The first boundary condition: prescribed temperature of metal as a function of t.

$$\theta_0(x, y, z, t)|_{t=o} = \theta \; (x, y, z, t) \quad \text{................... (4.28)}$$

Where θ is temperature, θ_0 is initial temperature.

The secondly boundary condition: prescribed surface heat flux as a function of t.

$$q_0(x, y, z, t)|_{t=o} = q \; (x, y, z, t) \quad \text{........................... (4.29)}$$

The thirdly boundary condition: prescribed volumetric heat flux as a function of t.

$$r_0(x, y, z, t)|_{t=o} = r \; (x, y, z, t) \quad \text{........................... (4.30)}$$

The fourth boundary condition: surface convection

$$q = h(\theta - \theta^*) \text{ ……………………….…….. (4.31)}$$

Where h= h_0 (x, y, z, t) is the film coefficient and θ^* is the sink temperature.

a) The fifth boundary condition: radiation.

$$q = A((\theta - \theta^z)^4 - ((\theta^* - \theta^z)^4) \text{ ………………….. (4.32)}$$

Where A is the radiation constant (emissivity times the Stefan-Boltzmann constant) and θ^z is the absolute zero on the temperature scale used.

4.6 Friction model

In physics, the coefficient of the kinetic friction is defined as the ratio of friction force between two parts and the normal pressure. The coefficient of friction is material intrinsic. For example, the coefficient of friction between ice and steel is very low. Meanwhile, the coefficient of friction between copper and cast iron is high, about 1.05. On the other hand, the coefficient of friction is affected by the surface roughness. In the rigid model, the materials are considered as the rigid body which is not able to be deformed under any circumstance. In the metal plastic forming, there is a high pressure between the die and the workpiece. There are some special dynamic conditions in this process, for instance, large plastic deformation. Due to the plastic deformation and the friction between die and workpiece, the temperatures of the die and the workpiece can be increased, and the materials properties would be changed accordingly. In addition, the lubricant, which is the substance placed at the workpiece/die interface to reduce friction is also affected by many conditions, temperature, degree of homogeneity, viscosity and so on. So far, generally speaking, there are two methods used to study friction during metal plastic forming.

1. The coulomb friction law:

$$\tau_f = \mu\sigma_n \text{……………………………..………….. (4.33)}$$

Where τ_f is the friction stress,

μ is the coefficient of the coulomb friction,

σ_n is the normal stress.

This is used in the metal cold forming usually.

2. The constant friction law:

$$\tau_f = mk = m\ \frac{\sigma_s}{\sqrt{3}} \text{ ………………………..………….. (4.34)}$$

Where τ_f is the friction stress,

m is the the friction factor(0<m<1),

k is the shear yield strength，

σ_s is the true stress.

This equation is used to analyse metal hot forming, for example, hot forging and hot extrusion. However, the precision of these methods is not sufficiently high to anaylse complex models in metal hot forming. Thus, it is important to study more accurate model in order to enhance the simulation result. So far, two new models are often applied.

(a) τ_f =mkv………………………………………………….……….. (4.35)

Where τ_f is the friction stress,

v=dimensionless relative velocity= (v_w-v_d) v_r

v_w= workpiece velocity,

v_d= die velocity,

v_r= vertical ram velocity.

(b) The arc tangent friction model

$$f = -mk[\arctan(\frac{v_s}{A})] \text{ ………………………..……………….……….. (4.36)}$$

Where f is the friction force,

m is friction factor,

k is the shear yield strength,

v_s is relative velocity between die and workpiece

A=a positive number which get usually 10^{-3}～10^{-5}.

4.7 Simulation Model Setup in ABAQUS

This study focuses on the upsetting process of titanium based powder compacts.

The simulation involves coupled temperature-displacement analysis of a viscoplastic problem. In this study, small cylindrical powder compacts of Ti-6Al-4V alloy were reduced in length by 70%-80%.The initial temperature of the powder compacts was considered as 1050 °C-1150°C.

4.7.1 Geometric Model

In this study, all geometric parts were designed by using SolidWorks software in the first place, and then input the data into ABAQUS. As a result of this process, SolidWorks software was used as professional and advanced 3D design software. The object of simulation was a hot-forging model as shown in Figure 4.6: a circular powder compact with 30 mm high and a radius of 20 mm; and then compressed between flat, rough, elastic open dies with 10 mm thickness and a radius of 100mm.

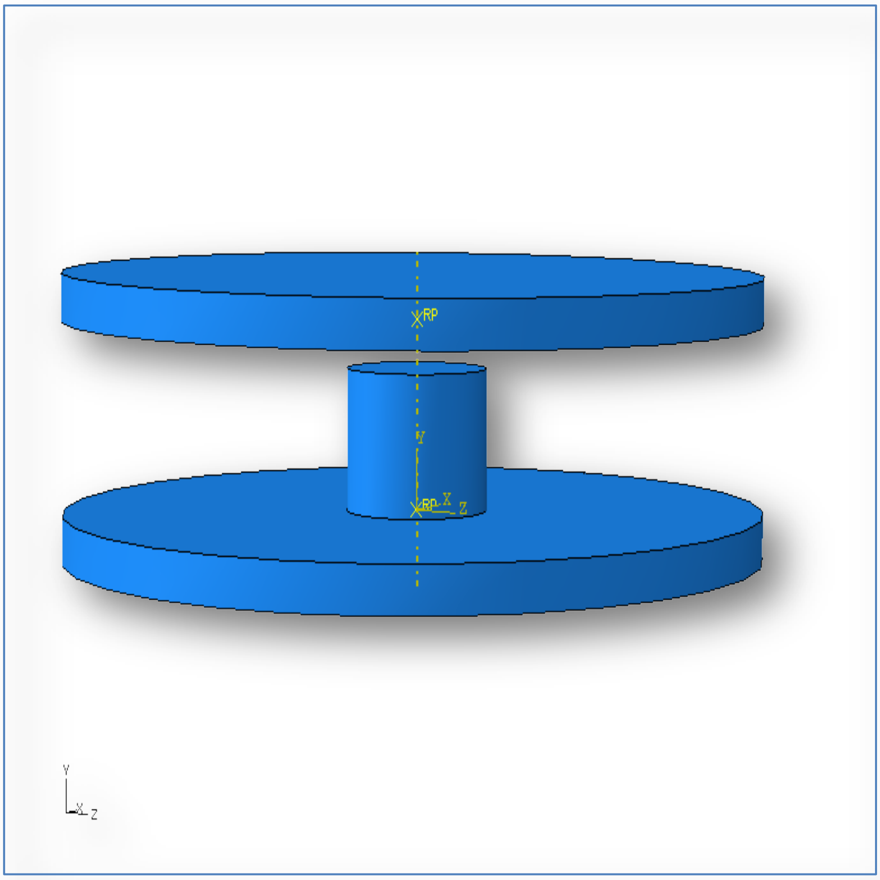

Figure 4.6: The 3D-assemble picture of the whole simulation model

All surfaces of the powder compacts have heat transferred with all contact surfaces of dies and atmosphere. In addition, this model is axisymmetric, and thus, only half of the compact and dies was studied, as shown in Figure 4.7. The whole body can be constructed by rotating a planar surface which is the cross-section along the centerline of powder compacts by 180° about the centerline.

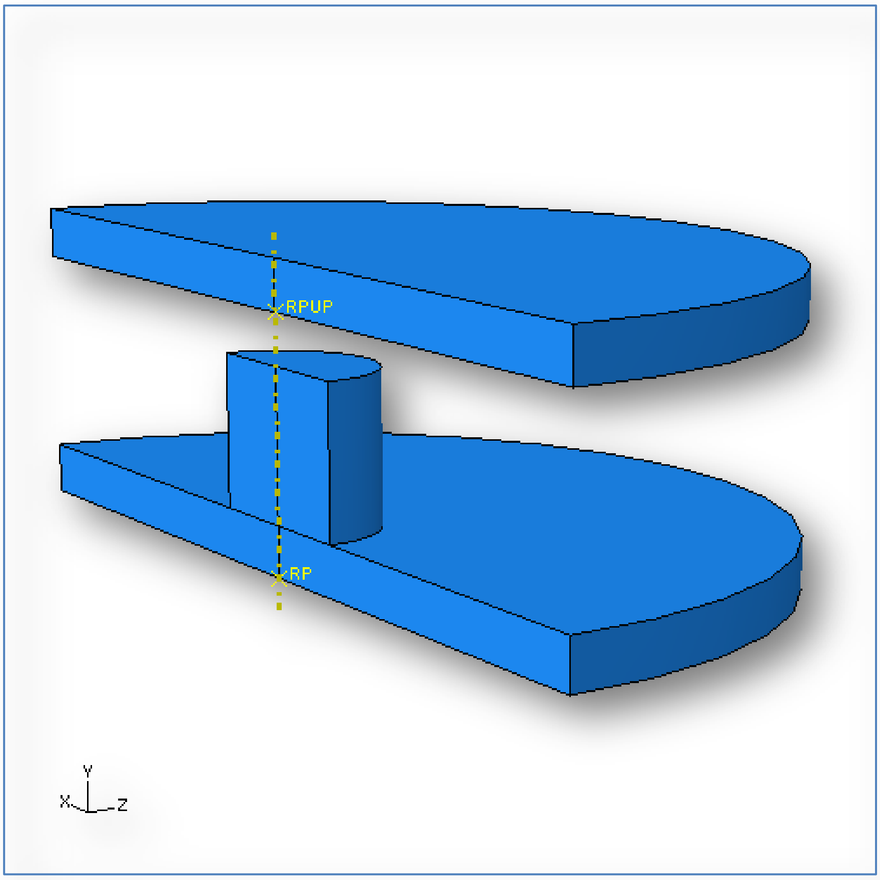

Figure 4.7: The 3D-assemble picture of the actual simulation model

4.7.2 Mesh

In the process of simulation, a calculation method called “the elements of type C3D8T”, which is an 8-node thermally coupled brick, trilinear displacement and temperature that allowed for fully coupled temperature-displacement analysis[59],was used in this study. A regular mesh with six elements in each direction was used, as shown in Figure 4.8.

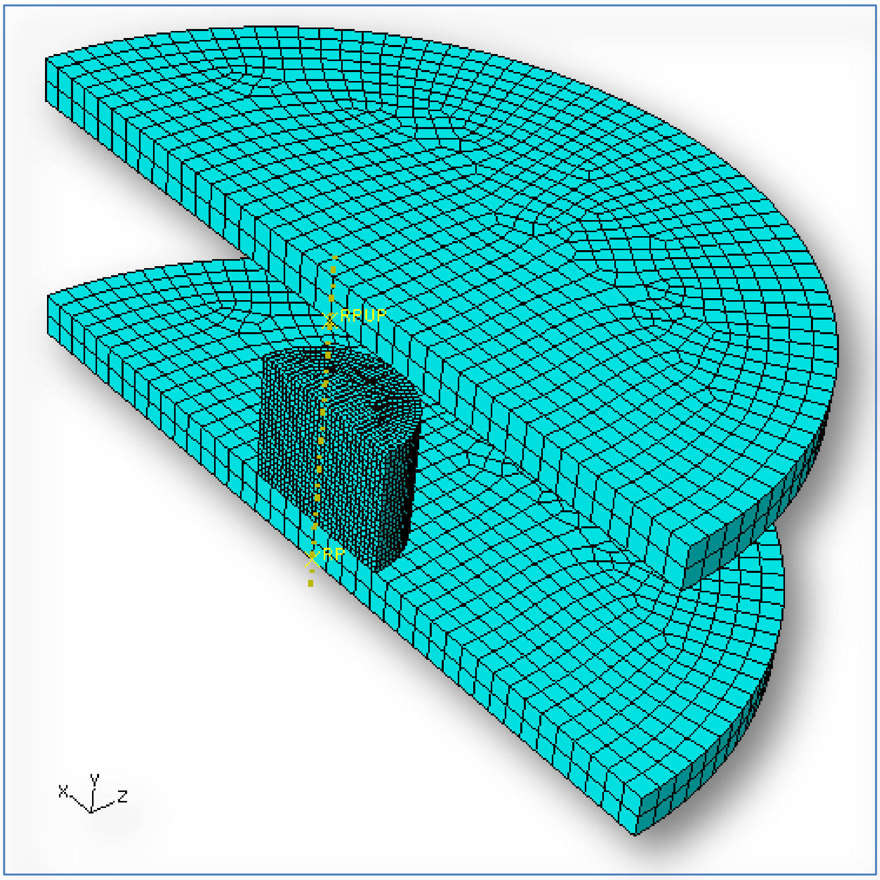

Figure 4.8: The 3D picture of the actual simulation model meshed

4.7.3 Interaction

The contacts between the top and low die surfaces and the exterior surfaces of the billet were modeled with the *CONTACT PAIR option as show in Figure 4.9. One of the contact pairs is called surface “die A” and surface “body up”; another is called surface “body-down” and surface “die B”. In these contact pairs, there were two important factors that need to be considered. On one hand, the contact surfaces are assumed to be rough frictional contact. The friction coefficient can be set by using different values to analyze different frictional influence. On the other hand, the conductivity of contact pairs are set as a result to show that there are heat transferred between contact pairs. In this study, the powder compacts were placed in 20^{o}C atmosphere, and a surface film condition option was used with the film coefficient being set to 100.

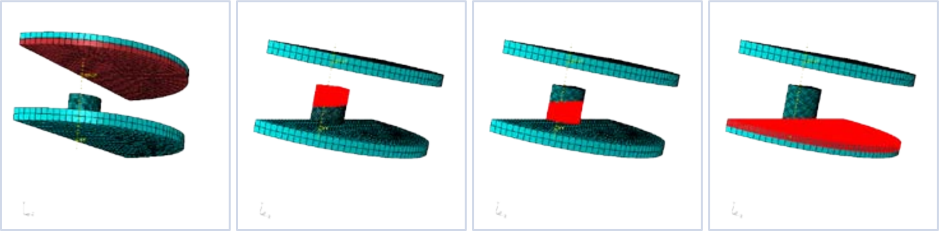

(a) (b) (c) (d)

Figure 4.9: The contact surfaces of the model (a) Surface die A, (b) Surface bodyup, (c) Surface bodydown, (d) Surface die B

4.7.4 Material

In this experiment, the powder compacts of titanium and Ti-6Al-4V powders were used in simulation. The majority of material parameters are based on the gleeble compression testing, except some standard properties of titanium and Ti-6Al-4V powder. In addition, their initial relative density can be calculated from the density measurement. The properties of H13 steel were used as material parameters of dies. The material properties used in the simulation are listed in Table 4.2.

Table 4.2: The major materials parameteres used in the simulation

	Titanium	Ti-6AL-4V	H13
Conductivity	19.3 at 200 ^{o}C	7.3 at 93 ^{o}C	48 W/(m.k)
	18 at 600 ^{o}C	23.5 at 950 ^{o}C	
Specific heat	503 at 100 ^{o}C	550 at 100 ^{o}C	450 J/(kg.K))
	670 at 600 ^{o}C	950 at1000 ^{o}C	
Expansion	8.42E-005 /Kelven	8.42E-005 /Kelven	1.2E-005/Kelven
Density	4.5g/cm^{-3}	4.43 g/cm^{-3}	7.85g/cm^{-3}
Elastic	Compression testing	Compression testing	209GPa
Poisson's Ratio	Compression testing	Compression testing	0.28
Plastic	compression testing	Compression testing	none
Relative density	density measures	density measures	100%

4.7.5 Step

In ABAQUS program, the type of the load and boundary condition put on the part as input data is selected, and the interaction is set up by the options of type, number, time, response and Nlgeom. In this simulation model, two steps were created, namely initial step and step 1, coupled temp-displacement was selected in the type of loading and boundary conditions. The time period of compression process was chose as the same as that in simulation plan. The response option was selected as transient as the result, the results of simulation were monitored anytime. As a typical nonlinear problem, Nlgeom was chose in the model.

4.7.6 Load

The values of load, boundary condition, and predefined temperature were applied in the load model, which are step-dependent objects, which meant that the simulation conditions were applied in each step. In this simulation, some elements and nodes of model were set as shown in Figure 4.10 before the values of boundary conditions and loading were applied. Then, the predefined temperatures of die and billet were set at 50°C ~1150°C depended on simulation plan in initial step which nodes and elements were shown in Figure 4.10(a), (b) and (c),.

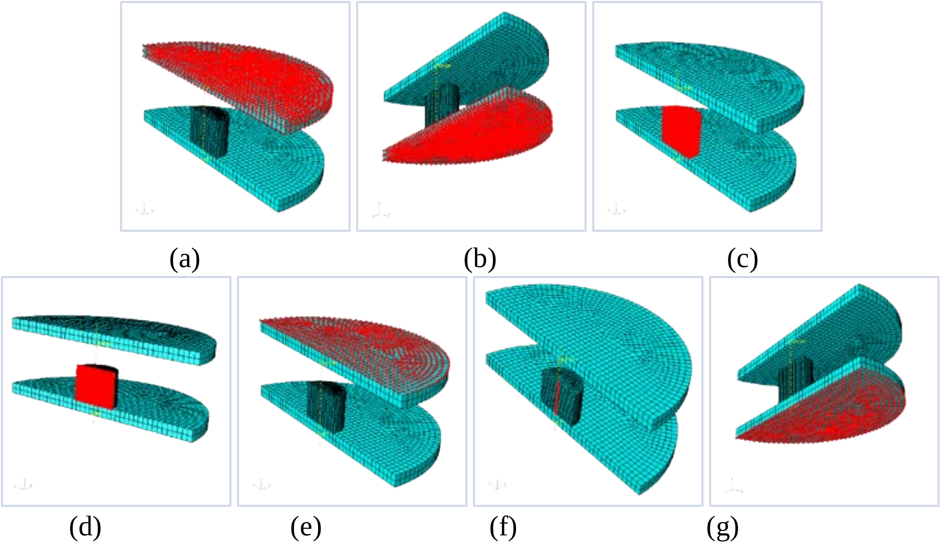
(a) (b) (c)
(d) (e) (f) (g)

Figure 4.10: The drawing of site of some sets(a)Up die, (b)Down die, (c)Body, (d)Sr, (e)Top, (f)M, (g)Bot

In addition, in ABAQUS program, the freedoms of displacement and rotation were named as follows: U1 is displacement in the X-direction; U2 is displacement in the Y-direction and U3 is displacement in the Z-direction. And, UR1 is rotation around X-axis; UR2 is rotation around Y-axis and UR3 is rotation around Z-axis as shown in Figure 4.11.

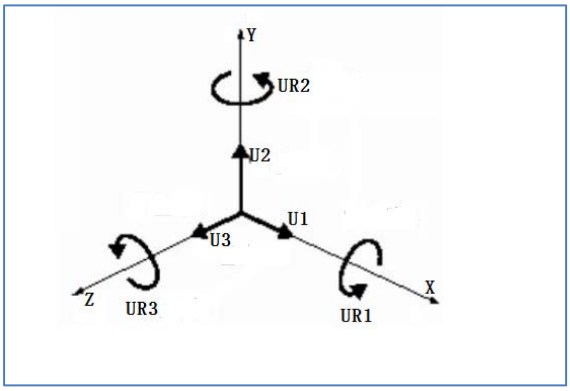

Figure 4.11: The freedoms of displacement and rotation

In the simulation model, the boundary conditions of some sets in initial step and step 1 were set up as follows:

Initial step:

“Sr”, which nodes and elements were shown in Figure 4.10(d):U3=UR2=UR1=0. Here, U3=0 means that “Sr” is restricted in the Z-direction, and UR2=0 means that “Sr” is restricted rotation around Y-axis; “M”, which nodes were shown in Figure 4.10(f): U1=UR3=UR1=UR3=0; “Bot”, which nodes and elements were shown in Figure 4.10(g):U1=U2=U3=UR1=UR2=UR3=0.

Step 1:

“Sr”:U3=UR2=UR1=0;“M”:U1=UR3=UR1=UR3=0;

“Bot”:U1=U2=U3=UR1=UR2=UR3=0.

“Top”, which nodes and elements were shown in Figure 4.10(e): U1=U3= UR1=UR2=UR3=0.U2=-21mm.

4.7.7 Simulation plans

After boundary conditions and load were applied, the basic upsetting model of titanium and Ti-6AL-4V powder compacts upsetting was built up. There were nine simulation models built up as shown in Table 4.3. The model B was selected as a reference. By comparing the results of model B with the other models, the effect of the amount of deformation, strain rate, initial temperature of billet, friction coefficient, initial temperature of die and four materials of the upsetting on the output results from simulation were discussed in the next chapter.

Table 4.3: The table of simulation plan

Model	Sample	Friction coefficient	Time(s)	Deformation degree	Ts(^oC)	Td(^oC)	Ta(^oC)
A	E	0.4	7	50%	1050	500	20
B	E	0.4	7	70%	1050	500	20
C	E	0.4	2	70%	1050	500	20
D	E	0.4	7	70%	1150	500	20
E	E	0.8	7	70%	1050	500	20
F	E	0.4	7	70%	1050	50	20
G	A	0.4	7	70%	1050	500	20
H	C	0.4	7	70%	1050	500	20
I	F	0.4	7	70%	1050	500	20

Chapter 5: Results and Discussion

5.1 Powder compacting

By uniaxial pressing, the densities of the powder compacts attained were in the range of 87%-93% of the theoretical density of titanium (4.5g/ $\mathbf{cm^3}$) and Ti-6Al-4V (4.43g/ $\mathbf{cm^3}$) respectively, as shown in Table 5.1. The densities of the majority of powder compacts were above 90%. The density of the sample E was the smallest and the density of sample D was the biggest. Theoretically, the densities of all powder compacts should be same since they had the same compacting conditions. However, in reality, it was difficult to keep the same conditions completely for all samples.

Table 5.1: The table of the densities of powder compacts

Sample	M(g)	V(cm^3)	$\rho_a(g/cm^3)$	$\rho_t(g/cm^3)$	RD	Porosity
A(Titanium)	159.9	39.352	4.063	4.50	0.902944	0.097056
B(Titanium)	158.8	38.159	4.162	4.50	0.924783	0.075217
C(Titanium)	158	38.672	4.086	4.50	0.907913	0.092087
D(Titanium)	158.8	38.001	4.179	4.50	0.928628	0.071372
E(Ti-6Al-4V)	158.4	41.235	3.841	4.43	0.867115	0.132885
F(Ti-6Al-4V)	159.3	38.804	4.105	4.43	0.926685	0.073315
G(Ti-6Al-4V)	159.8	39.900	4.005	4.43	0.904066	0.095934
H(Ti-6Al-4V)	159.6	39.071	4.085	4.43	0.922076	0.077924

In addition, there were two example pictures for Ti-6Al-4V compact geometry and dimensions as shown in Figure 5.1.

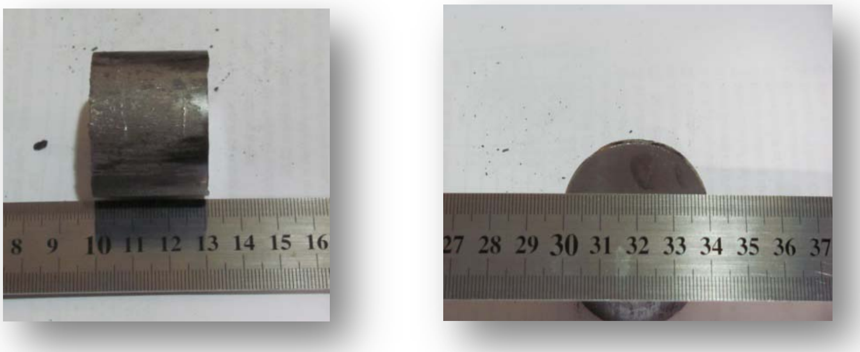

(a) (b)

Figure 5.1: Images of a Ti-6Al-4V powder compacts a) Side view, b) Top view

5.2 Sintering

The densities of powder compacts after sintering are shown in Table 5.2. The densities of all samples were increased by 2~3% during sintering, as shown by comparing Table 5.1 and Table 5.2. Theoretically, the densities should have increased with increasing sintering temperature and holding time. However, this was not always the case. Possibly, it was related to the low accuracy of the density measurement of pre-sintered powder compacts.

Table 5.2: The densities of sintered powder compacts

Sample	M1(10^{-4}g)	M2(10^{-4}g)	ρ_a(g/cm^3)	ρ_t(g/cm^3)	RD	porosity
A(Titanium)	24268	18516	4.219083	4.5	0.937574	0.062426
B(Titanium)	24443.5	18688	4.247118	4.5	0.943804	0.056196
C(Titanium)	24707.5	18909.5	4.261353	4.5	0.946967	0.053033
D(Titanium)	24700	18915	4.269564	4.5	0.948792	0.051208
E(Ti-6Al-4V)	22340.5	16695	3.957212	4.43	0.893276	0.106724
F(Ti-6Al-4V)	25767.5	19702	4.248332	4.43	0.958991	0.041009
G(Ti-6Al-4V)	24142	18209.5	4.070959	4.43	0.918952	0.081048
H(Ti-6Al-4V)	24791.5	18837.5	4.163818	4.43	0.939914	0.060086

The compression testing samples were prepared and then marked with label numbers. A picture of compression testing sample is shown in Figure 5.2 from which it can be seen that it has a very glaze outer surface which is the necessary condition to get exact results of high temperature compression testing .

Figure 5.2: Picture of compression testing sample

5.3 High temperature compression testing

The densities of samples after compression testing are recorded in Table 5.3. The densities of the majority of samples were above 99%.In addition, there were some visible trends. Firstly, the density increased with increasing compression testing temperature. Secondly, the density increased with decreasing strain rate. Thirdly, these two trends were similar to the trend of the change of flow stress with temperature and strain rate. In addition, before the writing of this thesis was finished, the samples of group A,C,E and F had just been done and then put back in original bags. A picture of a sample after compression testing, as shown in Figure 5.3 from which it can be seen that every finished sample had a thin pancake shape. The compressive true stress-true strain curves of samples are shown in Figure 5.4. These curves were the basis of simulation. The difference of group A, C, E and F samples was materials and sintering conditions, respectively. Samples in group A and group C were made from titanium powder sintered at 1200^{o}C. The samples in group A were induction sintered without holding time while those in group C were sintered with 5 minutes holding time. The samples in group E and F were made from Ti-6Al-4V powder. The samples in group E were sintered at1200^{o}C, while those in group F were sintered at 1300^{o}C, without holding time.

Table 5.3: The densities of all samples after compression testing

Sample	M1(10^{-4}g)	M2(10^{-4}g)	ρ_a(g/cm^3)	ρ_t(g/cm^3)	RD	Porosity
A(1000^{o}C,0.01/s)	24918	19375	4.4954	4.5	0.998978	0.001022
A(1000^{o}C, 1/s)	24735	19210	4.476923	4.5	0.994872	0.005128
A(1000^{o}C,0.01/s)	28924	22491	4.496192	4.5	0.999154	0.000846
A(1100^{o}C, 1/s)	25015	19429	4.47816	4.5	0.995147	0.004853
A(1200^{o}C, 1/s)	24520	19071	4.499908	4.5	0.99998	2.04E-05
C(1000^{o}C,0.01/s)	24832	19298	4.48717	4.5	0.997149	0.002851
C(1000^{o}C,0.1/s)	24671	19170	4.484821	4.5	0.996627	0.003373
C(1000^{o}C, 1/s)	25535	19807	4.457926	4.5	0.99065	0.00935
C(1100^{o}C,0.01/s)	31214	24165	4.428146	4.5	0.984032	0.015968
C(1100^{o}C, 1/s)	24791	19232	4.459615	4.5	0.991026	0.008974
C(1200^{o}C,1/s)	24494	19021	4.475425	4.5	0.994539	0.005461
E(1000^{o}C,0.01/s)	22187	17032	4.303977	4.43	0.971552	0.028448
E(1000^{o}C,0.1/s)	23127	17685	4.249724	4.43	0.959306	0.040694
E(1000^{o}C,1/s)	22670	17190	4.136861	4.43	0.933829	0.066171
E(1100^{o}C,0.01/s)	22738	17507	4.346779	4.43	0.981214	0.018786
E(1100^{o}C,0.1/s)	22218	17083	4.326777	4.43	0.976699	0.023301
E(1100^{o}C,1/s)	22190	16930	4.218631	4.43	0.952287	0.047713
E(1200^{o}C,0.01/s)	22802	17620	4.400232	4.43	0.99328	0.00672
E(1200^{o}C,0.1/s)	22956	17675	4.346904	4.43	0.981242	0.018758
E(1200^{o}C,1/s)	23109	17748	4.310576	4.43	0.973042	0.026958
F(1000^{o}C,0.01/s)	25734	19875	4.392217	4.43	0.991471	0.008529
F(1000^{o}C, 1/s)	25817	19908	4.369098	4.43	0.986252	0.013748
F(1100^{o}C,0.01/s)	26124	20194	4.405396	4.43	0.994446	0.005554
F(1100^{o}C,0.1/s)	26230	20283	4.410627	4.43	0.995627	0.004373
F(1100 ^{o}C,1/s)	26006	20033	4.353926	4.43	0.982828	0.017172
F(1000^{o}C,0.01/s)	26620	20595	4.418257	4.43	0.997349	0.002651
F(1000^{o}C,1/s)	25734	19825	4.355052	4.43	0.983082	0.016918

Figure 5.3: Picture of a sample after compression testing

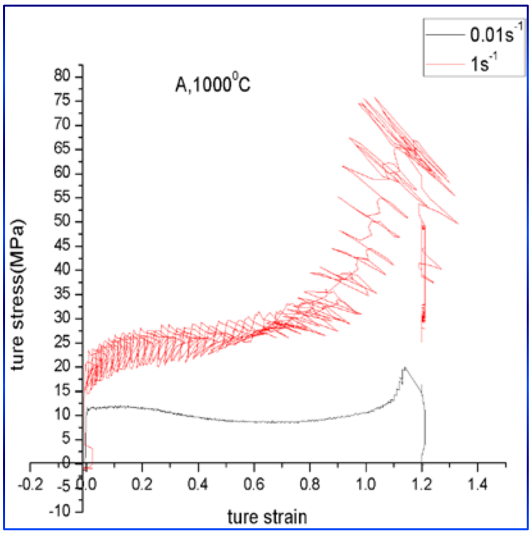

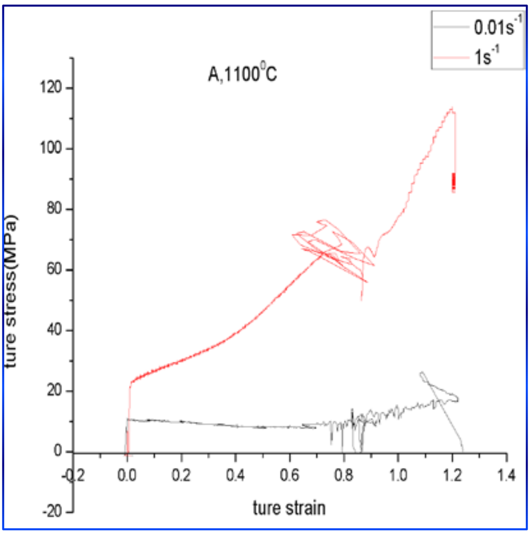

(A, 1000^{o}C) (A, 1100^{o}C)

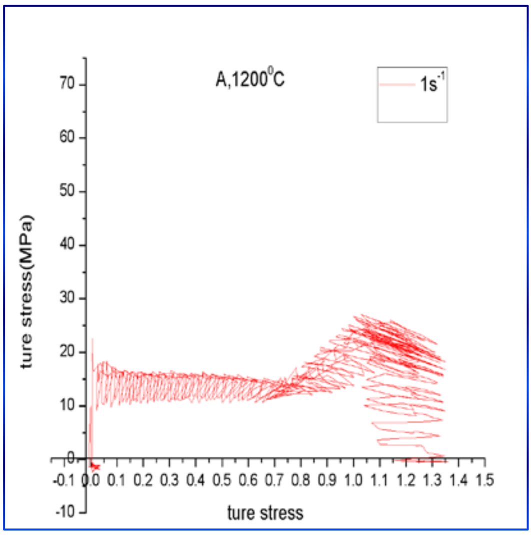

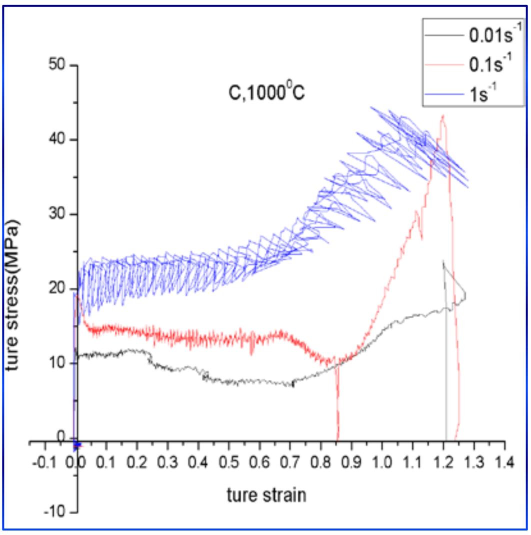

(A, 1200^{o}C) (C, 1000^{o}C)

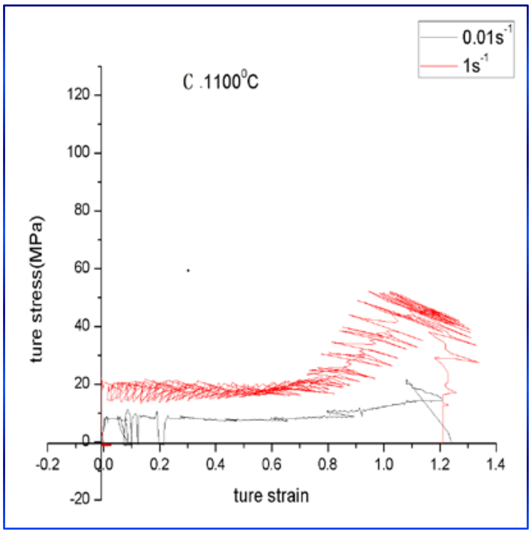

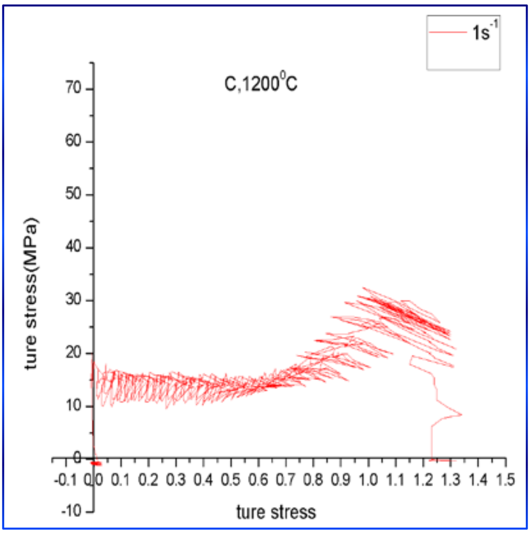

(C, 1100^{o}C)

(C, 1200^{o}C)

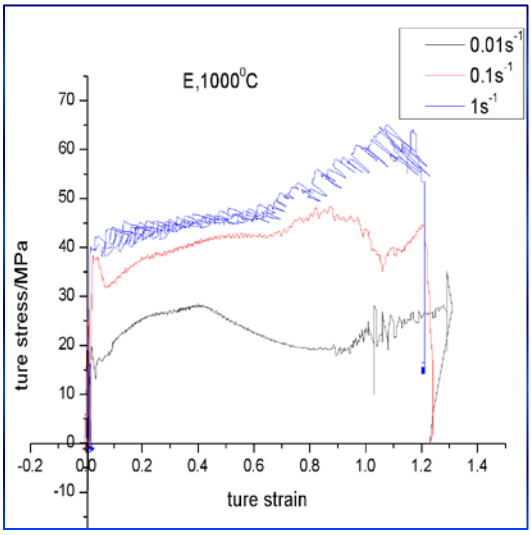

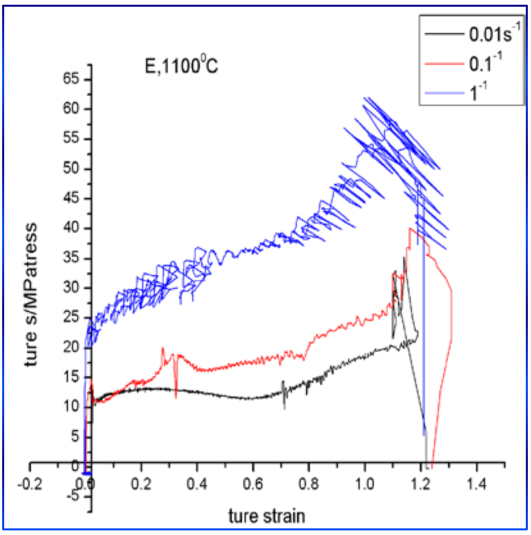

(E, 1000^{o}C)

(E, 1100^{o}C)

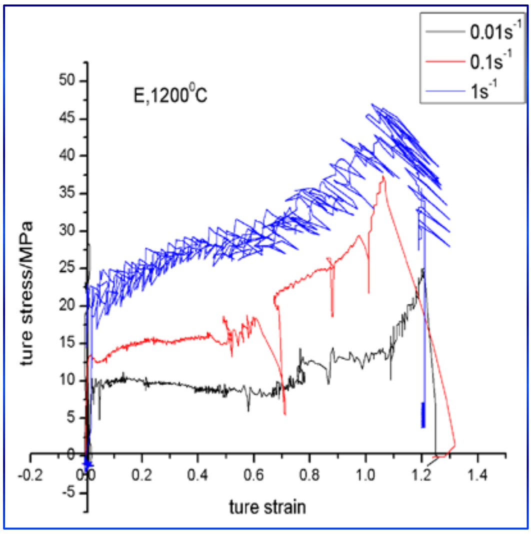

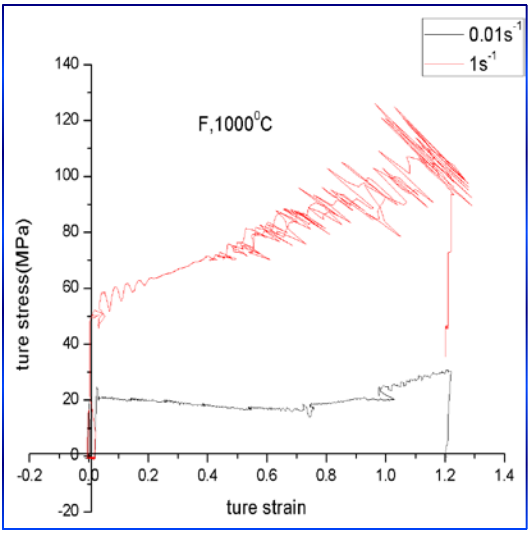

(E, 1200^{o}C)

(F, 1000^{o}C)

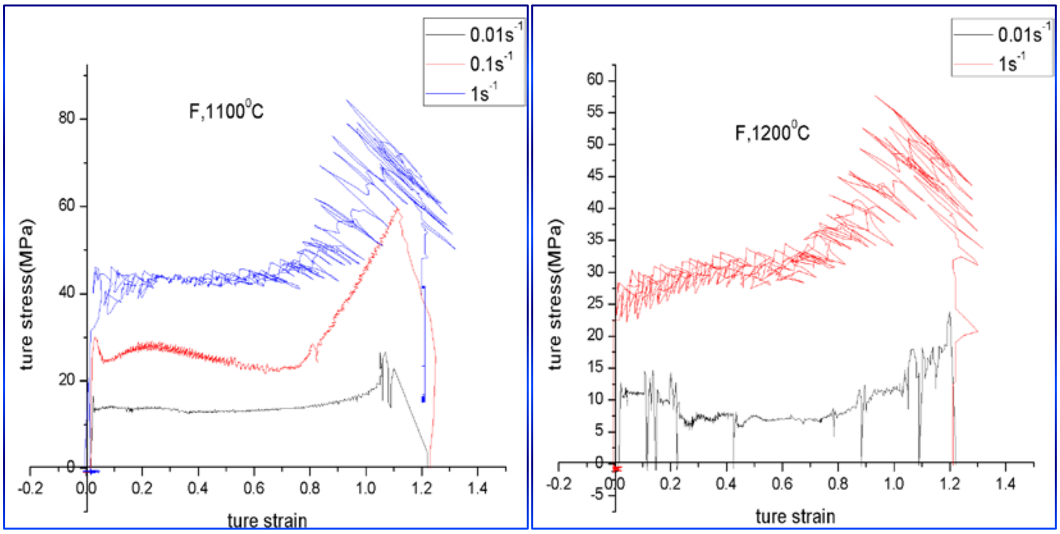

(F, 1100°C) (F, 1200°C)

Figure 5.4: The compressive true stress-true strain curves of all samples which have been tested

All curves in Figure 5.4 have common features. Firstly, the true stress increased with decreasing temperature for the same strain rate. Secondly, the true stress increased with increasing strain rate at the same temperature. Thirdly, the trend of each curve was that it increased or reduced slightly before true strain was 0.8 and then rose rapidly until the true strain was 1.2 as a result of powder consolidation. To sum up, in order to improve the formability of the powder compact, the temperature should be increased appropriately and the strain rate should be reduced. Certainly, the changes of these two factors were related to time and cost. Thus, the purpose of this study was to find out optimum forming conditions for best economy and productivity.

5.4 Simulation

5.4.1 The influence of deformation degree

In metal forging process, gain size can be reduced with the increase of deformation degree, but in P/M process, the occurrence of powder consolidation is accompanying by increasing the the amount of deformation degree .So the amount of deformation of 50% and 70%, respectively, was simulated by FEM. As the result, Mises stress distribution is shown in Figure 5.5 and Figure 5.6. According to the simulation results, the maximum Mises stress occurred in the centre node of the sample, as shown in Figure 5.5 and Figure 5.6, and the minimum Mises stress occurred at the centre of the top and bottom surfaces. The minimum and maximum Mises stresses increased with the amount of deformation. One reasons for these results is work hardening. Another reason is that the sample is a porous material whose density increased with increasing the amount of deformation as the level of powder compact densification increases.

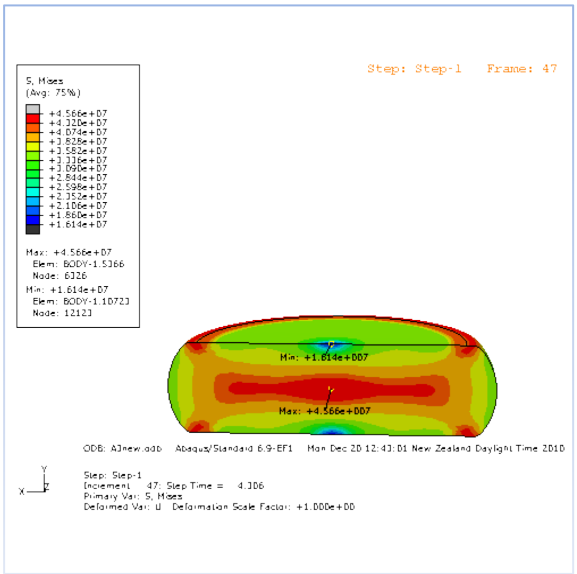

Figure 5.5: Mises stress distribution of the simulation model A

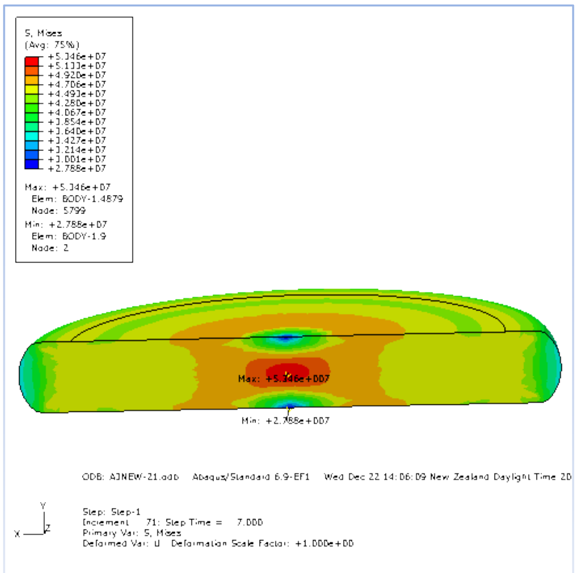

Figure 5.6: Mises stress distribution of the simulation model B

Equivalent plastic strain (PEEQ) distributions of the simulation model A and B are shown in Figure 5.7 and Figure 5.8. The maximum and minimum equivalent plastic strains corresponding to the two amounts of deformation occurred at the corner of the top and bottom planes, as shown in Figures 5.7 and 5.8, unlike the maximum of Mises stress. This can be explained by the constraint of geometry, since there is more freedom of deformation on the surface compared with that at the corner. In contrast, the minimum equivalent plastic strain coincide with the minimum Mises stress.

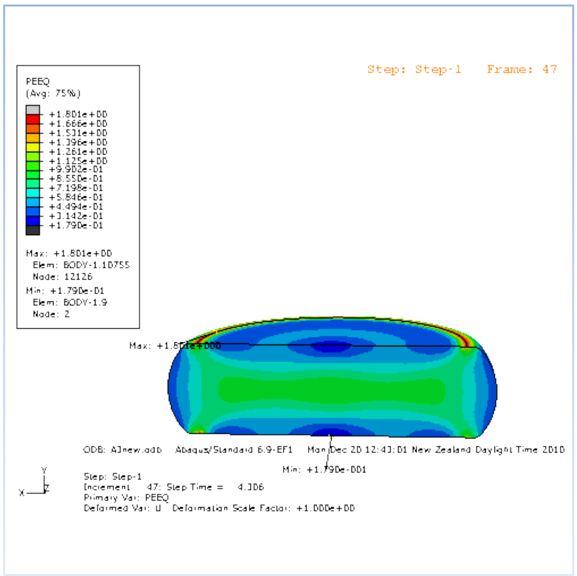

Figure 5.7: Equivalent plastic strain distribution of the simulation model A

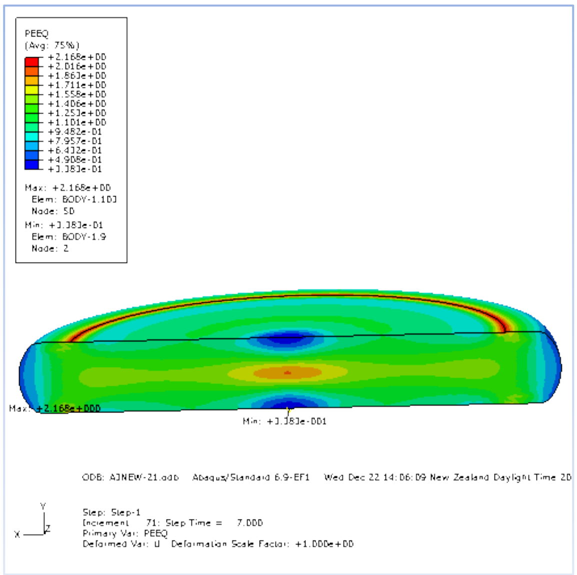

Figure 5.8: Equivalent plastic strain distribution of the simulation model B

The results of strain rate simulation are shown in Figure 5.9 and 5.10. The strain rate distribution became more uniform with increasing the amount of deformation, as shown by comparing Figure 5.10 with Figure 5.9. The change of strain rate in the sample was influenced in the input data of plastic property. As well known, yield stress is sensitive to the strain rate, so the deforming force was different once the change of strain rate occurred.

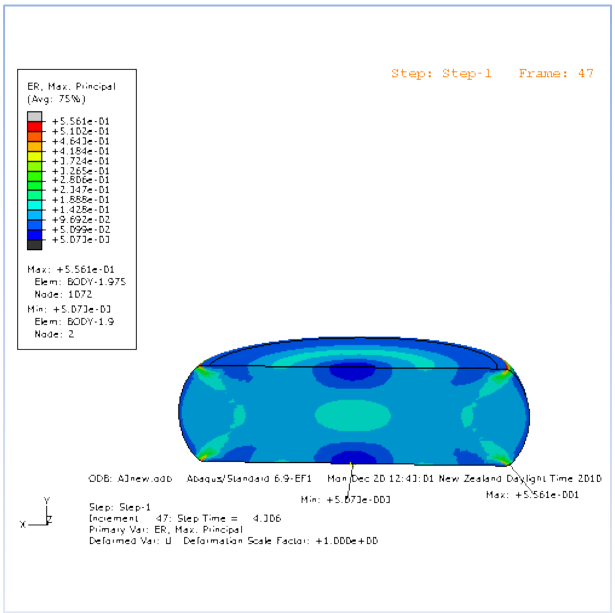

Figure 5.9: Strain rate distribution of the simulation model A

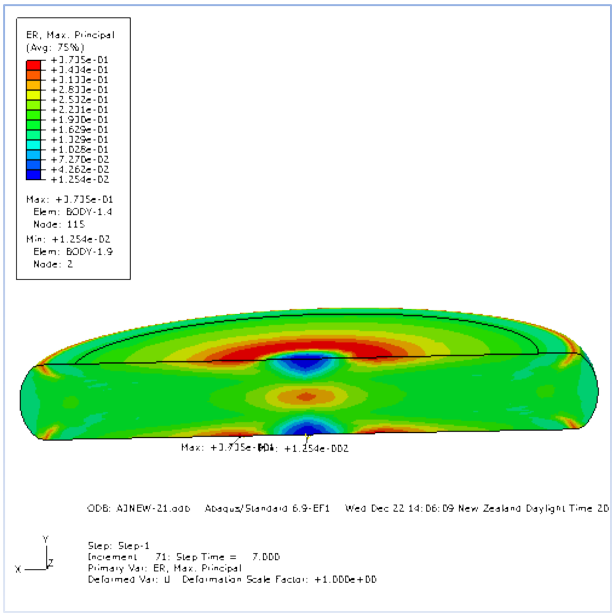

Figure 5.10: Strain rate distribution of the simulation model B

The temperature distribution of the simulation models A and B is shown in Figure 5.11 and Figure 5.12. In this plan, the initial temperatures of dies and powder compact were 500°C and 1050°C respectively, the temperature of atmosphere was 20°C, the heat transfer and heat radiation occurred simultaneously. From these figures, it can be seen that with increasing the amount of deformation and time, the temperature of the sample decreased rapidly. Heat transfer between the dies and powder compact played an important role on the decrease of temperature. Meanwhile the heat radiation from the powder compact to the atmosphere also influenced the temperature change. During deformation, the thermal energy generated from deformation was not enough to make up the thermal energy loss from heat transfer and radiation. This gap became greater with increasing the amount of deformation since the contact areas between the dies and powder compact increased with increasing the amount of deformation, leading to enhanced heat transfer.

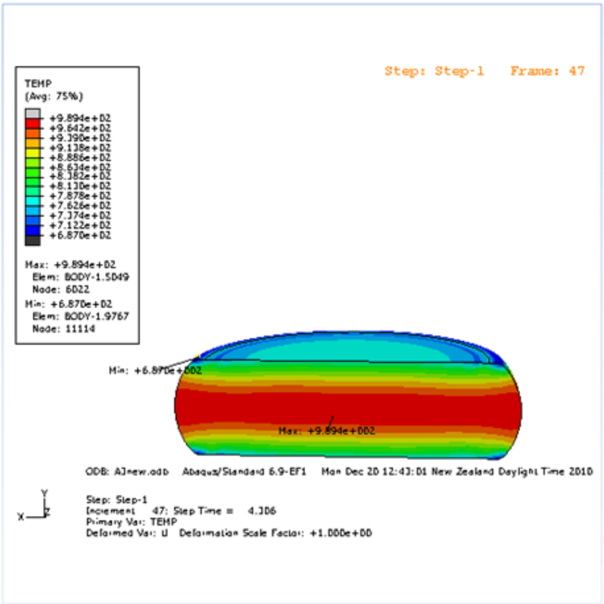

Figure 5.11: Temperature distribution of the simulation model A

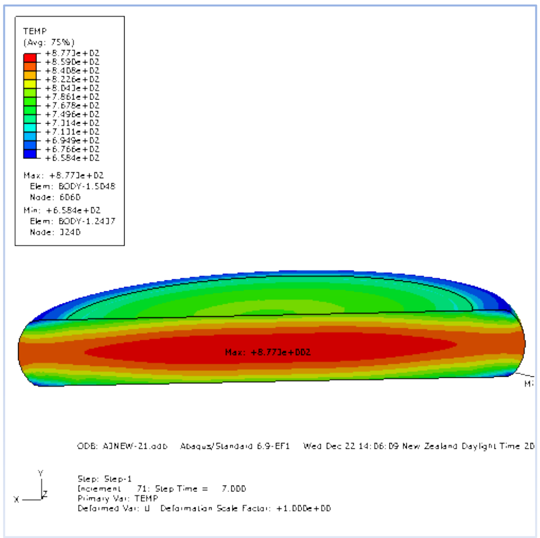

Figure 5.12: Temperature distribution of the simulation model B

The Density distribution of the simulation models A and B is shown in Figure 5.13 and Figure 5.14. The initial relative density was set up to 89% as input data. From these figures, it can be seen that the powder compact consolidation process was fulfilled with increasing the amount of deformation. When the amount of deformation was 50%, the powder compact became fully dense in the middle region of powder compact. With increasing the amount of deformation, the fully dense region expanded gradually. However, the density in the middle part of side face layer was reduced with further deformation. In practice, this part of material needs to be considered as redundant material.

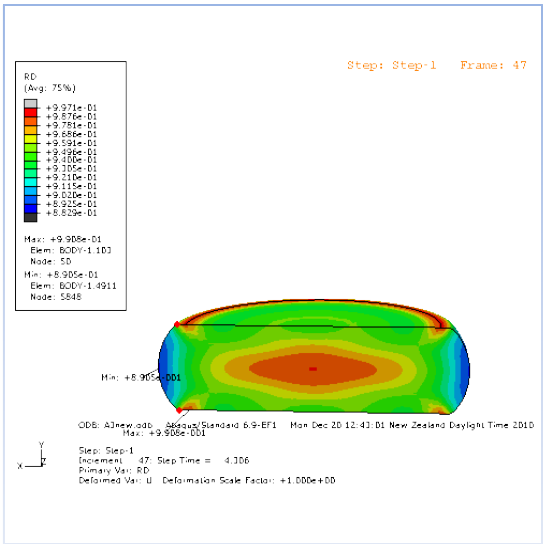

Figure 5.13: Relative density distribution of the simulation model A

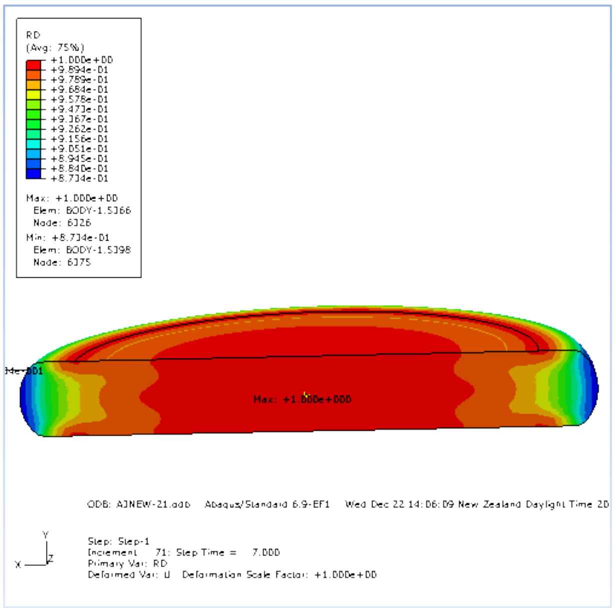

Figure 5.14: Relative density distribution of the simulation model B

5.4.2 The influence of strain rate

In this part, the strain rate was modified as input data and from the results, the effects of strain rate in the powder compact forging were observed. In the models B and C, the total upsetting time was 7s and 2s, respectively, and the compression displacement of the sample was 21mm in total. The calculated average compression velocities were 3mm/s and 10.5mm/s. Thus, the engineering strain rate of the sample was 0.1/s and 0.35/s respectively. Mises stress distribution of the simulation in model C is shown in Figure 5.15. Compared with Figure 5.6, both of the maximum and minimum of Mises stress of the sample increased with strain rate which was attributed to the increase of deformation force when the strain rate increased.

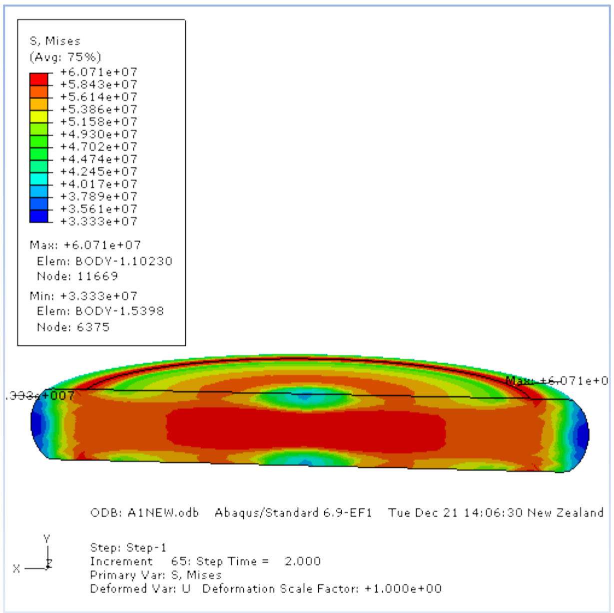

Figure 5.15: Mises stress distribution of the simulation model C

The equivalent plastic strain distribution of the simulation model C is shown in Figure 5.16. From Figure 5.8 and Figure 5.16, it can be seen that the distribution of equivalent plastic strain is similar in both cases, and the geometry of sample was not changed in the two figures.

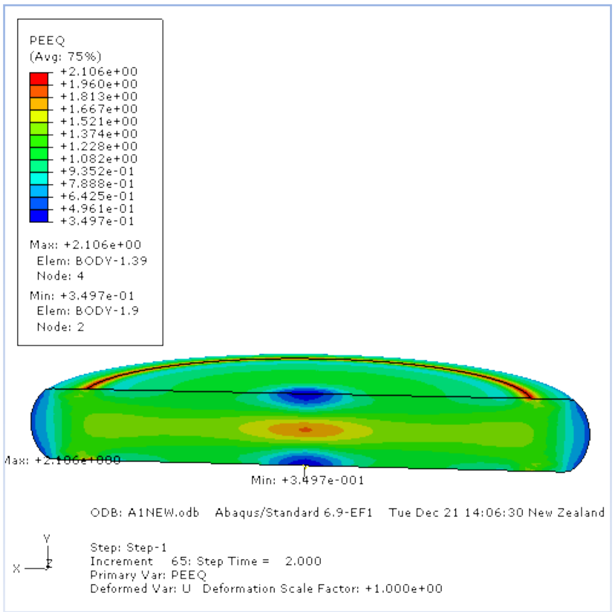

Figure 5.16: Equivalent plastic strain distribution of the simulation model C

The temperature distribution of the simulation model C is shown in Figure5.17. The maximum of the temperatures of the sample was 1023^{o}C, compared with

877°C for that in Model B. This shows that the maximum temperature increased with increasing strain rate. This is because the heat transfer time is reduced with high strain rate, so the loss of heat energy caused by heat conduction and radiation in model C was less than that in model B, and heat generation due to deformation was more intense with increasing strain rate.

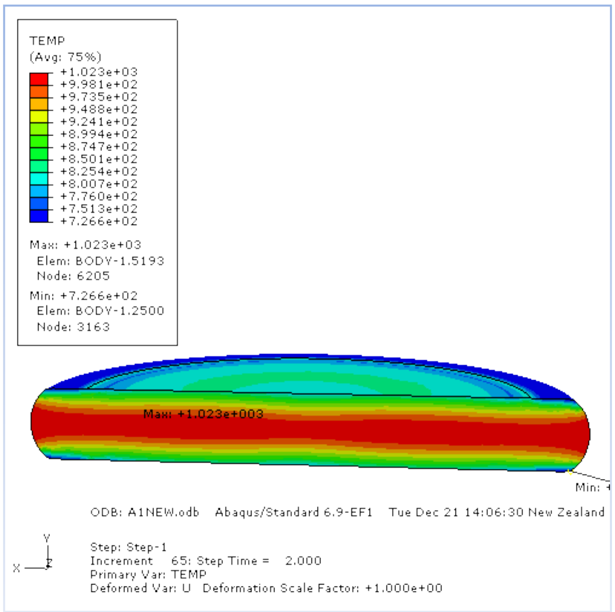

Figure 5.17: Temperature distribution of the simulation model C

The relative density distribution of the simulation model C is shown in Figure 5.18. From Figure 5.14 and Figure 5.18, it can be seen that the relative density distribution was similar in both models, which means that the strain rate had little direct effect on the powder compact consolidation process. In summary, based on the simulation, it can be seen that the strain rate has strong effects on Mises stress and temperature, but little effects on strain distribution and relative density.

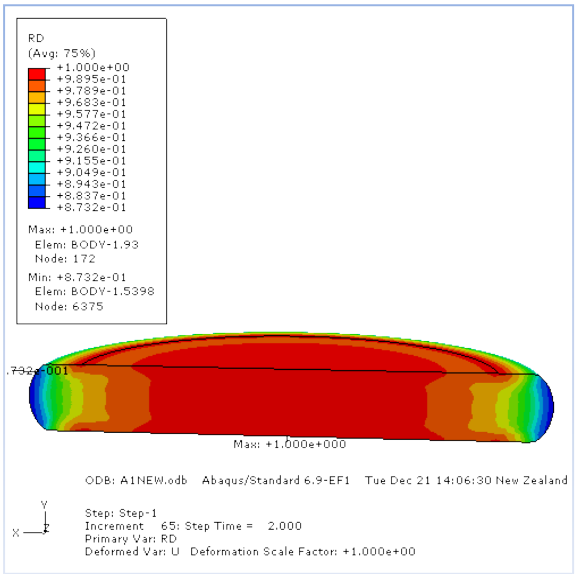

Figure 5.18: Relative density distribution of the simulation model C

5.4.3 The influence of initial sample temperature

The initial sample temperature affects the mechanical properties of the material and deformation force. The Mises stress distribution of the simulation model D is shown in Figure 5.19. By comparing Figures 5.19 and 5.6, it can be seen that the maximum and minimum of Mises stress decreased slightly with increasing initial sample temperature from 1050^{o}C to 1150^{o}C. This can be explained by the lower yield stress with higher initial sample temperature.

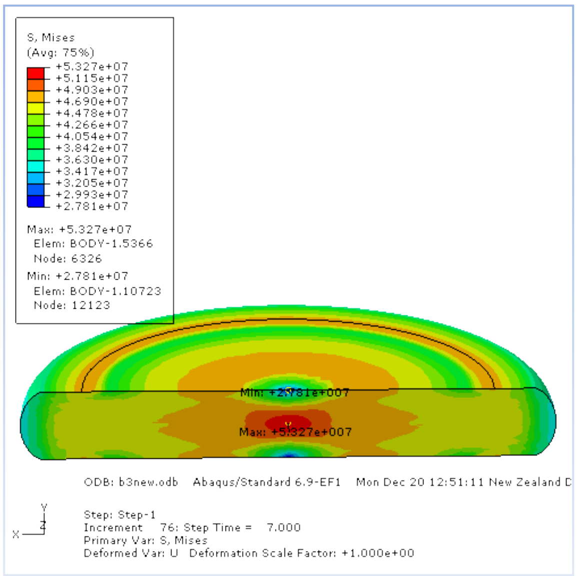

Figure 5.19: Mises stress distribution of the simulation model D

The equivalent plastic strain distribution of the simulation model D is shown in Figure 5.20. By comparing Figures 5.20 and 5.8, we can see that the maximum of the equivalent plastic strain decreased and the minimum of the equivalent plastic strain increased with increasing the initial sample temperature from 1050°C to 1150°C. This means that increasing the initial sample temperature is favourable for getting more uniform distribution of equivalent plastic strain.

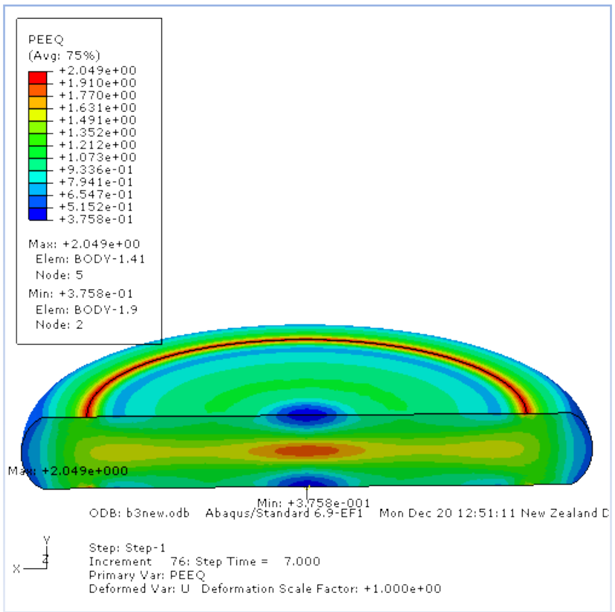

Figure 5.20: Equivalent plastic strain distribution of the simulation model D

The strain rate distribution of the simulation model D is shown in Figure 5.21. By comparing Figures 5.21 and 5.10, it can be seen that with increasing the initial sample temperature the maximal strain rate decreased. This means that increasing the initial sample temperature is favourable for getting more uniform distribution of strain rate. The magnitude of strain rate is not changed with increasing the intial sample temperature.

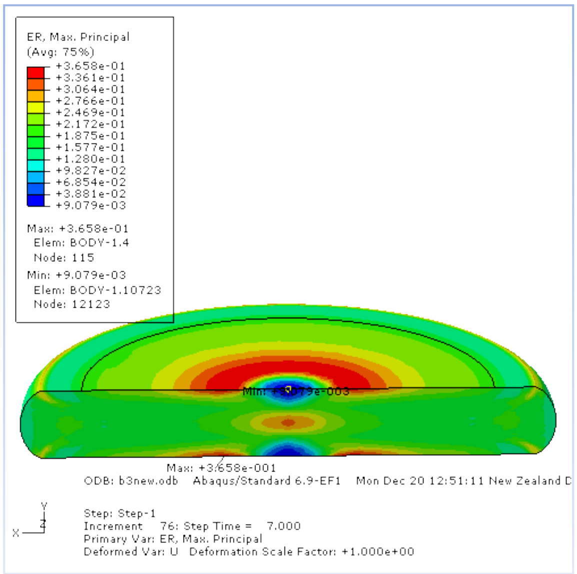

Figure 5.21: Strain rate distribution of the simulation model D

The temperature distribution of the simulation model D is shown in Figure 5.22. Figures 5.22 and 5.12 show that the maximum of the temperatures in the forged disk were 877^{o}C and 941^{o}C, respectively, corresponding to the initial sample temperatures of 1050^{o}C and 1150^{o}C. With these intial sample temperatures, the temperature difference between the maximum and the temperature of the disks corner were 173^{o}C and 209^{o}C respectively. This means that the distribution of temperature was not changed significantly by changing the initial sample temperature from 1050^{o}C to 1150^{o}C, but overall temperature value was increased.

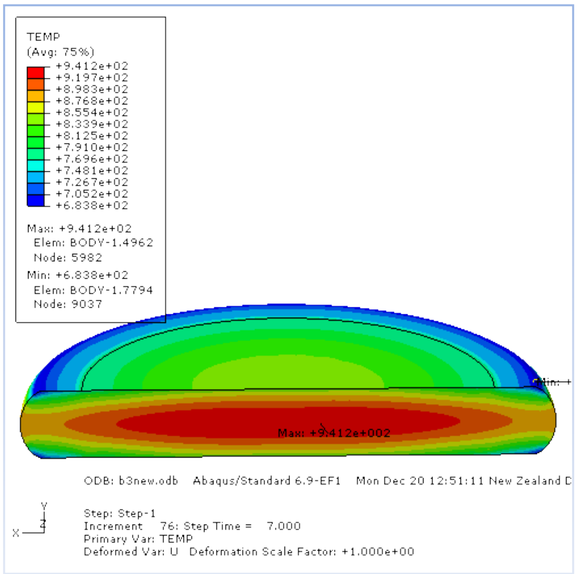

Figure 5.22: Strain rate distribution of the simulation model D

The relative density distribution of the simulation model D is shown in Figure 5.23. By comparing Figures 5.23 and 5.14, it can be seen that the fully dense region was enlarged a little by increasing the initial sample temperature from 1050°C to 1150°C. This can be related to the effect of intial sample temperature on the strain distribution as shown in Figure 5.20.

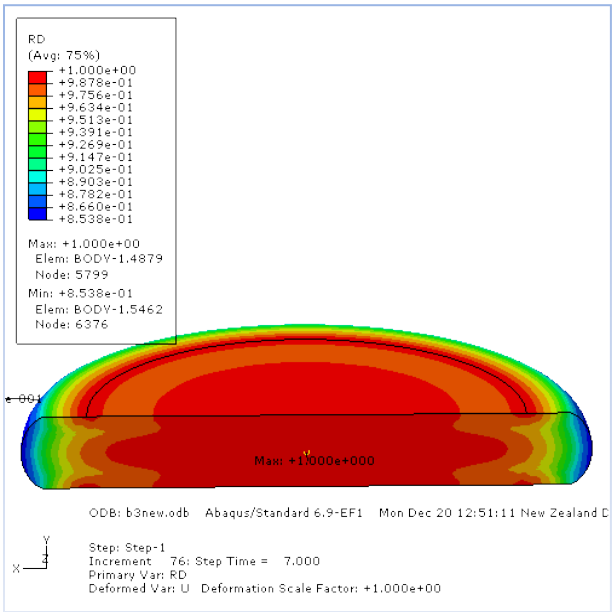

Figure 5.23: Relative density distribution of the simulation model D

5.4.4 The influence of friction coefficient

The friction coefficient influences the energy produced by friction between two surfaces, and the relative movement of two touched parts. Furthermore the shape of the sample after being deformed will be changed with changing friction coefficient. The Mises stress distribution of the simulation model E is shown in Figure 5.24. By comparing Figures 5.24 and 5.6, both of the maximum and the minimum of Mises stress increased with increasing friction coefficient. In addition, the difference between the maximum and the minimum of the Mises stresses increased slightly with increasing the friction coefficient from 0.4 to 0.8. With friction coefficient of 0.8, the maximum of Mises stress was located on the touch surfaces between the die and powder compact, and this is different from that in simulation model B with friction coefficient of 0.4, where the maximum of Mises stress was located at the centre of the sample.

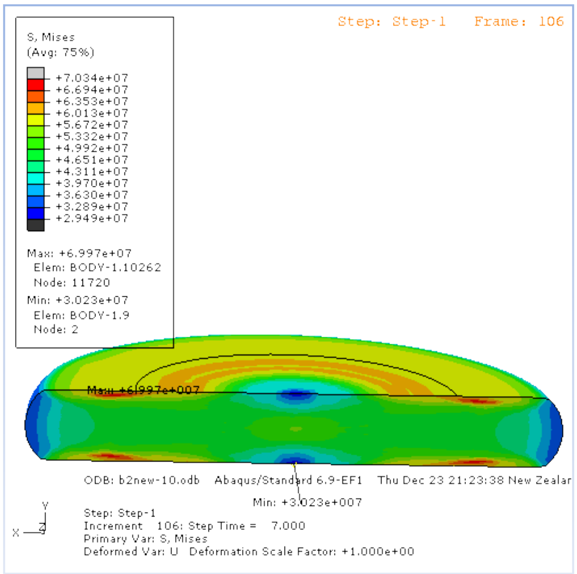

Figure 5.24: Mises stress distribution of the simulation model E

The equivalent plastic strain distribution of the simulation model E is shown in Figure 5.25. From Figures 5.25 and 5.8, it can be seen that the maximum of equivalent plastic strain increased and the minimum of equivalent plastic strain decreased with increasing the friction coefficient. This can be attributed to the constraint from the friction on two surfaces. In order to reduce the friction force, lubricant should be coated on the contact surfaces between the sample and the die.

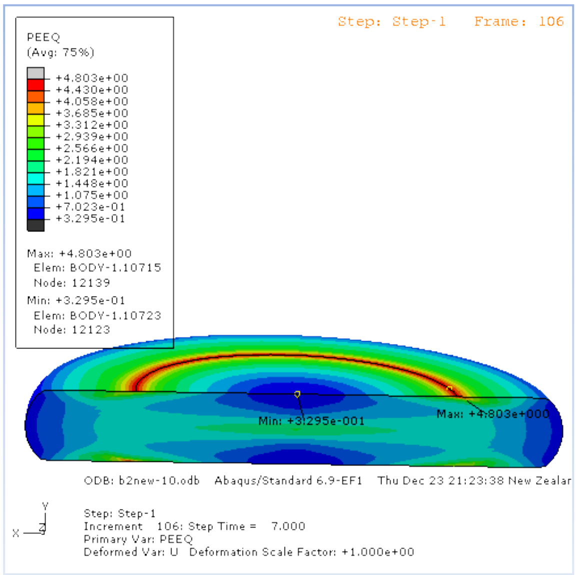

Figure 5.25: Equivalent plastic strain distribution of the simulation model E

The strain rate distribution of the simulation model E is shown in Figure 5.26. By compared Figures 5.26 and 5.10, it can be seen that the maximum of strain rate increased, but the minimum of strain rate changed little with increasing the friction coefficient from 0.4 to 0.8. Both the maximum and the minmum of strain rate appeared near the middle of touch surfaces between the sample and the die.

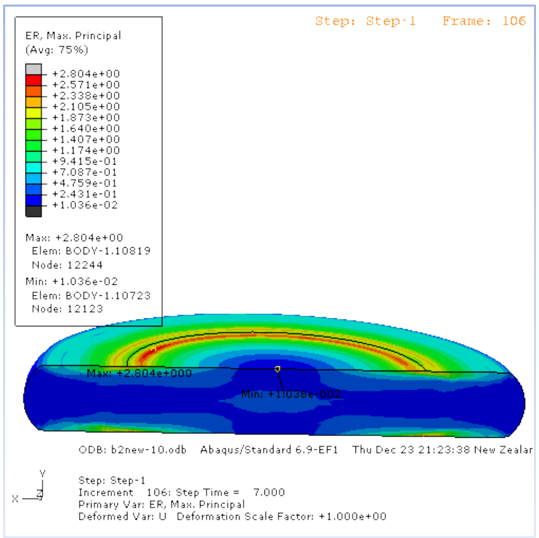

Figure 5.26: Strain rate distribution of the simulation model E

The temperature distribution of the simulation model E is shown in Figure 5.27. From Figures 5.27 and F5.12, both of the maximum and the minimum of temperatures increased with increasing friction coefficient, as a result of the increasing the rate of heat geration from friction.

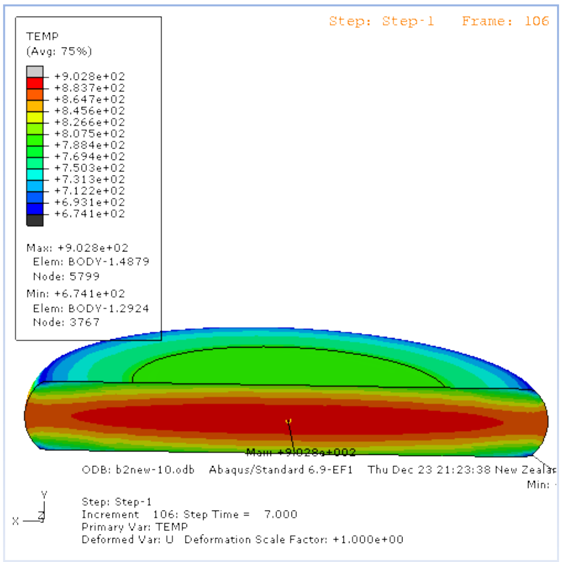

Figure 5.27: Temperature distribution of the simulation model E

The relative density distribution of the simulation model E is shown in Figure 5.28. From Figures 5.28 and 5.14, the volume of the fully dense region was reduced with increasing the friction coefficient, which means that it is beneficial to reduce the friction coefficient for to geting fully dense powder compact.

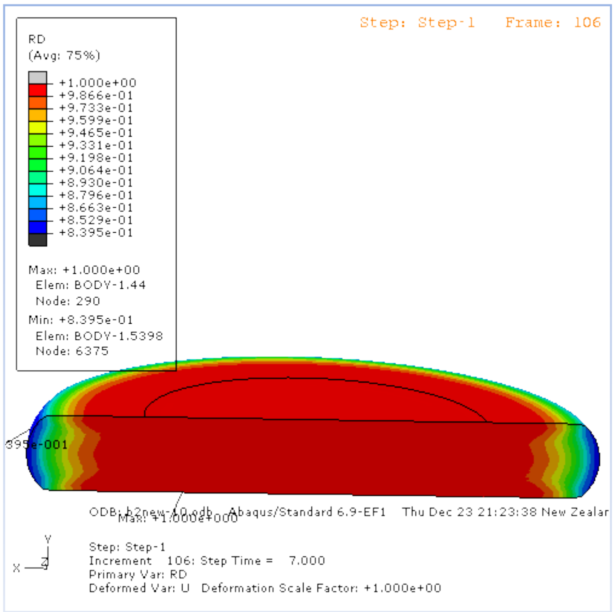

Figure 5.28: Relative density distribution of the simulation model E

5.4.5 The influence of die temperature

Die temperature plays an important role in heat transfer, so it has a great influence on the powder forging. The Mises stress distribution of the simulation model F is shown in Figure 5.29. From Figures 5.22 and 5.6, it can be seen that the difference between the maximum and minimum of Mises stresses was reduced slightly with increasing the die temperature from 50^{o}C to 500^{o}C, and the effect of die temperature on Mises stresses distribution was little.

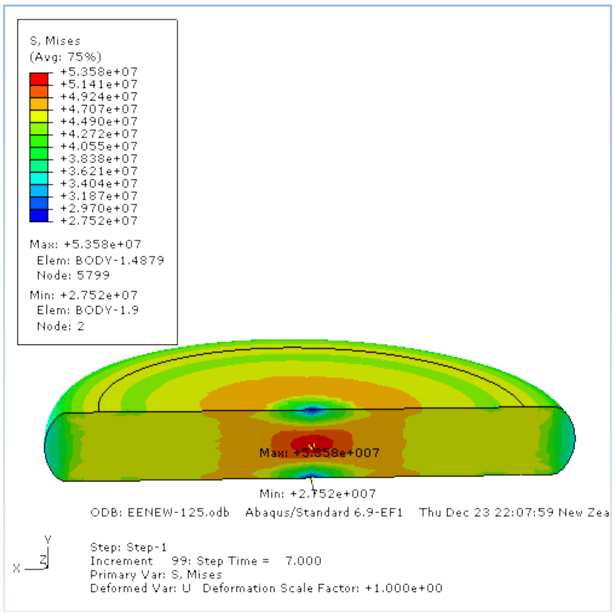

Figure 5.29: Mises stress distribution of the simulation model F

The equivalent plastic strain distribution of the simulation model F is shown in Figure 5.30. From Figures 5.30 and 5.8, both of the maximum and minimum of equivalent plastic strain were reduced slightly with increasing die temperature from 50°C to 500°C, and this change of die temperature had little effect on the equivalent plastic strain distribution.

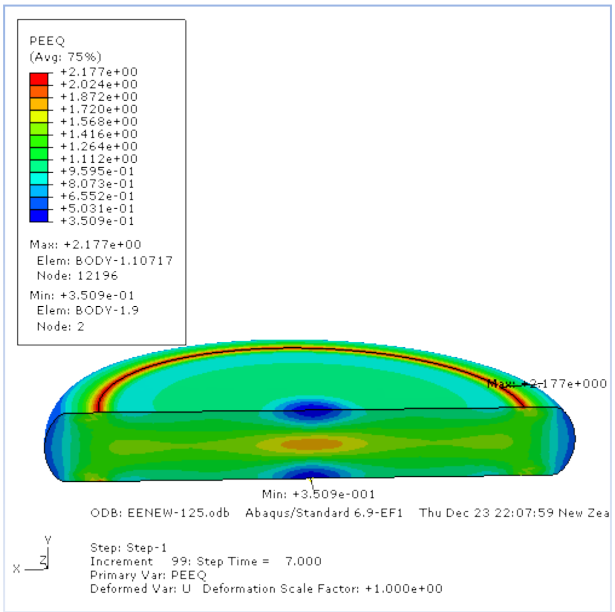

Figure 5.30: Equivalent plastic strain distribution of the simulation model F

The strain rate distribution of the simulation model F is shown in Figure 5.31. By comparing Figures 5.31 and 5.10, both of the maximum and minimum of strain rate changed little with increasing the die temperature from 50^{o}C to 500^{o}C.

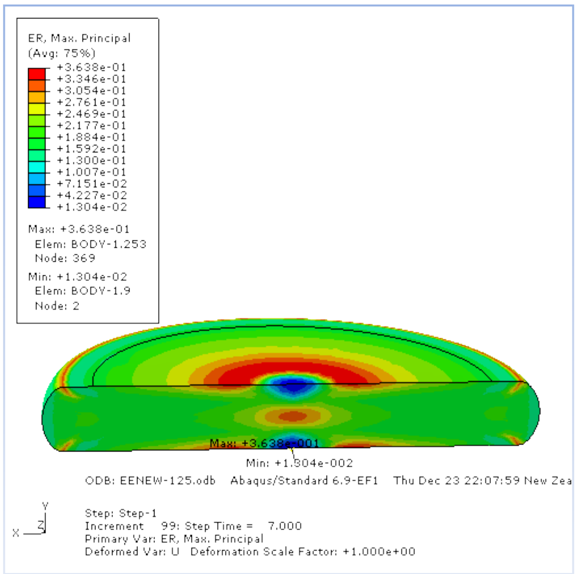

Figure 5.31: Strain rate distribution of the simulation model F

The temperature distribution of the simulation model F is shown in Figure 5.33. From Figures 5.32 and 5.12, the maximum of the temperature increased by 120^{o}C, while the minimum of temperature increased by 286^{o}C when the die temperature increased from 50^{o}C to 500^{o}C. Accordingly, increasing the initial die temperature is beneficial for getting more uniform distribution of temperature in the sample.

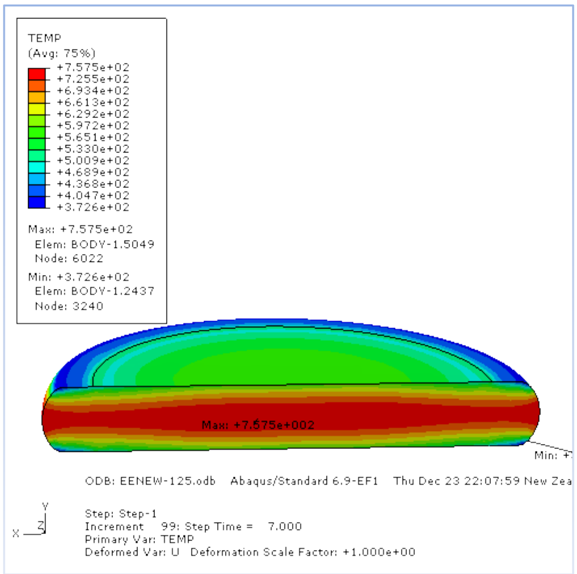

Figure 5.32: Temperature distribution of the simulation model F

The relative density distribution of the simulation model F is shown in Figure 5.33. In Figures 5.33 and 5.14, there was the same density distribution with different die temperature, so the die temperature had little effect on densification.

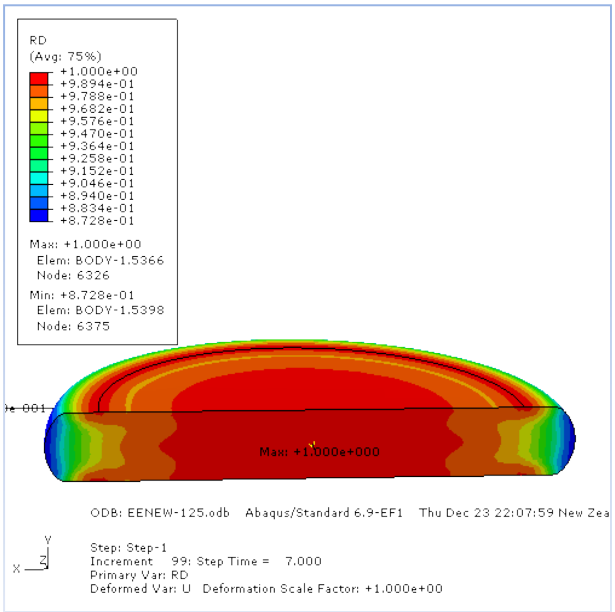

Figure 5.33: Relative density distribution of the simulation model F

5.4.6 The influence of material

Different materials have different properties. In this part, the initial properties were changed to determine their effects. The Mises stress distributions of the simulation model G, H and I is shown in Figures 5.34, 5.35 and 5.36, the maximum of Mises stress is 36.7MPa and 42.3MPa, respectively. Both of the materials in Model G and H were titanium with different sintered holding time. Both samples of the Model G and H were heated to 1200°C for sintering. The sample in Model G had no holding time, which holding time in model H had 5 minutes. Accordingly, it is favourable to enhance stress by increasing sintered holding time. On the other hand, in the simualtion models B and I, the maximum of stress were 53.4MPa and 69.3MPa respectively. Both the material in model B and I were Ti-6Al-4V with different sintered temperature. The sintered temperature of model B was 120°C, which was higher than 1300°C in model I which depended on the initial density and properties after sintering.

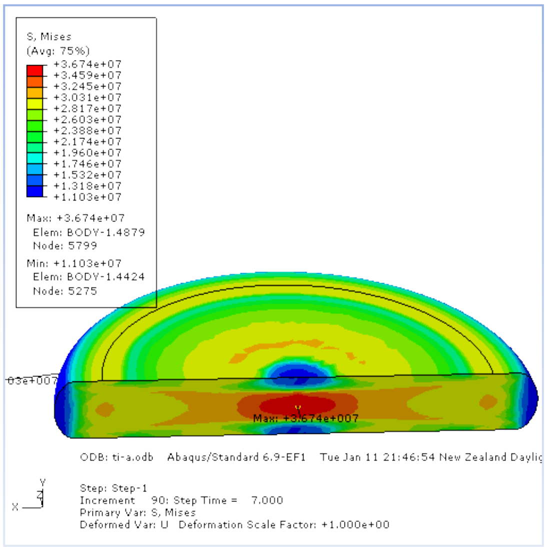

Figure 5.34: Mises stress distribution of the simulation model G

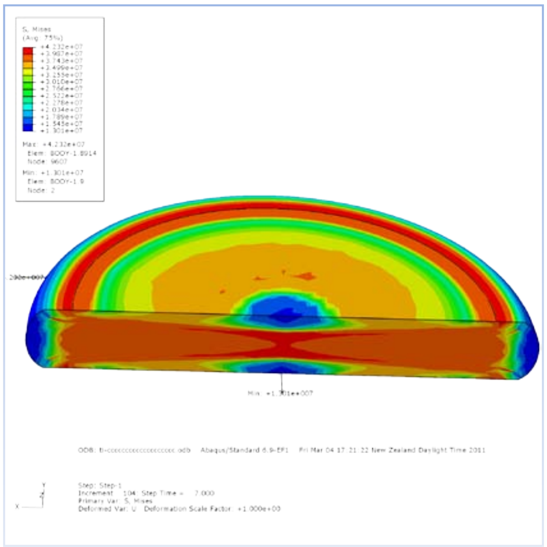

Figure 5.35: Mises stress distribution of the simulation model H

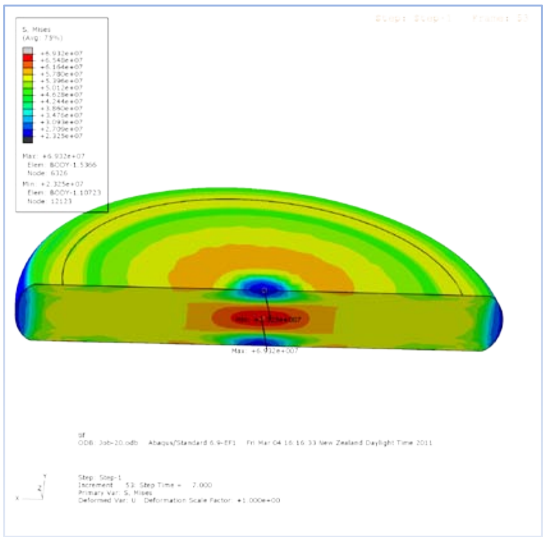

Figure 5.36: Mises stress distribution of the simulation model I

The equivalent plastic strain distributions in simulation models G, H and I are shown in Figures 5.37, 5.38 and 5.39. From Figures 5.37, 5.38, 5.10 and 5.39, it can be seen that the distributions of equivalent plastic strain were similar in all cases. Accordingly, materials had very little effect on the distribution of equivalent plastic strain.

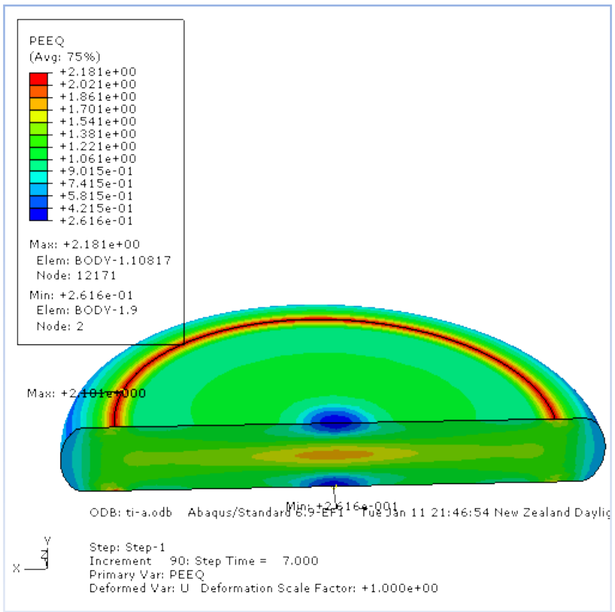

Figure 5.37: Equivalent plastic strain distribution of the simulation model G

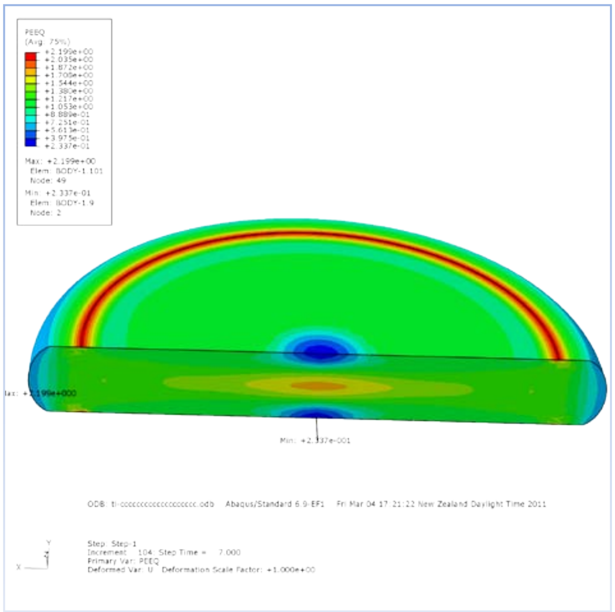

Figure 5.38: Equivalent plastic strain distribution of the simulation model H

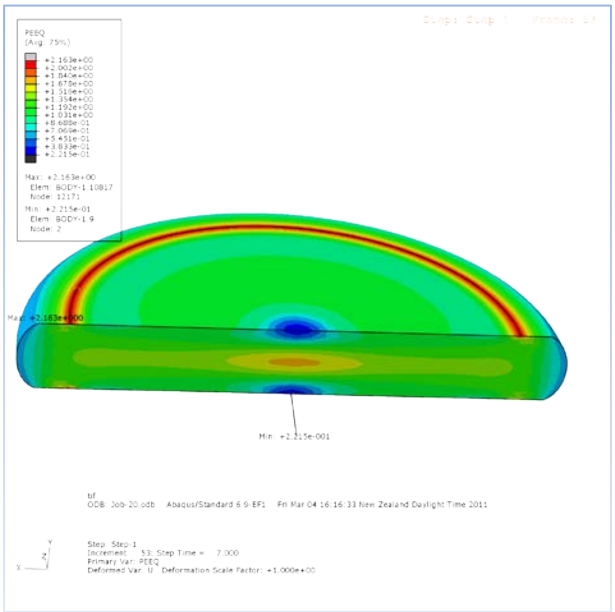

Figure 5.39: Equivalent plastic strain distribution of the simulation model I

The temperature distribution of the simulation model G, H and I is shown in Figures 5.40, 5.41 and 5.42 respectively. From these figures and Figure 5.14, it can be seen that the temperature distribution is similar in simulation models G, H B and I respectively. Accordingly, the difference of temperature distribution is mainly attributed to the differenece in thermal conductivity between titanium and Ti-6Al-4V.

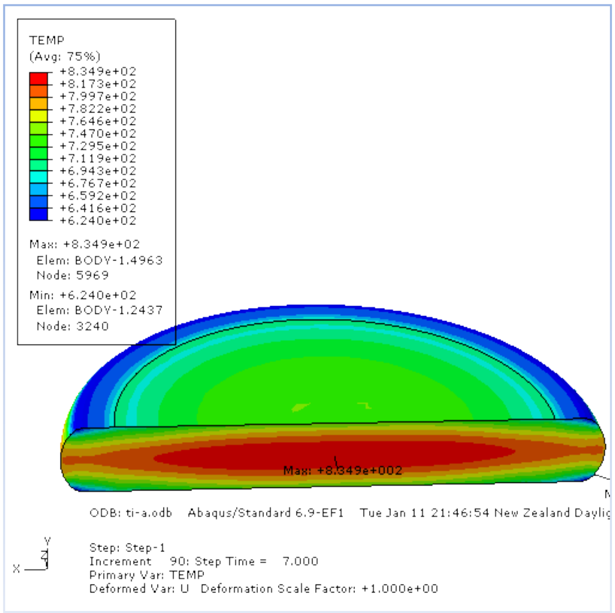

Figure 5.40: Temperature distribution of the simulation model G

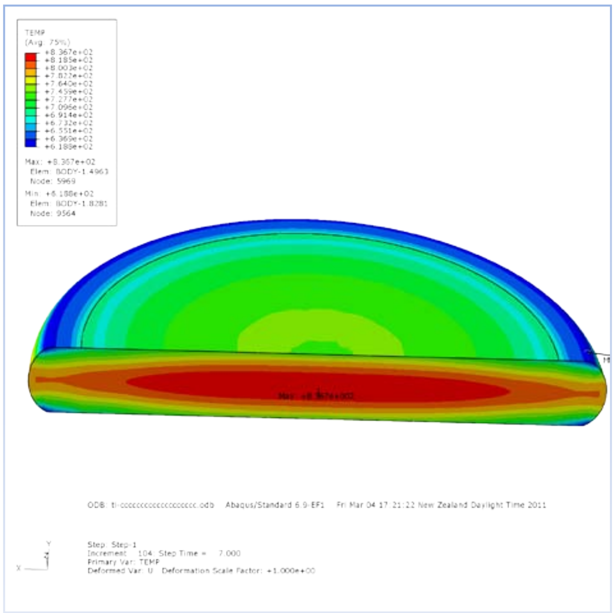

Figure 5.41: Temperature distribution of the simulation model H

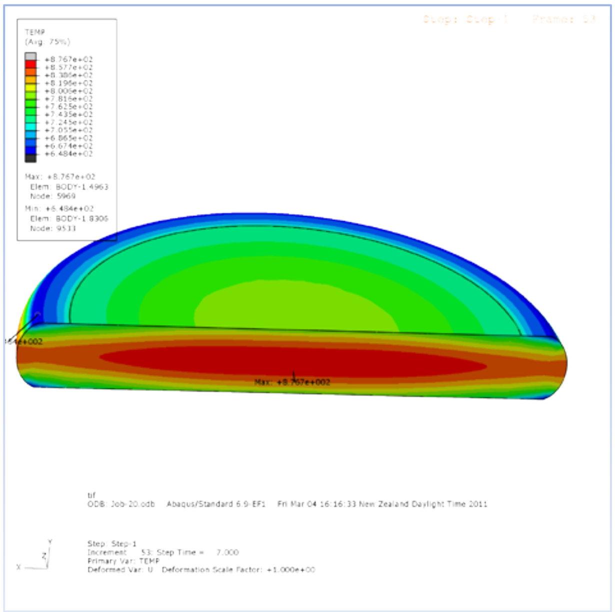

Figure 5.42: Temperature distribution of the simulation model I

The relative density distribution of the simulation model G, H and I is shown in Figure 5.43, 5.44 and 5.45. From these figures and Figure 5.14, it can be seen that the relative density distribution is similar for all materials.

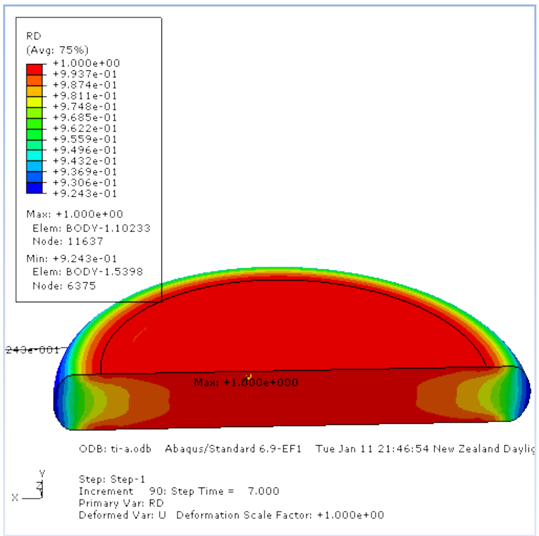

Figure 5.43: Densification distribution of the simulation model I

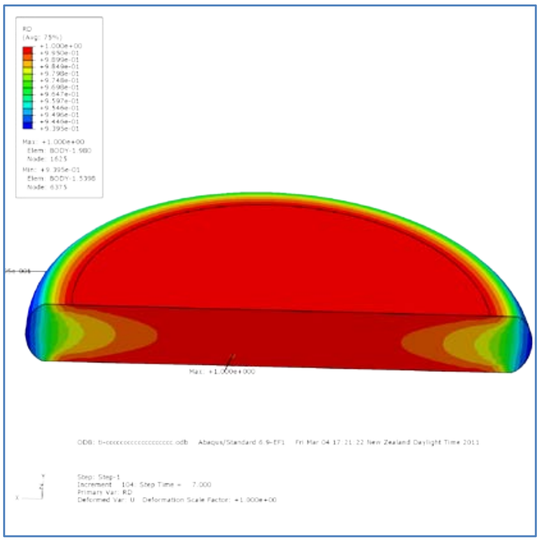

Figure 5.44: Densification distribution of the simulation model I

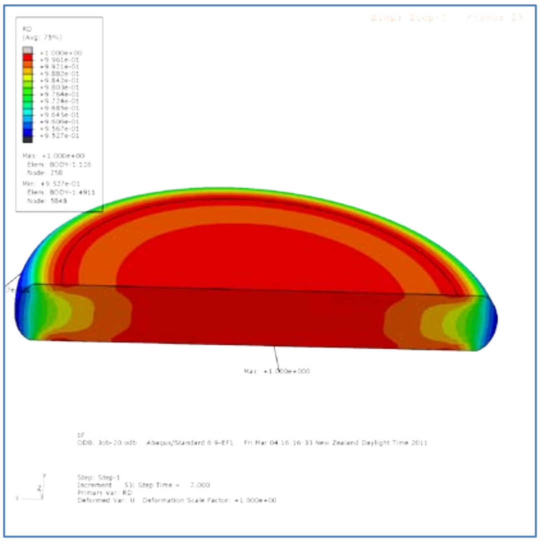

Figure 5.45: Relative density distribution of the simulation model H

5.4.7 Tracking points

In order to make tracks for output data of forging process, nine typical tracking points in model B were selected at positions as shown in Figure 5.46. By using the postprocessing of ABAQUS, the tracking curves were gained as shown in Figures 5.47, 5.58 and 5.59. In Figure 5.47, the heat loss on the end-surface (A1, A2 and A3) was much more than that on the middle-plane (C1, C2 and C3). In addition, the temperature of A1, A2 and A3 decreased rapidly at the beginning and then changed slowly, while the temperature of C1, C2 and C3 increased a little and then decreased slightly. Meanwhile, the temperatures of side-surface (A3, B3 and C3) were a little higher than inside (A1, A2, B1, B2, C1 and C2). The increase and decrease of the temperature were ascribed to heat transfer, heat radiation and heat energy origination from deformation. In the initial stage, the sample contacted the cool dies then the temperature of contact surfaces of sample dropped rapidly, but the temperature in the centre was not changed a lot, because of the longer heat transfer path. In addition the heat increase from deformation was more than heat loss from transfer in the initial stage for C1, C2 and C3 points, thus, the temperatures increased a little. Furthermore, heat transfer from the billet to air was smaller than from the billet to the dies.

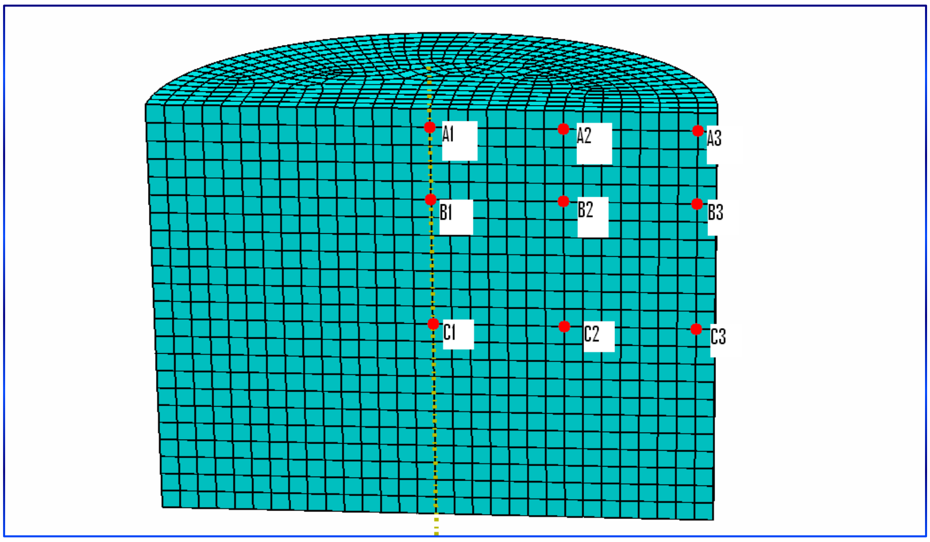

Figure 5.46: The sketch map of the tracking points

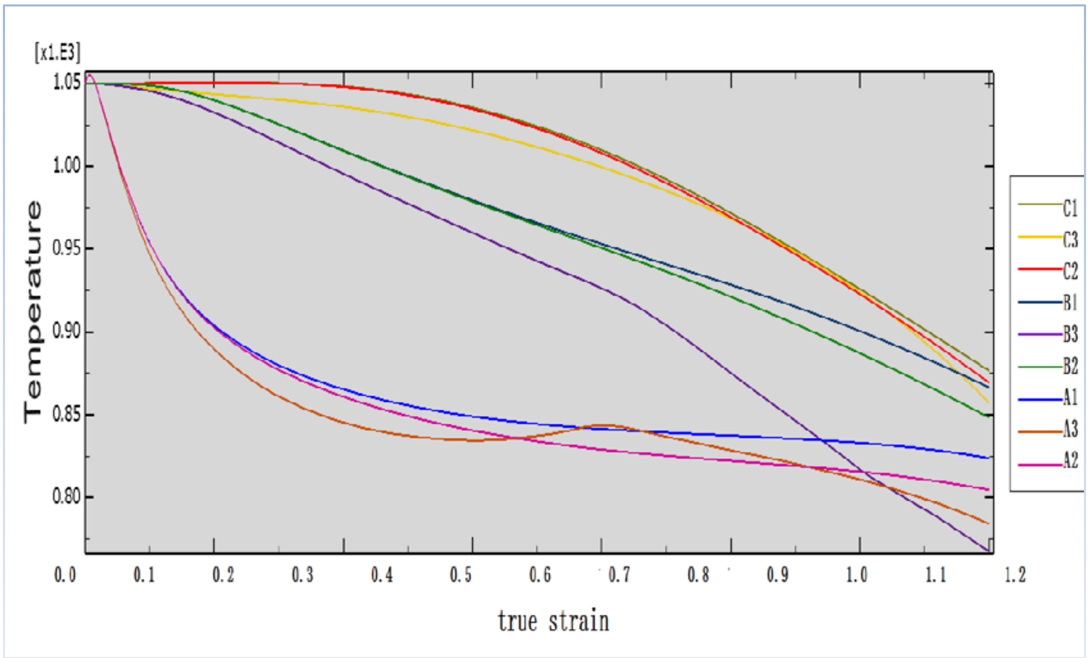

Figure 5.47: The curves of temperatures of some points with true strain of billet

From Figure 5.48, it can be seen that the stresses at B1, B2, C1 and C2 were obviously higher than those at A1 and C3. In the upsetting, the strain in the middle of end-surfaces (A1) was the smallest among the nine tracking points, which were related the friction from the contacts, which hindered further deformation. Thus, its stress and strain were the smallest.

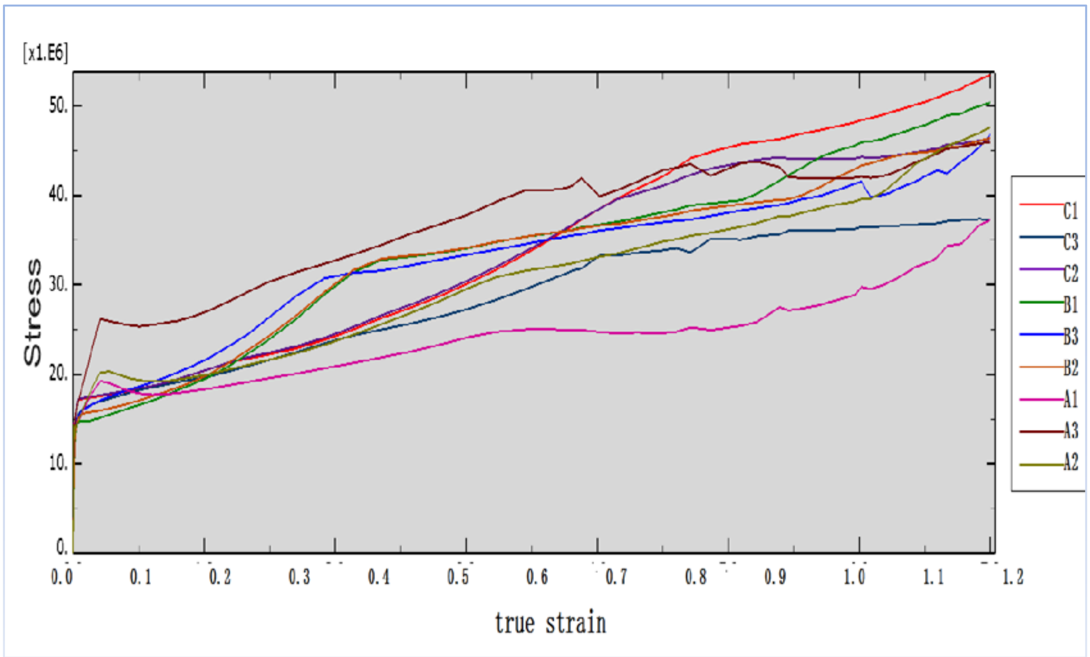

Figure 5.48: The curves of Mises stres of some points with true strain of billet

From Figure 5.49, it can be seen that except points B3 and C3, all of the curves climbed from 89% to 100%, so that the full density was achieved with increasing the true strain of the sample. However, due to the friction, the density in middle of side-surface (B3 and C3) increased slowly, furthermore the curve of C3 decreased in later stage.

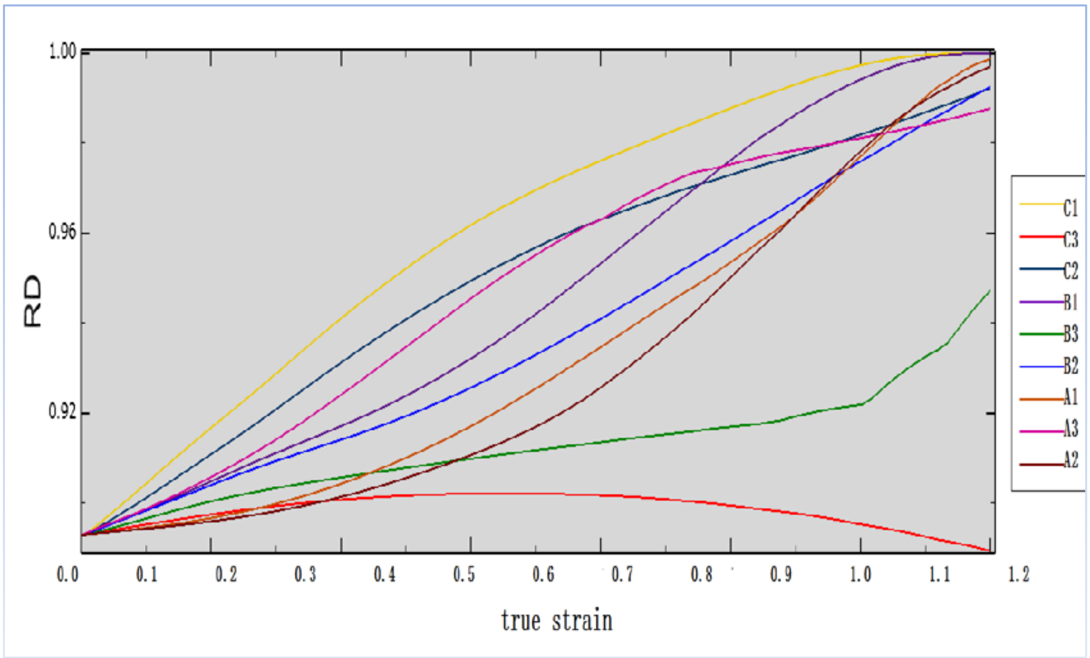

Figure 5.49: The curves of relative density of some points with true strain of billet

5.4.8 The curves of displacement and load

The curve of displacement and load shows the change of load in material plastic deformation. This value can be considered to be useful for equipment and forming process selection. The curves of displacement and load of model B, C, D, E, G, H and I are shown in Figure 5.50. From Figure 5.50(a), the deformation force increased with reducing the strain rate as a result, the velocity of the sample softening was bigger than that of hardening. The strain rate reduced with increasing the upsetting time and reducing temperature of billet when the billet became softer.

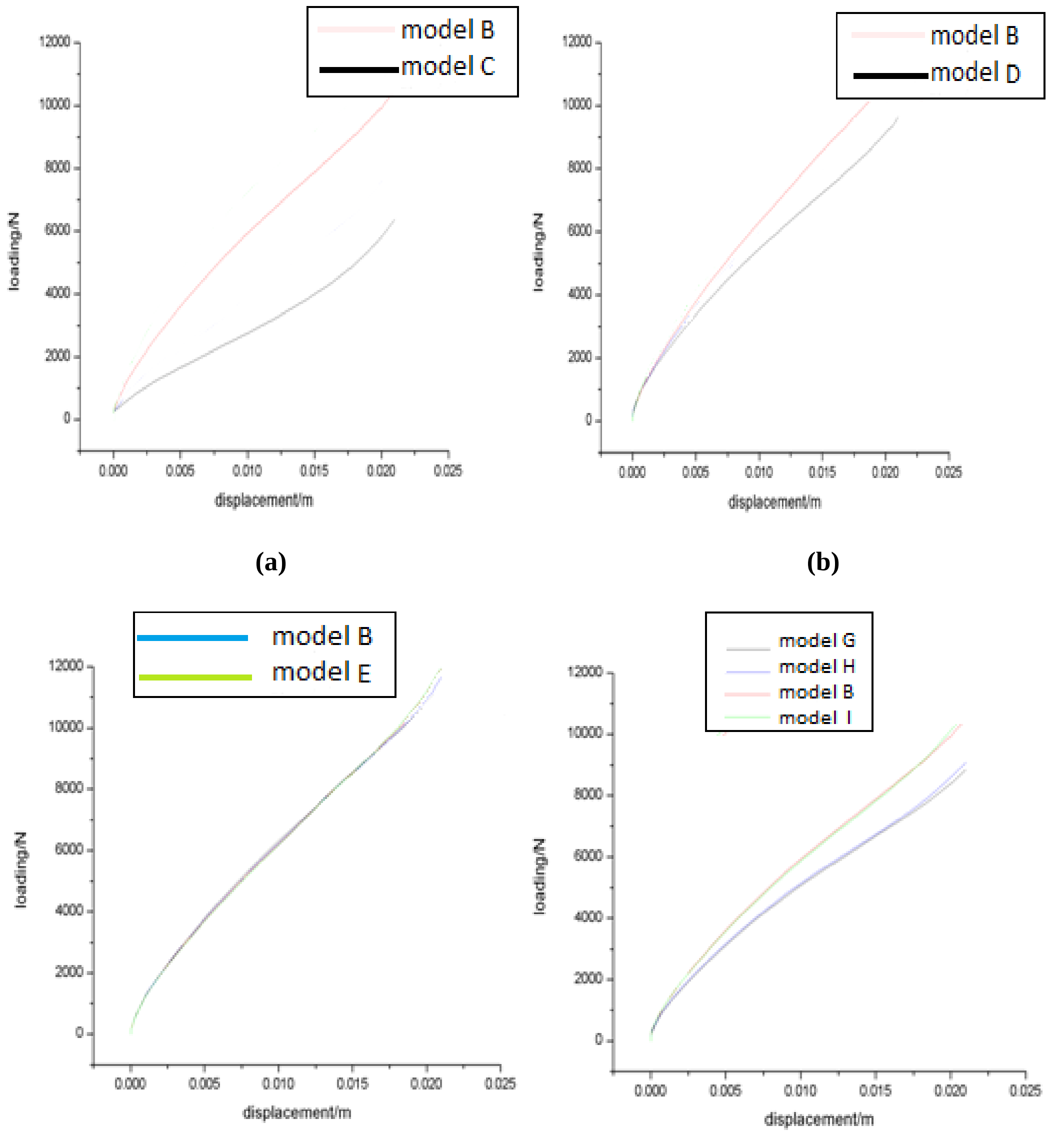

(a) (b)

(c) (d)

Figure 5.50: The curves of displacement with loading with different conditions: (a)strain rate, (b)initial sample temperature, (c) friction coefficient, (d)material

From Figure 5.50(b), it can be seen that the deformation force decreased with increasing the initial temperature, as a result, with increasing the temperature, the kinetic energy of metal atom increased, the dislocation increased, plastic stress decreased. In Figure 5.50(c), there was no obvious effect for deformation force with increasing friction coefficient. In Figure 5.50 (d), the deformation force of Ti-6Al-4V was bigger than that of titanium. But, there was no obvious effect distinction for model G,H,B and I.

5.5 Optical microscopy examination of forged samples

As shown by the results of simulation, increasing the initial powder compact temperature and reducing the strain rate are very beneficial to powder consolidation. In order to prove the reliability of the simulation, the microstructure of the compression samples were observed by using an optical microscope. Firstly, two points on the cross section of the samples, as shown in Figure 5.51 were chosen to be observed. Secondly, two magnifications were selected: one is ×50 and one is ×200. Thirdly, four compressed samples were chosen to observe the density distribution after forging , namely, Ti-6Al-4V(GA, group A, 1000^{o}C, 1/s), Ti-6Al-4V(GA, group A, 1100 ^{o}C, 0.01/s), titanium (HDH, group E, 1000 ^{o}C, 1/s) and titanium (HDH, group E,1200 ^{o}C, 0.01/s). Their microstructures are shown in Figures 5.52, 5.53, 5.54 and 5.55.

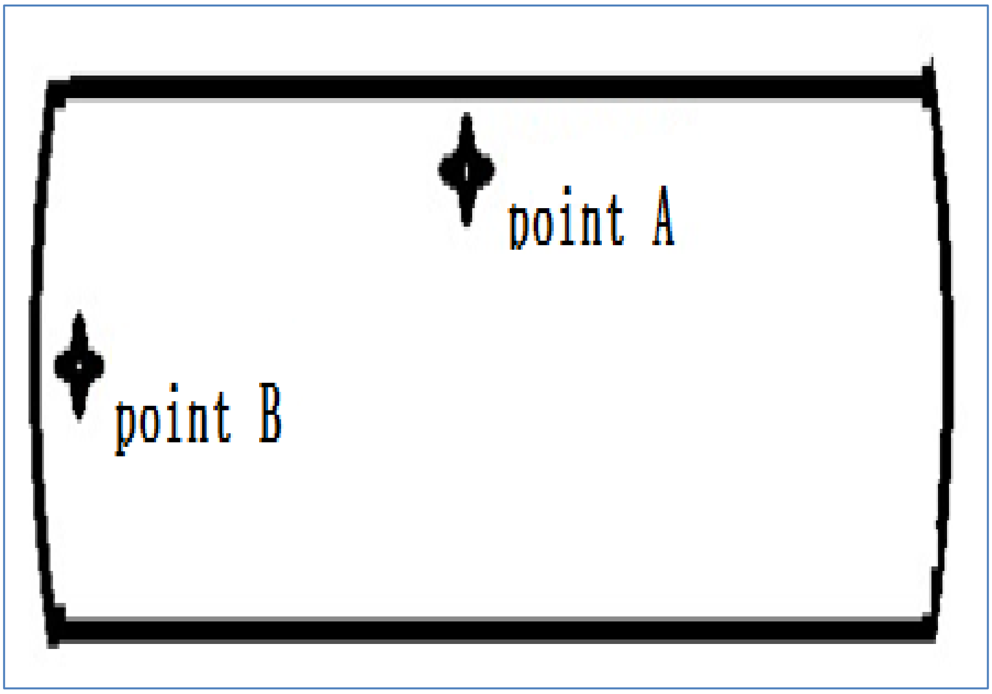

Figure 5.51: A sketch map of sampling

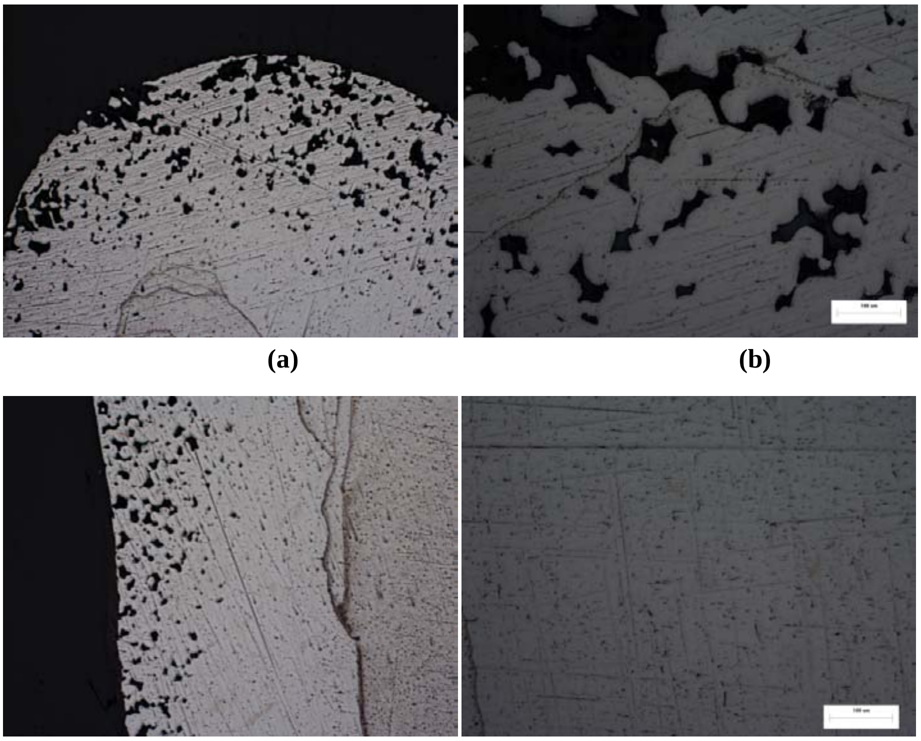

(a) (b)

(c) (d)

Figure 5.52: The microstructure of the compression samples of Ti-6Al-4V, (1000oC, 1/s): (a) point B, ×50, (b) point B, ×200, (c) point A, ×50, (d) point A, ×200

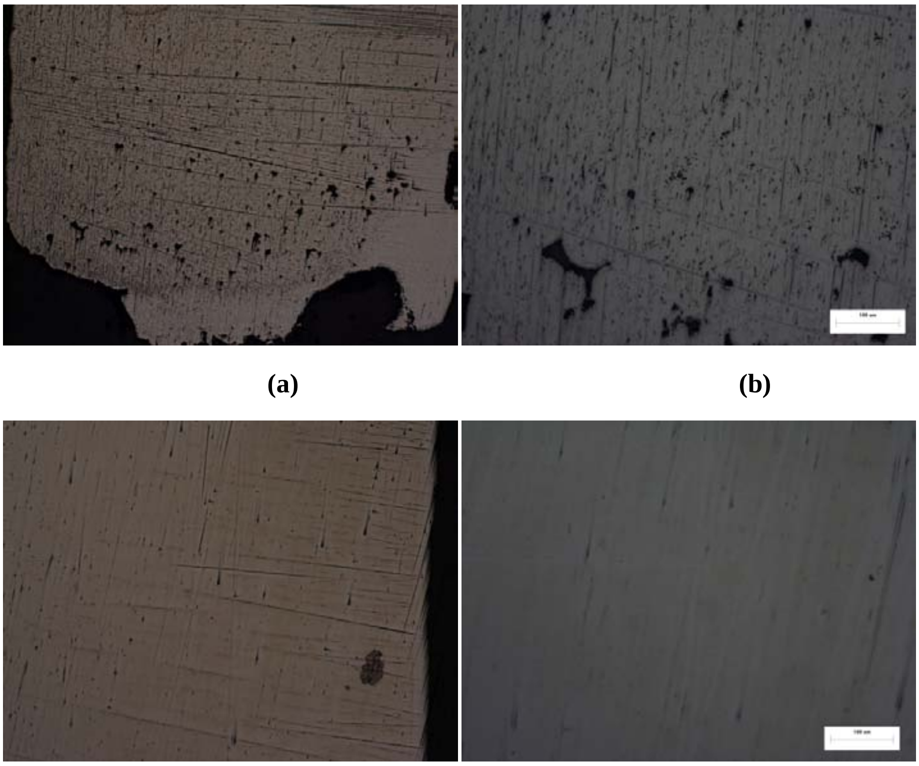

(a) (b)

(c) (d)

Figure 5.53: The microstructure of the compression samples of Ti-6Al-4V, 1100 ^{o}C, 0.01/s: (a) point B, ×50, (b) point B, ×200, (c) point A, ×50, (d) point A, ×200

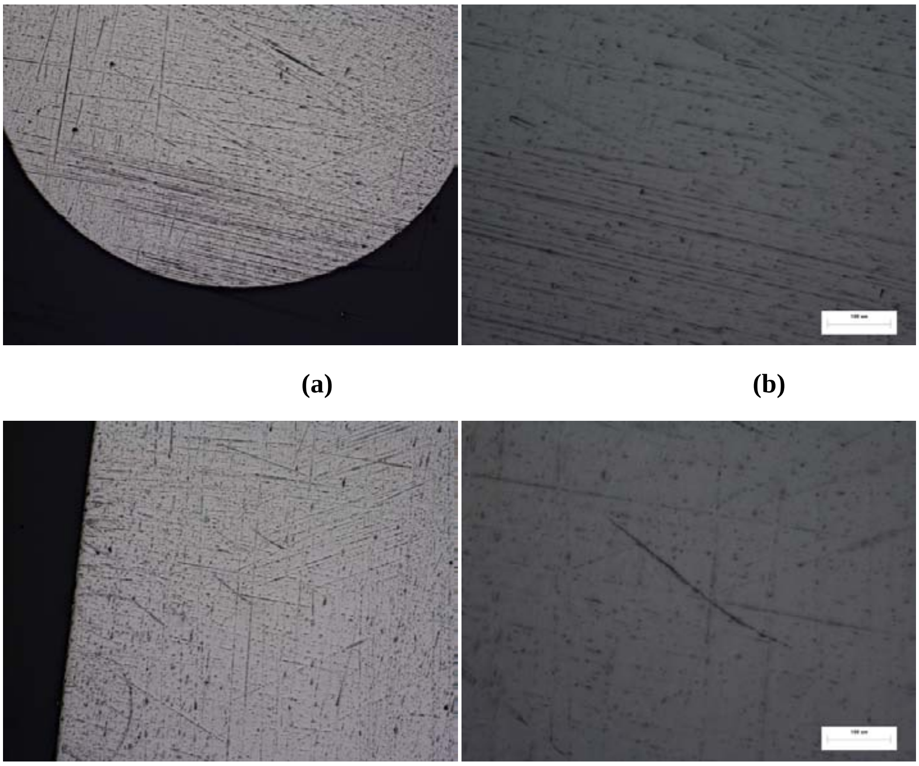

(a) (b)

(c) (d)

Figure 5.54: The microstructure of the compression samples of titanium, 1000oC, 1/s: (a) point B, ×50, (b) point B, ×200, (c) point A, ×50, (d) point A, ×200

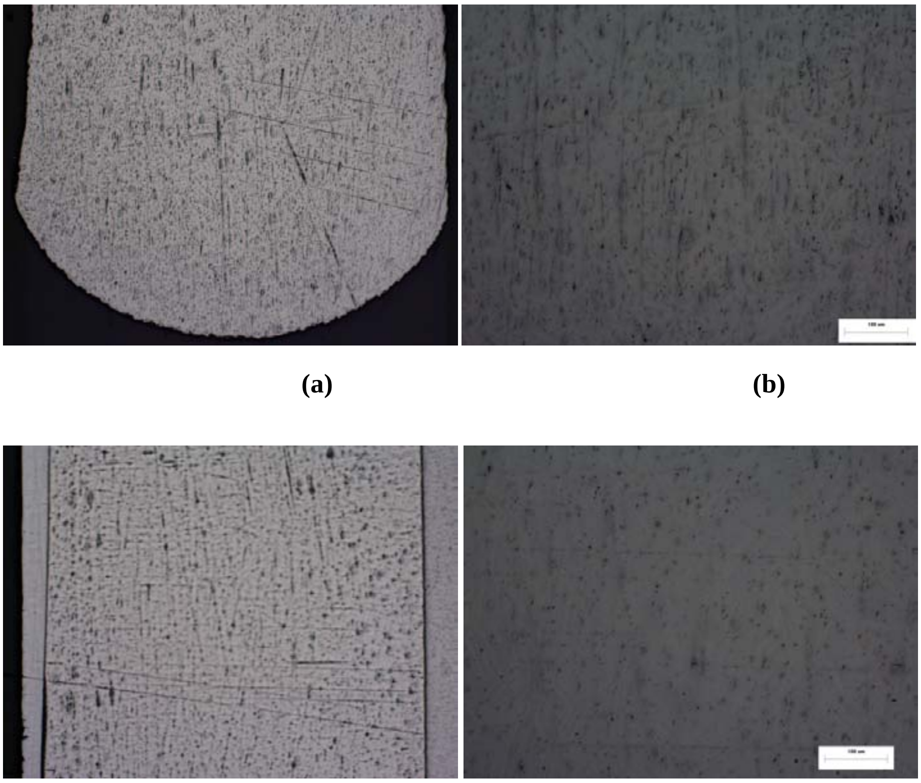

(a) (b)

(c) (d)

Figure 5.55: The microstructure of the compression samples of titanium, 1200 ^{o}C, 0.01/s: (a) point B, ×50, (b) point B, ×200, (c) point A, ×50, (d) point A, ×200

From these figures, the following observations were made:

- In mose cases, there were few pores in the areas around point A, so it was confirmed that these areas were close to fully dense. However, in Figure 5.52 (c), there still were many pores at the edge because of friction at lower temperature and higher strain rate during upsetting.
- Increasing initial temperature and reducing strain rate were very beneficial to powder consolidation by.
- Compared titanium (HDH) with Ti-6Al-4V (GA), the pores of the Ti-6Al-4V (GA) were much more than that of titanium (HDH).

In summary, the density distribution of the samples was generally consistent with the results of simulation.

Chapter 6: Conclusions and Recommendations for Future Work

6.1 Conclusions

The upsetting of powder compacts of pure titanium (HDH) and Ti-6Al-4V has been studied in this thesis by using experiments and numerical simulation. The deformation, heat transfer, friction and densification of upsetting of powder compacts were investigated deeply. The following conclusions are drawn from the research:

(1) The theory of plasticity of metal powder material was reviewed. Based on the constituent equations of stress, strain, temperature, strain rate and density in ABAQUS programme, the basic simulation model was set up.

(2) To obtain the true stress-true stress curves of the powder compacts as input data for simulation, a Gleeble 1500 thermal simulation testing machine was used to test the high temperature mechanical properties of powder compacts of pure titanium (HDH) and Ti-6Al-4V.

(3) After the material properties were established and the boundary conditions of geometric model was set up, the upsetting simulations of powder compacts of pure titanium (HDH) and Ti-6Al-4V were run successfully in ABAQUS. From the post-processing of ABAQUS, the distributions of temperature field, Mises stress field, strain rate field and relative density field were attained.

(4) The simulation shows that as the amount of deformation increases the stress, strain and relative density increase, but the temperature decreases.

(5) The simulation shows that the strain rate affects the deformation significantly. If the temperature is constant, Mises stress decreased with strain rate. However, practically, the temperature of sample decreases with time gradually when the stress of the sample increases if strain rate is

constant. Thus, the effect of strain rate on deformation must be combined with cooling rate of sample.

(6) The simulation shows that increasing the initial temperature of the powder compacts is beneficial to densification and making stress distribution more uniform.

(7) The simulation shows that increasing friction coefficient between the sample and the die is disadvantagous to densification and reduction of stress. In practice, suitable lubricant should be used at the interface between the sample and the die to reduce the friction coefficient.

(8) From the curves of displacement with loading, the deformation force increases with decraesing strain rate, as a result of that the rate of the sample softening is higher than that of hardening. The deformation force decreases with increasing the initial powder compact temperature. In addition, there was no obvious effect on deformation force by friction.

(9) By using an optical microscope, it was observed that the density distribution of the sample is in accordance with the results of simulation. However, since the underlying relationships of powder consolidation used in the simulation model have not been well established, actual relative density near the edge of the sample is commonly higher than that predicted by the simulation.

6.2 Recommendations for Future Work

The high temperature deformation process of metal powder material is an intricate process which includes many microstructural changes such as static recovery, dynamic recovery, recrystallization and phase transformation. Thus, in order to study high temperature deformation behavior of metal powder material accurately, the constituent equations of the model of the material need to be studied further. In addition, theoretical study must be combined with experimental study. Based on the basic coupled thermo-mechanical 3D-FEA model in this thesis, in the future, other hot forming processes. Such as complex forging, extrusion and rolling should be simulated.

References

[1] M. J. Donachie, *Titanium: a technical guide*: Asm Intl, 2000.

[2] M. Arciniegas, *et al.*, "Low elastic modulus metals for joint prosthesis: Tantalum and nickel-titanium foams," *Journal of the European Ceramic Society,* vol. 27, pp. 3391-3398, 2007.

[3] R. Atwood, *et al.*, "Modeling the investment casting of a titanium crown," *Dental Materials,* vol. 23, pp. 60-70, 2007.

[4] F. Jones, "Teeth and bones: applications of surface science to dental materials and related biomaterials," *Surface Science Reports,* vol. 42, pp. 75-205, 2001.

[5] N. Poondla, *et al.*, "A study of the microstructure and hardness of two titanium alloys: Commercially pure and Ti-6Al-4V," *Journal of Alloys and Compounds,* vol. 486, pp. 162-167, 2009.

[6] G. Lütjering and J. C. Williams, *Titanium*: Springer Verlag, 2007.

[7] Specifications for the Lockheed SR-71 [Online]. Available: http://www.fiddlersgreen.net/models/aircraft/Lockheed-SR71.html

[8] SR-71 BLACKBIRD TITANIUM [Online]. Available: Http://www.mach3ti.com

[9] A. Choudhury and M. Blum, "Economical production of titanium-aluminide automotive valves using cold wall induction melting and centrifugal casting in a permanent mold," *Vacuum,* vol. 47, pp. 829-831, 1996.

[10] Wikipedia [Online]. Available: http://en.wikipedia.org/wiki/Titanium#cite_note-HistoryAndUse-4

[11] Pistons and Titanium Rods for NC30 &NC35 from G-Force [Online]. Available: http://akhara.com/nc30/pistonrod1/index.html

[12] PRO X STEEL VALVE CONVERSION KITS [Online]. Available: http://www.powersportsnetwork.com/accessoriesdetail/product=944448/levelcode=10304/catalog=6338/Western+Power+Sports+Offroad/PRO+X+STEEL+VALVE+CONVERSION+KITS/accessories944448.htm

[13] K. Toyama and T. Kuwayama, "Trial Production and Strength Assessment of Titanium Alloy Connecting Rods," *Sumitomo Met.,* vol. 41, pp. 75-80, 1989.

[14] S. R. Seagle, "The state of the USA titanium industry in 1995," *Materials Science and Engineering: A,* vol. 213, pp. 1-7, 1996.

[15] Benefits of Medical Titanium [Online]. Available: http://www.supraalloys.com/prodapp.php

[16] Watches Channel [Online]. Available: http://watches.infoniac.com./

[17] Wikimedia Commons [Online]. Available: http://commons.wikimedia.org/wiki/Main_Page

[18] Optingolfer [Online]. Available: http://www.optingolfer.com/blog/

[19] The Bicycle Info Project [Online]. Available: http://www.equusbicycle.com/bike/index.html

[20] PointGlasses.com [Online]. Available: http://www.pointglasses.com/fashion-glasses/

[21] A. Lawley and T. F. Murphy, "Metallography of powder metallurgy materials," *Materials*

characterization, vol. 51, pp. 315-327, 2003.

[22] I. Pokorska, "Modeling of powder metallurgy processes," *Advanced Powder Technology*, vol. 18, pp. 503-539, 2007.

[23] R. Baccino and F. Moret, "Numerical modeling of powder metallurgy processes," *Materials & Design*, vol. 21, pp. 359-364, 2000.

[24] Shengyuan MIM&PM [Online]. Available: http://www.sino-metalparts.com/technology/powder-metallurgy

[25] Sino-metalparts.com [Online]. Available: http://www.sino-metalparts.com/technology

[26] T. H. Okabe, *et al.*, "Titanium powder production by preform reduction process (PRP)," *Journal of Alloys and Compounds*, vol. 364, pp. 156-163, 2004.

[27] W. Kroll, "METHOD FOR MANUFACTURING TITANIUM," ed: Google Patents, 1940.

[28] W. Kroll, "The production of ductile titanium," *Journal of The Electrochemical Society*, vol. 78, p. 35, 1940.

[29] *ASM : Metal Handbook: Powder Metal Technologies and Applications*
Volume 7.

[30] Wikipedia.HIP [Online]. Available: http://en.wikipedia.org/wiki/Hot_Isostatic_Pressing

[31] J. Duva and P. Crow, "The densification of powders by power-law creep during hot isostatic pressing," *Acta Metallurgica Et Materialia*, vol. 40, pp. 31-35, 1992.

[32] P. Yu, *et al.*, "Two-stage sintering of nano-sized yttria stabilized zirconia process by powder injection moulding," *Journal of Materials Processing Technology*, vol. 192, pp. 312-318, 2007.

[33] Wikipedia.SLS [Online]. Available: http://en.wikipedia.org/wiki/Selective_laser_sintering

[34] F. Anon, "Hayes Develops Automated Powder Forging Line.," *Metal Powder Report*, p. 310, 1986.

[35] P. K. Johnson., "New P/M Applications," *INTERnational Journal of Powder Metallurgy*, vol. 26, p. 383~367, 1990.

[36] www.mpif.org [Online]. Available: http://www.mpif.org/DesignCenter/designcenter.asp?linkid=11

[37] 51Manufacture web site [Online]. Available: http://www.51zz.org/chengxing/xianjin/shimeshifenmoduanzaojiqigongyiguocheng_89.html

[38] C. C. Huang and J. H. Cheng, "An investigation into the forming limits of sintered porous materials under different operational conditions," *Journal of Materials Processing Technology*, vol. 148, pp. 382-393, 2004.

[39] N. J. Howard A.Kuhn and B.Lynn Ferguson.Powder Forging.Metal Powder Industries Federation Princeton.

[40] H. Kuhn and C. Downey, "Deformation characteristics and plasticity theory of sintered powder materials," *Int J Powder Met*, vol. 7, pp. 15-25, 1971.

[41] A. Freudenthal, "The inelastic behavior of solids," ed: Wiley, New York, 1950.

[42] M. Cockcroft and D. Latham, "Ductility and the workability of metals," *J Inst Metals*, vol. 96, pp. 33-39, 1968.

[43] P. Brozzo, *et al.*, "A new method for the prediction of formability limits in metal sheets," 1972.

[44] Wikipedia.Extrusion [Online]. Available: http://en.wikipedia.org/wiki/Extrusion

[45] R. Lapovok, *et al.*, "Low-temperature compaction of Ti-6Al-4V powder using equal channel angular extrusion with back pressure," *Materials Science and Engineering: A*, vol. 490, pp. 171-180, 2008.

[46] Wikipedia.Simulation [Online]. Available: http://en.wikipedia.org/wiki/Simulation

[47] D. F. Zhang, "Numerical and physical simulation of new SPD method combining extrusion and equal channel angular pressing for AZ31 magnesium alloy," *Transactions of Nonferrous Metals Society of China*, vol. 20, pp. 478-483.

[48] H. R. Darani and M. Ketabchi, "Simulation of," *Materials & Design*, vol. 25, pp. 535-540, 2004.

[49] W. Lin, *et al.*, "Boundary-element method simulation of the impact of bounding walls on the dynamics of a particle group freely moving in a wide-gap Couette flow," *Applied Energy*, vol. 83, pp. 669-680, 2006.

[50] G. Fang, *et al.*, "FEM simulation of aluminium extrusion through two-hole multi-step pocket dies," *Journal of Materials Processing Technology*, vol. 209, pp. 1891-1900, 2009.

[51] Wikipedia.Finite Element Method [Online]. Available: http://en.wikipedia.org/wiki/Finite_element_method

[52] P. Montmitonnet, "Hot and cold strip rolling processes," *Computer Methods in Applied Mechanics and Engineering*, vol. 195, pp. 6604-6625, 2006.

[53] A. F. Gerday, *et al.*, "Interests and limitations of nanoindentation for bulk multiphase material identification: Application to the [beta] phase of Ti-5553," *Acta Materialia*, vol. 57, pp. 5186-5195, 2009.

[54] J. Huang, *et al.*, "A general rigid-plastic/rigid-viscoplastic FEM for metal-forming processes based on the potential reduction interior point method," *International Journal of Machine Tools and Manufacture*, vol. 43, pp. 379-389, 2003.

[55] D. Systemes, "Getting Started with Abaqus " *Dessault Systémes, Providence, RI*, 2007.

[56] D. Systemes, "ABAQUS/CAE User's Manual," *Dessault Systémes, Providence, RI*, 2007.

[57] Wikipedia.Abaqus [Online]. Available: http://en.wikipedia.org/wiki/ABAQUS

[58] D. Systemes, "ABAQUS Theory Manual," *Dessault Systémes, Providence, RI*, 2007.

[59] D. Systemes, "ABAQUS Example Problems Manual," *Dessault Systémes, Providence, RI*, 2007.